RESPONSE OF A PENDULUM SPAR TO 2-DIMENSIONAL

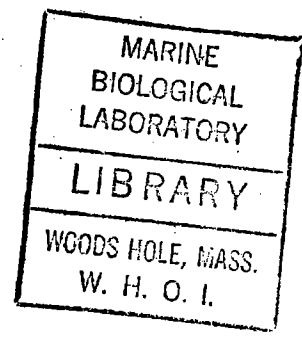RANDOM WAVES AND A UNIFORM CURRENT

by

GEORGE RODENBUSCH

B.S., RICE UNIVERSITY

1974

M.M.E., RICE UNIVERSITY

1974

SUBMITTED IN PARTIAL FULFILLMENT OF THE
REQUIREMENTS FOR THE DEGREE OF
DOCTOR OF PHILOSOPHY

at the

MASSACHUSETTS INSTITUTE OF TECHNOLOGY

and the

WOODS HOLE OCEANOGRAPHIC INSTITUTION

August, 1978

Signature of Author ....
Joint Program in Ocean Engineering, Massachu-
setts Institute of Technology/Woods Hole Ocean-
ographic Institution, and Department of Ocean
Engineering, Massachusetts Institute of Tech-
nology, August, 1978

Certified by ....
Thesis Supervisor

Accepted by ....
Chairman, Joint Committee on Ocean Engineering,
Massachusetts Institute of Technology/Woods
Hole Oceanographic Institution

RESPONSE OF A PENDULUM SPAR TO 2-DIMENSIONAL

RANDOM WAVES AND A UNIFORM CURRENT

by

GEORGE RODENBUSCH

Submitted to the Department of Ocean Engineering

in August 1978 in partial fulfillment of the requirements

for the Degree of Doctor of Philosophy.

ABSTRACT

A linearized theory for the response of a circular pen-
dulum spar in 2-dimensional waves and a uniform current is devel-
oped. The linear forces on the cylinder are predicted using an
approximate potential flow theory for slender bodies. The dynamic
equations are then amended to account for the wake effects of
viscous bluff body flow by including a quadratic drag law and
neglecting wave damping. A spectral model for the forces on a
cylinder due to an oscillating wake, modeling the force as a
frequency modulation process, is proposed. The non-linear
equations of motion which result are then solved, assuming con-
stant force coefficients, by linearization for use with a Gaussian
random sea. The method of equivalent linearization is extended to
include mean flow effects and a spatially distributed process.
Some numerical experiments are then used to test the performance

of the linearization. For a variety of environments, the linearization predicts the standard deviation of the simulation response to within 10% and the mean angle of inclination to within 30%. Results of the numerical experiments indicate that there is significant variation (order of magnitude changes) in both response and mean angle of inclination. Thus, significant changes are followed by the linearization.

A laboratory experiment was carried out to test the linearized spar model in a realistic fluid environment. Only the low Keulegan Carpenter number regime was investigated. With some minimal manipulations, good agreement is obtained between the experiment and the linearized estimates. It appears that the drag coefficients for vortex induced in-line forces may be an order of magnitude larger than those reported in the literature, .5 instead of .06, and that the shedding of vortices due to steady flow may reduce the added mass coefficient significantly, as observed in oscillating flows with significant vortex shedding.

ACKNOWLEDGEMENTS

TABLE OF CONTENTS

LIST OF FIGURES

LIST OF TABLES

LIST OF SYMBOLS

A_o	fluid excursion amplitude
A	wave amplitude
$a(t)$	time varying amplitude of $f(t)$
a	amplitude of cylinder motion
C	$= \frac{2}{\pi}\, C_D\, /\, (\frac{\rho_c}{\rho} + C_a)$
C_a	added mass coefficient
C_D	drag coefficient
$\hat{C}_D$	vortex force drag coefficient
$\hat{C}_L$	vortex force lift coefficient
$\hat{C}_{L(max)}$	vortex force lift coefficient based on maximum normal fluid speed and maximum lift force
C_T	damping coefficient in governing equation
D	cylinder diameter
$E[\ ]$	expected value
F	$= \frac{1}{2}\pi K k^2\, F^*\, \cosh kz$
F^*	$= \int_o^h \zeta\, R^2(\zeta)\, \cosh k\zeta\, d\zeta$
F'	$= (1 + C_a)\, /\, (\frac{\rho_c}{\rho} + C_a)$
F_D	drag force
$\hat{F}_D$	vortex drag force
$\hat{F}_L$	vortex lift force
f	oscillation frequency $= \omega\, /\, 2\pi$

$f(t)$	$= a(t) \sin[\omega_c(t) t]$
f_c	frequency of forced cylinder oscillation
$\tilde{f}_\ell$	expected lift force frequency
f_v	vortex shedding frequency of a fixed cylinder
g	acceleration of gravity
$H_{(\ )}$	transfer function of ( )
h	fluid depth
I	moment of inertia
i	$= \sqrt{-1}$
K	$= \dfrac{(k_\infty + k) e^{-kh} \sinh kh}{k_\infty h + \sinh^2 kh}$
K_S	stability parameter
k	wave number $= \dfrac{2}{\lambda}$
k_∞	infinite depth wave number $= \omega^2 / g$
L	length of cylinder
ℓ_v	excursion length of a fluid particle corresponding to a shed vortex
M	mass
$M_{\hat{D}}$	vortex drag moment
M_L	vortex lift moment
$M^*_{\psi D}$	viscous drag moment
$M^*_{\zeta D}$	viscous drag moment
M^*_{ψ}	inviscid damping moment
m_e	equivalent mass per unit length

m_x	mass per unit length plus hydrodynamic
N_{KC}	Keulegan-Carpenter number
N_R	Reynolds number
N_S	Strouhal number
PDF	probability density function
p	pressure
p^*	inviscid damping pressure
R	radius of spar
r_c	spanwise correlation of vortex lift force
(r, Θ, z)	circular cylindrical coordinate system
(r', Θ', z')	body fixed circular cylindrical coordinate system
S_L	vortex lift force spectrum
S_{M_L}	vortex lift moment spectrum
$S_{M_{\hat{D}}}$	vortex drag moment spectrum
S_{P-M}	Pierson-Moskowitz fully developed spectrum
t	time
t_o	defined by $\omega_c(t_o) = \omega$
U_E	equivalent velocity
U_M	magnitude of velocity vector
U_o	mean current
U_{oE}	equivalent velocity for computing mean inclination

u	velocity of fluid normal to the cylinder which would exist in the absence of the cylinder
u_r	relative velocity
V	spectral wind speed in the Pierson-Moskowitz fully developed spectrum
(x, y, z)	cartesian coordinate system, z positive upwards, origin at the center of rotation
(x', y', z')	body fixed coordinate system
z_{cg}	coordinate of the center of mass
α	dummy variable
β	$= N_R / N_{KC}$
δ	angle of inclination in the y-z plane
δ'	logarithmic decrement
γ	dummy integration variable for z
$\varkappa$	stiffness of the spar restoring force
λ	wave length
ν	kinematic viscosity
ζ	modal displacement of vibrating cylinder
ρ	fluid density
ρ_c	average density of spar
σ_{ψ_L}	standard deviation of linearized prediction
σ_{ψ_S}	standard deviation of the simulation
$\sigma_{(\ )}$	standard deviation of ( )
Φ	velocity potential
ϕ	phase

ϕ_Λ diffraction potential

ϕ_I incident potential

ϕ_ψ displacement potential

ϕ_ψ^* damping potential

ψ angle of pitch of spar

ψ_0 mean angle of inclination

ω radian frequency

ω' dummy frequency

$\omega_c(t)$ time varying carrier frequency

ω_v $2\pi f_v$

ω_D Doppler shifted wave frequency
$= \omega - k U_o$

$\bar{\omega}_\ell$ $= 2\pi \bar{f}_\ell$

$\dot{(\ )}$ differentiation with respect to time

1. Introduction

The problem which originally motivated this work involved the analysis of the dynamics of a tilting spar current sensor, Mavor, et.al. (1976). In this case it was necessary to evaluate the effect of surface waves on the mean inclination of the spar to determine its performance as a current sensor. The spar has a natural frequency in the region of wave excitation and therefore cannot be treated as stationary, allowing one to make direct use of the large body of literature for wave forces on cylinders. Bluff body drag, which is the dominant dissipative force on the spar and a possible exciting force, is fundamentally non-linear, so that an elementary application of linear vibration theory is not possible. With the advent of offshore oil development in deep water, 300 m or more, structures with cylindrical components are being built with natural frequencies in the region of surface wave excitation. Motions of the structure and resonance behavior must therefore be considered in evaluating environmental loading. The question of dynamics of cylinder structures in a wave current environment is then of some general interest.

The forces on cylinder structures in various fluid environments has been a topic of considerable interest in classical and modern fluid dynamics. The cylinder provides a mathematically tractable geometry and is a popular engineering structure because of its symmetry, large stiffness and ease of

manufacture. With the advent of extensive offshore oil production considerable energy has been expended to determine the forces on cylinders in waves and currents. In fact, most effort has been directed at either the wave problem, oscillating flow, or the steady flow problem, with minimal thought given to the interaction. The most complete set of 2-dimensional experimental data on cylinders in sinusoidally oscillating flows is presented by Sarpkaya (1976). Some interesting experiments on vertical cylinders in sinusoidal waves have been performed by Bidde (1971), Isaacson (1974) and various other authors. The results concerning in-line forces of such experiments are generally interpreted in terms of Morison's equation. This formulation decomposes the force into a component proportional to the instantaneous normal acceleration, inertial force, and one proportional to the instantaneous square of the normal velocity, viscous force, which would exist in the undisturbed flow. The decomposition of the force in this manner is at first intuitively satisfactory, but there is such large scale flow disturbance due to the viscous wake that the good experimental performance of Morison's equation seems somewhat fortuitous. This point is clearer if we note that for small fluid excursion amplitude-to-cylinder diameter ratios, where inertial forces dominate, and for large amplitude-to-diameter ratios, where viscous forces dominate, Morison's equation performs well, whereas in the intermediate range of fluid amplitudes, the

equation experiences its poorest performance, see Sarpkaya (1976).
The transverse forces due to periodic asymmetries in the wake are
not well behaved and the results are generally presented in a
purely empirical form.

Offshore structures have in the past been in relatively
shallow water so that they could be considered rigid and stationary.
Dynamic phenomena are not usually considered, and most wave force
experimentation and theory make use of fixed rigid cylinders.
The results of wave force experimentation are generally applied
by choosing a "design wave" and compatible force coefficients
to compute maximum forces on a structure. Borgman (1967) presents
an elegant random process description of wave forces on fixed
cylinders, ignoring transverse forces and mean currents, and
obtains good agreement with a single field experiment. Such an
approach is essential in the consideration of a system's dynamics
since using a deterministic force instead of the essentially
random force imposed by ocean waves may lead to significant errors
in the determination of response. The linearization which is
presented here employs a random process model, and the result is
equivalent to Borgman's first order estimate when it is simplified
to the case which he considered.

Investigators such as Griffin (1975), Gerrard (1966),
and Tanida, et.al. (1973) have been interested in the vortex
shedding behind cylinders. Of special interest to these investi-

gators are the transverse vibrations of elastically supported

cylinders, as well as the effects of small forced sinusoidal

oscillations on the wake. A majority of these investigations

are motivated by a need to understand wake induced motions of

cables. Recently, as discussed by King (1977), in-line vortex

induced vibrations have become of some interest. All of the

experimental work in this field has led to an empirical repre-

sentation of an elastic system's response to steady flows,

generally represented as an amplitude at the natural frequency.

Some limited success has been obtained by applying the inviscid

von Karmen vortex street model to estimating forces on fixed

cylinders, Griffin (1972). A van der Pol oscillator model of

elastic cylinder wake interaction near resonance, Griffin (1975),

has received a great deal of attention, but it is complex and quite

limited in applicability.

Only one work, Seymour (1973), could be found which

analyzed the dynamics of a simple hydrodynamic system with large

viscous drag forces and included experimental verification.

Seymour investigated the dynamics of a tethered sphere in waves

and was especially interested in the dissipation of wave energy.

He modeled the sphere as a point oscillator, linearized the drag

term, and was able to achieve reasonably good agreement with

field experiments. It was decided therefore to perform a linear-

ization of the spar problem. The important concepts behind

statistical linearization can be found in a paper by Caughey
(1963). The analysis presented here includes the effects of
mean flow, vortex shedding and vertical spatial gradients not
previously discussed in the literature.

An experiment by Mercier (1973) is the only study
found which actually addresses the question of wave-current
interactions with respect to forces on cylinders. He oscillated
a cylinder sinusoidally in a flume and measured the force on the
cylinder in different speed flows. The results which he presents,
as well as those from other wave force measurements, indicate
a considerable change in force coefficients for different wave-
current environments. A constant coefficient model, as presented
here, may therefore be severely limited. However, the success
of the few experiments presented here and those of Seymour and
Borgman indicate that with a judicious choice of these coeffi-
cients, good results can be obtained.

The analysis presented here is directed at the question
of spar dynamics in co-linear uniform current and random 2-
dimensional waves. Although this is a somewhat artificial problem,
it embodies most of the complexities of realistic structure and
environment, while minimizing notational complexity. This is not
to imply that a single cylinder and co-linear waves and current
are typical, but that the treatment of spatial gradients, random
waves and simultaneous current represents a significant advance

in the analysis of engineering structures composed of cylinders.

The development begins with an estimation of the first order linear inviscid forces on the spar. The governing equations which result are then amended to include the effects of the separated wake and a linearization is then used to estimate the spar response. The performance of the linearization is then investigated by comparing it with the results from a numerical simulation. The entire spar response model is compared with some laboratory experiments. The experimental work is limited in scope and a more extensive set of experiments is necessary for a thorough evaluation of the model. The technique presented here can be generalized for more complicated structures and realistic environments, and the results presented here appear to make such an effort worthwhile.

2. Linearized Potential Solution

In this section, we will determine the first order inviscid forces due to 2 -dimensional waves incident on a pendulum spar, see Figure 2.1. The effects of viscosity will be considered in Section 3. The scheme used here involves the assumption of a slender body, that is a body with one dimension much larger than the other two, exhibiting small pitch motions in incident waves of small slope with a wavelength long compared to the body diameter. These assumptions will yield the equations of motion for an undamped linear oscillator. Since we are interested in the system response near resonance, a regime in which the first order conservative forces are in balance, we shall also consider the lowest order damping term, which is of second order. The motivation for considering this inviscid damping term is to allow us to compare it with the viscous damping estimated in Section 3. The solution for zero mean current is derived in Section 2.1, and the effects of a mean current are addressed in Section 2.2.

2.1 Zero Mean Current

The analysis presented here follows closely the work of Newman (1963) with some modifications. Newman considered the response of a free-floating spar buoy in heave, surge, and pitch to 2 -dimensional waves in a fluid of infinite depth. We shall restrict our attention to the pitch motions of the pendulum spar,
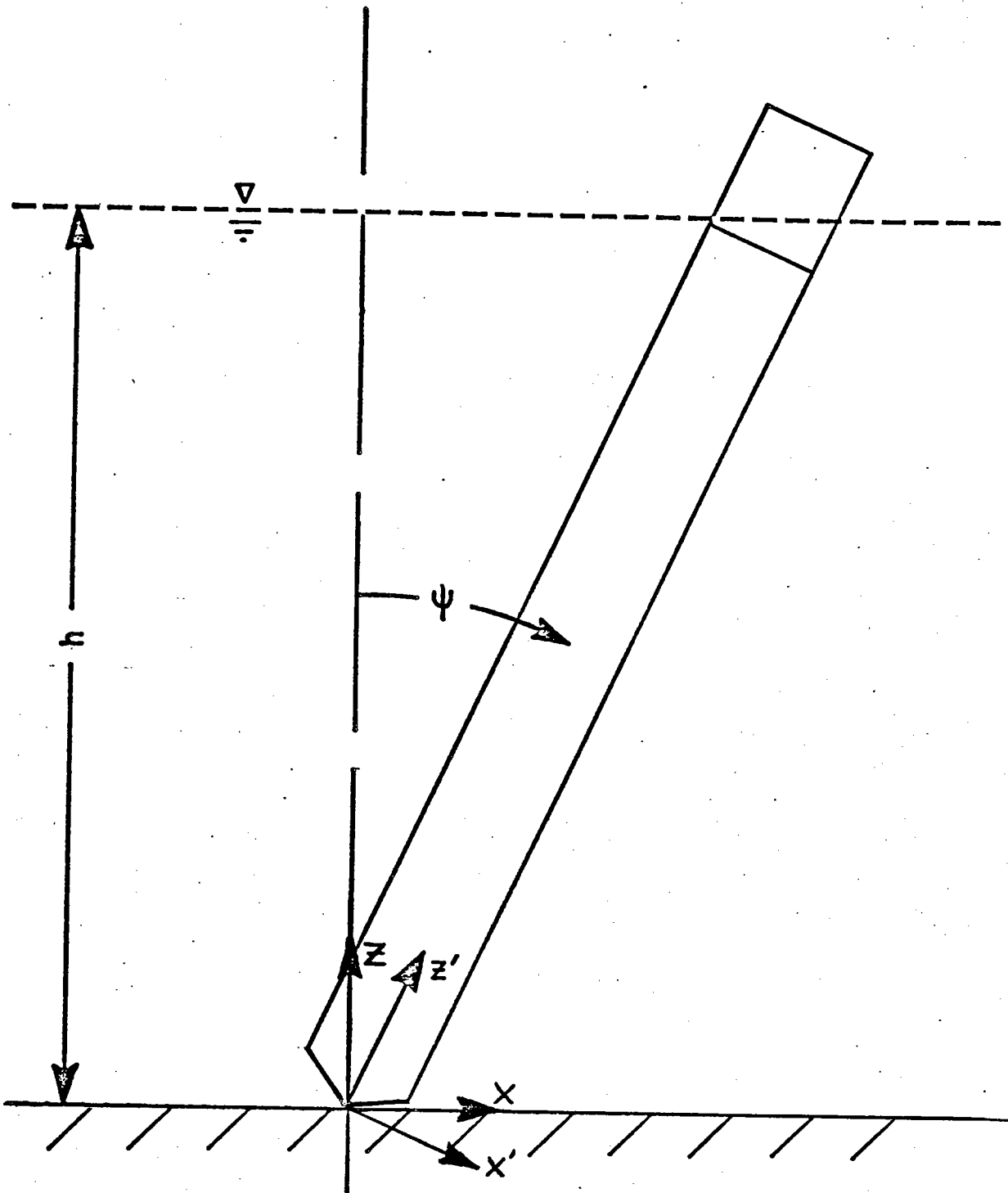
Figure 2.1 Coordinate System

and include the effects of a finite depth. There is a non-trivial error of a factor of 2 in the calculation of damping in Newman's paper, so calculation of the proper source potential for use in the damping calculations is included in Appendix A.

2.1.1 Problem Definition

A fixed Cartesian coordinate system (x, y, z) with z positive upwards is situated so that the origin coincides with the center of rotation of the body. The undisturbed free surface is at z = h and the x axis is the direction of incident wave propagation; see Figure 2.1. Use is made of a body fixed coordinate system (x', y', z'), with z' along the axis of the spar. When the spar is at rest (x, y, z) = (x', y', z'). We also use a circular cylindrical system (r, θ, z) with $x = r \cos \theta$ and $y = r \sin \theta$. The surface of the spar is defined by r' = R(z').

Letting ψ be the instantaneous angle of the body axis with respect to the z axis, we find that

$$x = x' \cos \psi + z' \sin \psi \qquad (2.1)$$

$$y = y'$$

$$z = z' \cos \psi - x' \sin \psi$$

Since the displacement ψ and the wave slope Ak, where A is the amplitude and k is the wave number, are assumed to be small, we shall linearize all equations by neglecting terms which are second order in these terms. Equation (2.1) is replaced by

$$x = x' + z'\psi \tag{2.2}$$

$$y = y'$$

$$z = z' - x'\psi$$

Assuming an inviscid, incompressible fluid, a velocity potential, Φ (x, y, z, t) whose gradient is the velocity vector, exists and must satisfy the following boundary conditions:

(1) a kinematic boundary condition at all boundaries
    (fluid does not pass through the boundary),

(2) a dynamic boundary condition on the free surface
    (pressure is constant), and

(3) a radiation condition at infinity (energy must
    propagate away from the body) for $_A$ and   below.

The linearized free surface, bottom and radiation boundary conditions are satisfied by the potentials of pulsating singularities, see for example Wehausen and Laitone (1960). The linearized body boundary condition is satisfied by a distribution of these singularities along the mean axis.

In order to simplify the analysis, we shall decompose the velocity potential as follows

$$\Phi(x, y, z, t) = \phi_I + \phi_A + \phi_\psi \tag{2.3}$$

The potential of the incident waves is

$$\phi_I = A \frac{g}{\omega} \frac{\cosh kz}{\cosh kh} e^{i(kx - \omega t)} \tag{2.4}$$

where ω is the radian frequency, g is the acceleration of gravity, and $i = \sqrt{-1}$. Note that this implicitly assumes that the wave slope is small. The dispersion relation for finite depth is

$$\omega^2 = gk \tanh kh \qquad (2.5)$$

The potential ϕ_A is the diffraction potential of the fixed body.

The potential ϕ_ψ is due to the motion of the body and is linear

in ψ. From Appendix A, Equations A.9 and A.11, we find that, to

lowest order in r, the above potentials are

$$\phi_\psi = \tfrac{1}{2}\,\dot{\psi}\left[2z\,\frac{R^2_{(z)}}{r}\cos\theta - \right. \qquad (2.6)$$
$$i\pi K k^2 x \cosh kz_0\, F^* - $$
$$\left. i2\,\frac{\cos\theta}{r}\,R^2_{(z)}\,F_{(z)}\right]$$

where

$$K = \frac{(k_\infty + k)\,e^{-kh}}{k_\infty h + \sinh^2 kh}\,\sinh kh$$
$$k_\infty = \omega^2/g$$
$$F^* = \int_0^h \varsigma\, R^2_{(\varsigma)}\cosh k\varsigma\, d\varsigma$$
$$F_{(z)} = \tfrac{1}{2}\pi K k^2 F^* \cosh kz$$

and

$$\phi_A = i\,\frac{Agk}{\omega}\,\frac{\cosh kz}{\cosh kh}\,\frac{R^2_{(z)}}{r}\,\cos\theta\, e^{-i\omega t} \qquad (2.7)$$

2.1.2 Equations of Motion

The equations of motion of the spar are obtained by

integrating the pressure over the surface of the body to obtain

the ψ moment. This moment is balanced by the angular acceleration

of the body and the gravitational moment. The linearized Bernoulli

equation is used to find the pressure

$$p = \rho\,\frac{\partial \bar{\phi}}{\partial t} - \rho g\,(z-h) \qquad (2.8)$$

To lowest order on the body

$$p = -\rho g(z - \psi R \cos\theta - h) - \rho \frac{\partial \phi_\psi}{\partial t} - \rho\left[\frac{\partial \phi_\theta}{\partial t} - i A g \frac{\cosh kz}{\cosh kh} e^{-i\omega t}(1 + ik)\right] \tag{2.9}$$

$$p = -\rho g(z - \psi R \cos\theta - h) - \rho \ddot{\psi} R z \cos\theta - 2\rho g A k R \cos\theta \frac{\cosh kz}{\cosh kh} e^{-i\omega t} + \rho g A \frac{\cosh kz}{\cosh kh} e^{-i\omega t} \tag{2.10}$$

The equation of motion is

$$I\ddot{\psi} - M z_{cg}\psi = -\int_0^h \int_0^{2\pi} z p R \cos\theta \, d\theta \, dz \tag{2.11}$$

where I is the moment of inertia, M is the mass, and Z_{cg} is the distance to the center of gravity. Substituting Equation (2.10) for the pressure and integrating over θ, Equation (2.11) becomes

$$I\ddot{\psi} - M z_{cg}\psi = -\psi \rho g \pi \int_0^h z R^2(z) \, dz - \rho \pi \ddot{\psi} \int_0^h z^2 R^2(z) \, dz + 2\rho g A k \frac{1}{\cosh kh} \int_0^h z R^2(z) \cosh kz \, dz \, e^{-i\omega t} \tag{2.12}$$

The terms on the right-hand side of Equation (2.12) are readily recognized. The first term is the hydrostatic restoring moment and the second term is the added moment of inertia. The last term represents the exciting moment due to the horizontal pressure gradient under the incident wave and the diffraction pressure field necessary to accelerate the fluid around the spar.

Equation (2.12) is the governing equation of an undamped oscillator, and as such would predict large motions near resonance. Since, near resonance, the first order conservative forces due to mass and stiffness cancel, it is reasonable to look for the lowest order damping forces. For a body in an inviscid fluid with a free surface, the energy dissipated in damping takes

the form of radiated waves.

The damping forces can be estimated by considering terms in the pressure field which are in phase with the body velocities. The force in phase with $\dot{\psi}$ is derived from the imaginary part of the potential ϕ_ψ, Equation (2.6). Thus, the damping potential can be written as

$$\phi_\psi^* = -i\pi K k^2 \cosh kz \, F^* \left(r + \frac{R(z)}{r}\right)\dot{\psi}\cos\theta \qquad (2.13)$$

The damping pressure is

$$p^* = -\rho\left(\frac{\partial\phi_\psi^*}{\partial t}\right) \qquad (2.14)$$

$$= i\rho\pi K k^2 \cosh kz \, R \, F^* \ddot{\psi}\cos\theta$$

Therefore, the damping moment is

$$M_\psi^* = -\int_0^h\int_0^{2\pi} p^* z \, R\cos\theta \, d\theta \, dz \qquad (2.15)$$

$$= -i\rho\pi^2 K k^2 F^* \ddot{\psi}\int_0^h z\cosh kz \, R^2_{(z)} \, dz$$

$$= -i\,\ddot{\psi}\rho\pi^2 K k^2 F^*$$

We can now add this moment to Equation (2.12), and upon rearranging, obtain the damped equation of motion,

$$\psi\Big[-\omega^2\Big(I + \rho\pi\int_0^h z^2 R^2_{(z)}dz\Big) - \omega^2 i\rho\pi^2 K k^2 F^{*2} + \qquad (2.16)$$

$$\rho g\pi\int_0^h z \, R^2_{(z)}\,dz - M z_{cg}\Big]$$

$$= 2Ak\frac{\pi\rho g}{\cosh kh}F^* e^{-i\omega t}$$

For the case of a right circular cylinder, $R(\zeta) = R$, considered here, Equation (2.16) can be written as

$$\psi\Big[-\omega^2\Big(I + \rho\pi R^2\frac{h^3}{3}\Big) - i\omega^2\rho\pi^2 R^4\frac{K}{k^2}(kh\sinh kh - \qquad (2.17)$$

$$\cos kh + 1)^2 + \rho g\pi R^2 h - M z_{cg}\Big]$$

$$= 2\rho g A\frac{\pi R^2}{k\cosh kh}(kh\sinh kh -$$

$$\cos kh + 1)\,e^{-i\omega t}$$

2.2 Effect of a Uniform Current

Including a uniform current in the inviscid solution

has three principal effects. There is a Doppler shift due to

wave advection by the current, so that the spar encounters wave

crests at a frequency other than ω. The character and magnitude

of wave damping can change drastically. A mean force in the

direction of the flow will exist due to surface wave generation.

This is identical to the wave drag experienced by ships. However,

the first order oscillating inertial and restoring forces are not

affected by the presence of a current.

Havelock (1958) has demonstrated analytically that the

effect of a uniform current on the damping potential for low fre-

quencies corresponding to wave lengths much larger than the body

diameter, i.e., $kR \ll 1$, is to increase the damping. He also shows

that there is a critical speed, $U_o = \dfrac{g}{4\omega}$, at which infinite

damping may be predicted. It seems, therefore, that a computa-

tion of the wave damping is necessary. However, the assumption

of inviscid flow about a bluff body when there is a mean current

is grossly inadequate and the solutions are not likely to have

much quantitative significance. The effort required to find

these solutions does not seem justified. In the next section we

will, in fact, demonstrate that for most cases of interest, large

motions, the linear wave damping term for zero mean flow is

negligible in comparison with the viscous forces. We shall

therefore assume that viscous damping will always dominate.

We shall now investigate the frequency change due to the mean current. Assuming the current is in the x direction, we write the incident wave potential in a coordinate system moving with the mean current,

$$\phi_I = \frac{Ag}{\omega} \frac{\cosh kz}{\cosh kh} e^{i(kx''-\omega t)} \qquad (2.18)$$

where $x'' = x - U_o t$ and U_o is the magnitude of the uniform current. Notice that in this coordinate system the wave is unchanged. Rewriting Equation (2.18) in the fixed coordinate system, we find

$$\phi_I = \frac{Ag}{\omega} \frac{\cosh kz}{\cosh kh} e^{i(kx-(kU_o+\omega)t)} + U_o X \qquad (2.19)$$

We can see immediately that the lowest order term, dipole, in the potentials ϕ_ψ and ϕ_A will not be changed if we let the contribution of $U_o x$ be balanced by a wave drag potential, which we are going to neglect as we stated above. The only change to the equation of motion will be due to the moment exerted by the incident potential. Some care must be used in computing the pressure, since we have introduced an arbitrary mean speed. We will need the dynamic pressure term in the unsteady Bernoulli equation so that

$$P_I = -\rho \left[\frac{\partial \phi_I}{\partial t} + \frac{1}{2} (\nabla \phi_I \cdot \nabla \phi_I) \right. \qquad (2.20)$$

$$= -\rho \left[i \frac{Ag}{\omega} \frac{\cosh kz}{\cosh kh} (-kU_o-\omega) e^{i(kx-(kU_o+\omega)t)} + \right.$$

$$\frac{1}{2}((U_o + ik \frac{Ag}{\omega} \frac{\cosh kz}{\cosh kh} e^{i(kx-(kU_o+\omega)t)})^2 +$$

$$\left. (\frac{Ag}{\omega} k \frac{\sinh kz}{\cosh kh} e^{i(kx-(kU_o+\omega)t)})^2 \right)$$

Simplifying and neglecting second order terms in Ak, we find that,

$$P_I = i\rho g A \frac{\cosh kz}{\cosh kh} e^{i(kx-(kU_o+\omega)t)} - \frac{1}{2} U_o^2 \qquad (2.21)$$

Since the dynamic pressure $\frac{1}{2}U_o^2$ contributes nothing to the

moment integral, it is clear that the only change in the equation

of motion, Equation (2.17), will be to substitute $e^{-i(kU_o + \omega)t}$

for $e^{-i\omega t}$ on the right-hand side.

3. Viscous Effects

It has been observed that a viscous fluid flowing at a moderate constant speed about a cylinder "separates" from the body and forms vortices, coherent over varying lengths of the cylinder, which shed and form a periodic wake. The result of this process is a force in line with the flow with a mean and a periodic component and a force normal to the flow with only a periodic component. Comparable effects have been noticed in slowly varying flows.

The forces on a cylinder in viscous flow have received much attention during the last 20 years. The results have been largely empirical due to the intractable governing equations for viscous flows. Experiments have been carried out primarily in steady flows, occasionally in oscillating flows, but rarely in a combination of the two. The data from these experiments have been organized through a set of dimensionless parameters, which aid in generalizing specific results. These parameters are generated through a knowledge of the relevant properties of the system being investigated, and use of the Pi Theorem which defines the number of dimensionless groups which may be formed. If all of the important properties are included, a physical law can be written as a function of the dimensionless groups. For a cylinder in viscous flow, these "laws" are complicated functions and are presented in the form of graphs, although there are parameter ranges in which simple analytical representations can

be found.

We shall review the real fluid effects for steady flow case in Section 3.1 and for the oscillatory flow case in Section 3.2. A model based on "strip" theory, which incorporates this empirical information with the inviscid solution of Section 2, is presented in Section 3.3.

3.1 Steady Flow

A recent review article by King (1977) gives an extensive summary of the state of knowledge on steady flow normal to circular cylinders. Some of the highlights of this article are presented here as background.

3.1.1 Fixed Cylinder

The important dimensionless parameters used in characterizing steady viscous flow about a fixed cylinder of diameter D are

$$N_R = \frac{U_o D}{\nu} \qquad = \text{Reynolds number}$$

where U_o is the mean speed, and ν is the kinematic viscosity,

$$N_S = \frac{f_v D}{U_o} \qquad = \text{Strouhal number}$$

where f_v is the frequency at which vortex pairs are shed, that is, the lift force frequency,

$$C_D = \frac{F_D / L}{\frac{1}{2} \rho U_o^2 D} \qquad = \text{drag coefficient}$$

where F_D is the mean drag force on a cylinder of length L.

$$\hat{C}_D = \frac{\hat{F}_D / L}{\frac{1}{2}\rho U_o^2 D} = \text{time varying drag coefficient}$$

where $\hat{F}_D$ is a function of the time varying part of the total drag

force, for example, the amplitude or the root mean square, and

$$\hat{C}_L = \frac{\hat{F}_L / L}{\frac{1}{2} U_o^2 D} = \text{time varying lift coefficient}$$

where $\hat{F}_L$ is the amplitude or maximum value of the lift force.

Note that there is no mean lift on a non-rotating circular

cylinder.

For a fixed cylinder in 2 -dimensional steady flow,

the general experimental relationship of the Strouhal number,

the drag coefficient and the Reynolds number is shown in Figure

3.1. The well-behaved subcritical region is usually characterized

by constant $C_D \simeq 1$ and $N_S \simeq .21$, and is the region in which most

experimental work on vortex shedding is done. For short cylinders

with a free end, the Strouhal number is reduced as much as 40%

due to end effects. The location of the transition from a laminar

to a turbulent boundary layer, the critical region, will vary with

surface roughness and flow turbulence, but behaves as shown in

Figure 3.1.

The time varying lift and drag coefficients show a

great deal of scatter. For $10^3 < N_R < 10^5$, $C_L \simeq .6$, and

$C_D \simeq .06$. The frequency of the drag force is twice that of the

lift force, and corresponds to the actual frequency of vortex

shedding. The measurements of these fluctuating coefficients

are complicated by the poorly understood longitudinal spatial

correlation of the shed vortices. For the subcritical region,
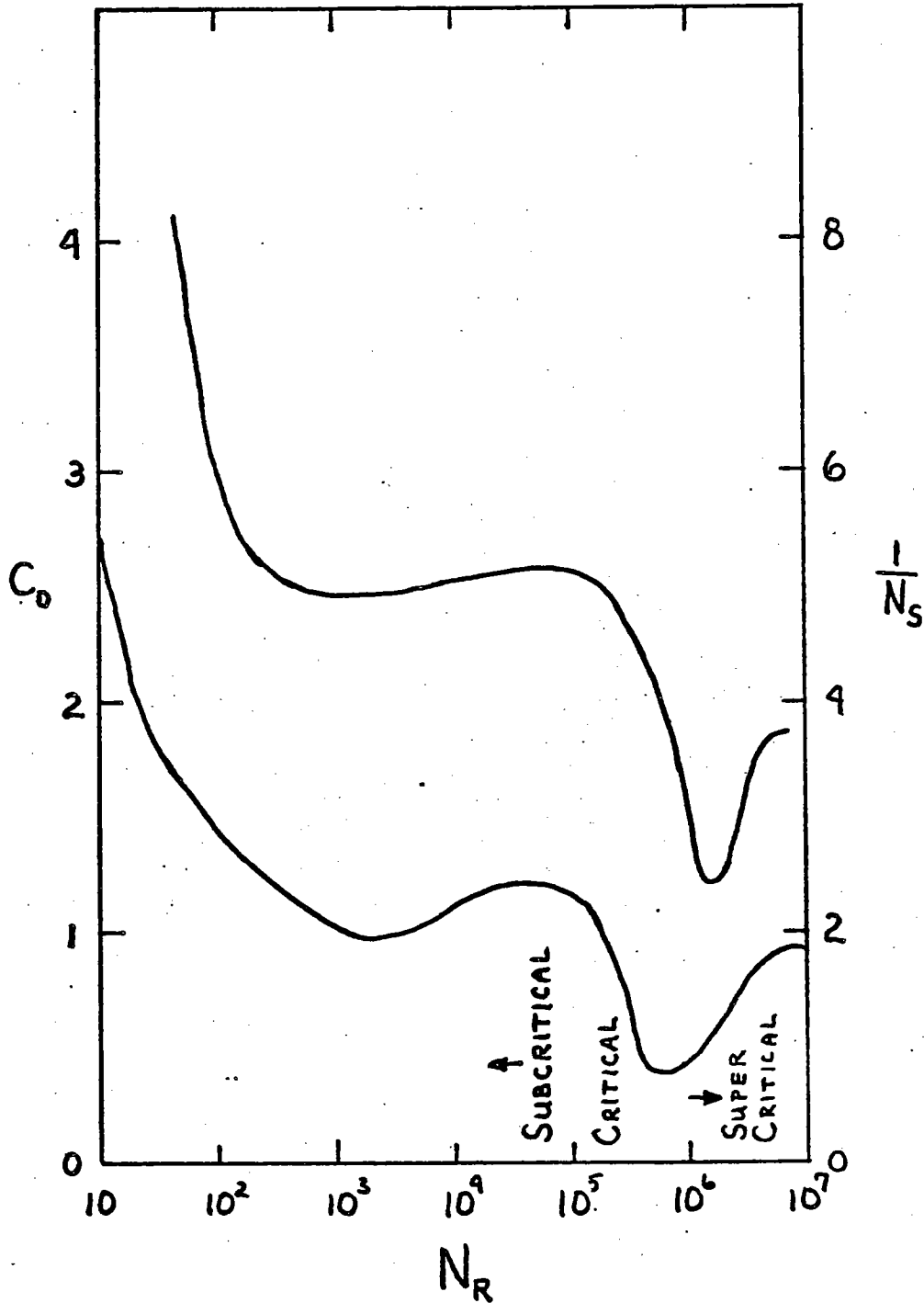
Figure 3.1 Relationship between drag coefficient
           Strouhal number and Reynolds number for
           fixed cylinders in steady flow (from King).

the correlation length is the order of two or three cylinder diameters and for $N_R > 10^5$, the correlation length is the order of half a diameter. The amplitude of the lift force on a long circular cylinder varies as the vortex "cells" move into and out of phase, as we would expect with a narrow band random process. Since most test cylinders are longer than the correlation length, this would explain some of the scatter in the data for the time varying lift and drag coefficients.

3.1.2 Forced Cylinder Oscillation

When a cylinder is oscillated in otherwise uniform flow, there are two significant changes in the flow. The first is known as "lock-in" or "wake capture". This is a region of forced oscillation near the fixed cylinder vortex frequency, or its first two harmonics, where the vortices are shed in phase with the forced cylinder motion. The second effect is an increase in the correlation length and strength of the shed vortices. To help deal with the additional complexity, two more parameters are introduced; the dimensionless displacement, $\frac{a}{D}$, where a is the amplitude, and the frequency ratio, $\frac{f_c}{f_v}$, where f_c is the forced frequency of oscillation.

3.1.2.1 Transverse Oscillations

When oscillations are transverse to the flow, lock-in occurs around $\frac{f_c}{f_v} = 1$, that is, a vortex is shed from each side of

the cylinder during one cycle. The lock-in range increases with $\frac{a}{D}$ up to roughly $.7 < \frac{f_c}{f_v} < 1.3$ for $\frac{a}{D} \gtrsim .1$. It has been observed, Tanida, et.al. (1974), that the lift force is in phase with the cylinder velocity for $\frac{f_c}{f_v} > 1$, with a maximum magnitude around $\frac{f_c}{f_v} = 1.2$, and out of phase for $\frac{f_c}{f_v} < 1$. The lift force, therefore, tends to maintain the oscillation for frequencies greater than the fixed cylinder shedding frequency, f_v . The lift forces reach a maximum around $\frac{a}{D} = .5$. This has been attributed to an increasing correlation length, as well as a slight increase in the circulation of each vortex, as $\frac{a}{D}$ increases from zero. For large amplitudes, $\frac{a}{D} > .5$, a breakdown in the vortex shedding occurs, as more than one vortex is shed during each half cycle, and forces decrease.

3.1.2.2 In-Line Oscillations

Lock-in for forced in-line motions exhibits two overlapping regimes. The first occurs around $\frac{f_c}{f_v} = 2$, and corresponds to one vortex shed during each cycle, that is, near the fixed cylinder drag oscillation frequency. The lift and drag coefficients in this regime are approximately the same as those of a fixed cylinder. The second in-line lock-in regime occurs in the neighborhood of $\frac{f_c}{f_v} = 4$ and is characterized by simultaneous shedding of a pair of vortices with each cycle of oscillation. In this regime there is virtually no lift force and the oscillating drag coefficient has not been measured directly. Griffin (1976)

has observed both of these regimes occurring intermittently near $\frac{f_c}{f_v}$ = 2. There is little force data on either of these in-line regimes since the forces seem to be an order of magnitude less than the transverse forces and result in correspondingly small free vibrations.

3.1.3 Elastic Vibrations

Free vibrations have been observed in each of the three forced regimes, i.e., one transverse and two in-line. In general, they are excited when the system natural frequency lies in a lock-in region and the system damping is low enough to allow motions which cause lock-in and increased spanwise correlation. The two dimensionless parameters which characterize the system dynamics are the reduced velocity, $\frac{U_o}{f_n D}$, where f_n is the natural frequency, and the stability parameter, $K_S = \frac{2 m_e \delta'}{D^2}$, where δ' is the logarithmic decrement and m_e is the equivalent mass/unit length.

$$m_e = \int_0^L m_x \xi^2 \, dz \Big/ \int_0^h \xi^2 \, dz$$

where ξ is the "modal" displacement, equal to z for the spar, and m_x is the actual mass per unit length plus the hydrodynamic added mass, $\rho \pi R^2$, for the immersed length. The response of an elastically supported circular cylinder to a uniform current is summarized by Figures 3.2 and 3.3, taken from King (1977). Figure 3.2 shows the three lock-in regimes and the response for K_S = 0. The variation of the response peaks with K_S is shown
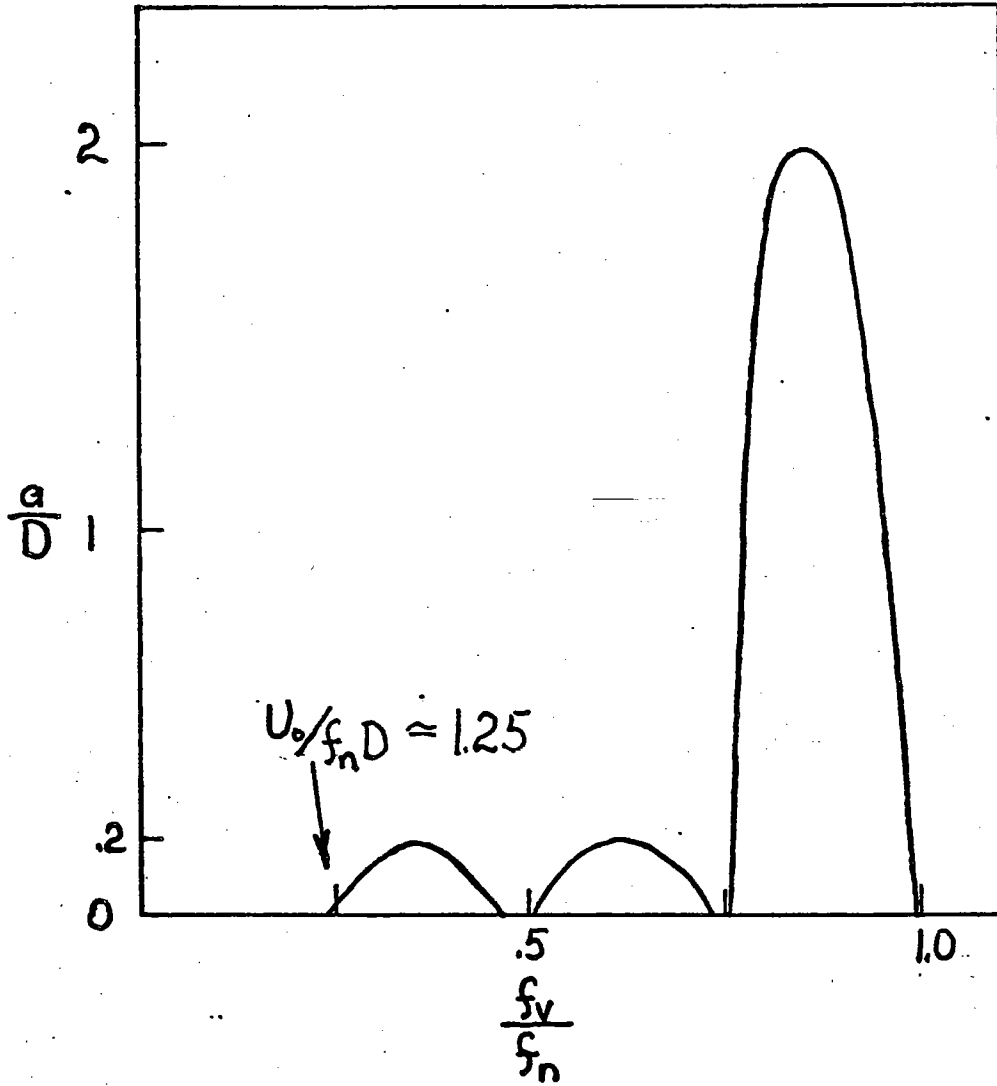
Figure 3.2 Composite graph of instability regions
in-line and cross-flow (from King).
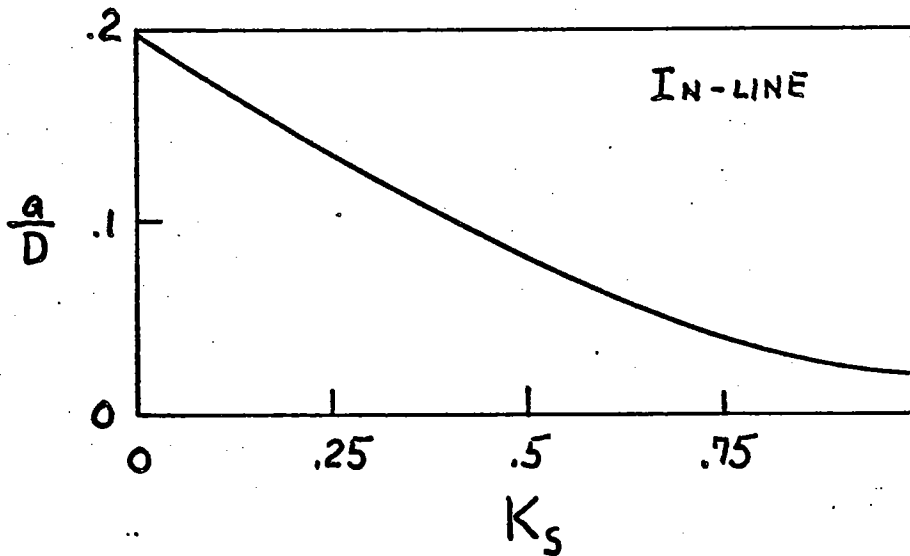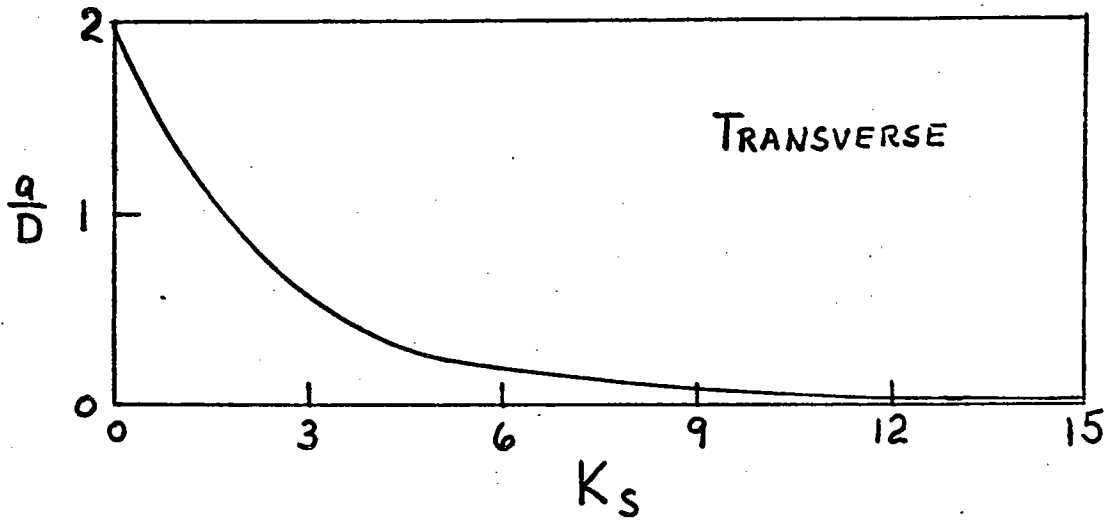
Figure 3.3 Limiting amplitudes of self-excited
oscillations

in Figure 3.3. Efforts have been made by Skop and Griffin (1973) and others to describe the cylinder-wake interactions using a Van der Pol oscillator equation for the lift coefficient. The results of this work lend little physical insight to the problem and are of use only in estimating system response near transverse resonance.

3.2 Oscillatory Flow

The forces on cylinders in oscillating flows have been investigated in waves and in uniform flows, almost exclusively with sinusoidal excitation. Results for in-line forces are generally analyzed in terms of Morison's Equation:

$$F/L = C_D \tfrac{1}{2}\rho D u |u| + (1+C_a)\rho \pi R^2 \dot{u} \qquad (3.1)$$

where u is the speed of the fluid in the absence of the cylinder. There is a drag term similar to steady flow and a hydrodynamic mass term representing the forces predicted by potential theory. The lift forces are defined in terms of the amplitude of the fluid velocity

$$\hat{C}_{L(max)} = \frac{F_{L(max)}/L}{\tfrac{1}{2}\rho U_{(max)}^2 D}$$

and an average shedding frequency. In addition, two other dimensionless numbers are important: the Keulegan Carpenter number, $N_{KC} = \frac{U_{(max)}}{fD}$, which includes the fluid oscillation frequency, f, and the Reynolds number, usually based on $U_{(max)}$.

The graphs presented in Figures 3.4 to 3.7, from Sarpkaya (1976), represent forces on a fixed cylinder in 2-

dimensional oscillating flow in a "U" shaped water tunnel. The drag and mass coefficients, given in Figures 3.4 and 3.5, are the first two coefficients of a normalized quasi Fourier series decomposition of the total in-line force, that is

$$C_D = - \frac{\frac{3}{4\pi} \int_0^{2\pi} F(t) \cos\theta' d\theta'}{\frac{1}{2}\rho D U_{(max)}^2 L}$$

$$C_M = \frac{1}{\pi} \int_0^{2\pi} F(t) \sin\theta' d\theta' \Big/ \rho \omega U_{(max)} L \pi R^2$$

where $u = -U_{(max)} \cos \omega t$, and $\theta' = \omega t$. Notice that the coefficient for C_D is normalized by $\int_0^{2\pi} \cos^2\theta |\cos\theta| d\theta = \frac{4\pi}{3}$

Figure 3.6 shows the maximum lift coefficient observed during a run and Figure 3.7 is a plot of the relative vortex shedding frequency, $f_r = \frac{f_v}{f}$.

These figures become easier to interpret if we rewrite N_{KC} using the fact that $U_{(max)} = 2\pi f A$ where A is the excursion amplitude of the fluid, that is

$$N_{KC} = \frac{2\pi A}{D}$$

The parameter $\beta = \frac{N_R}{N_{KC}}$ is introduced by Sarpkaya because it is independent of amplitude.

$$\beta = \frac{f D^2}{\nu}$$

The Keulegan Carpenter number is, therefore, an amplitude axis and the constant β lines are constant frequency lines. It is also useful to note that the Keulegan Carpenter number is proportional to the ratio of the maximum drag force to the maximum inertial force, so that if we assume $C_D = 1$ and $C_M = 2$, $N_{KC} \simeq 20$ represents equal drag and inertia forces.

If we invert the added mass coefficient, we see that
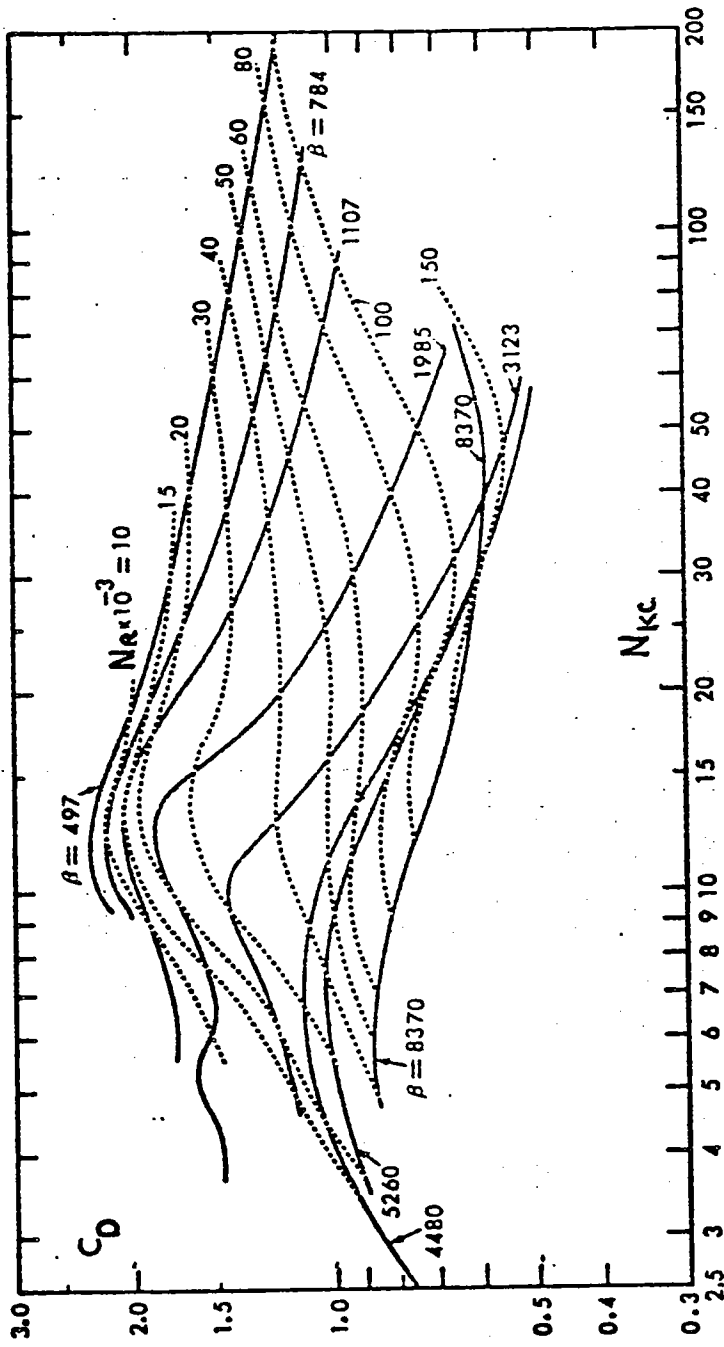
Figure 3.4 C_D versus N_{KC} for particular values of N_R, Sarpkaya (1976)
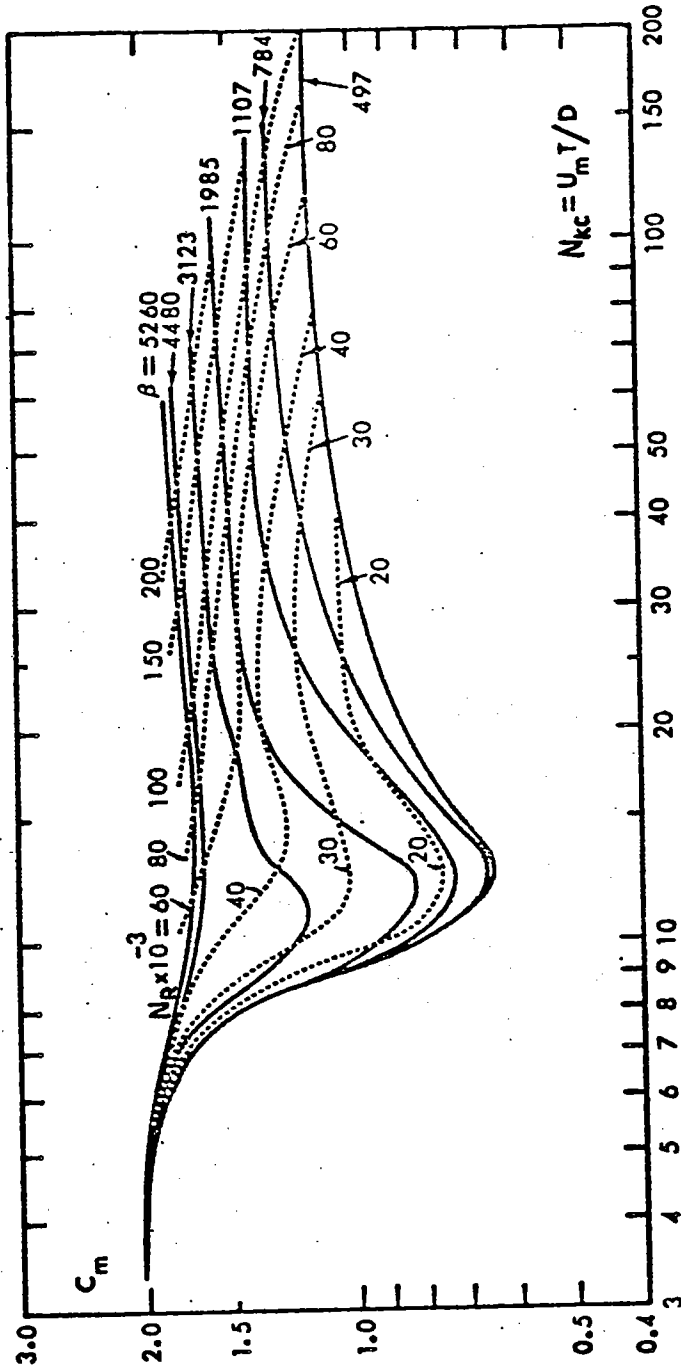
Figure 3.5 C_m versus N_{KC} for particular values of N_R, Sarpkaya (1976)
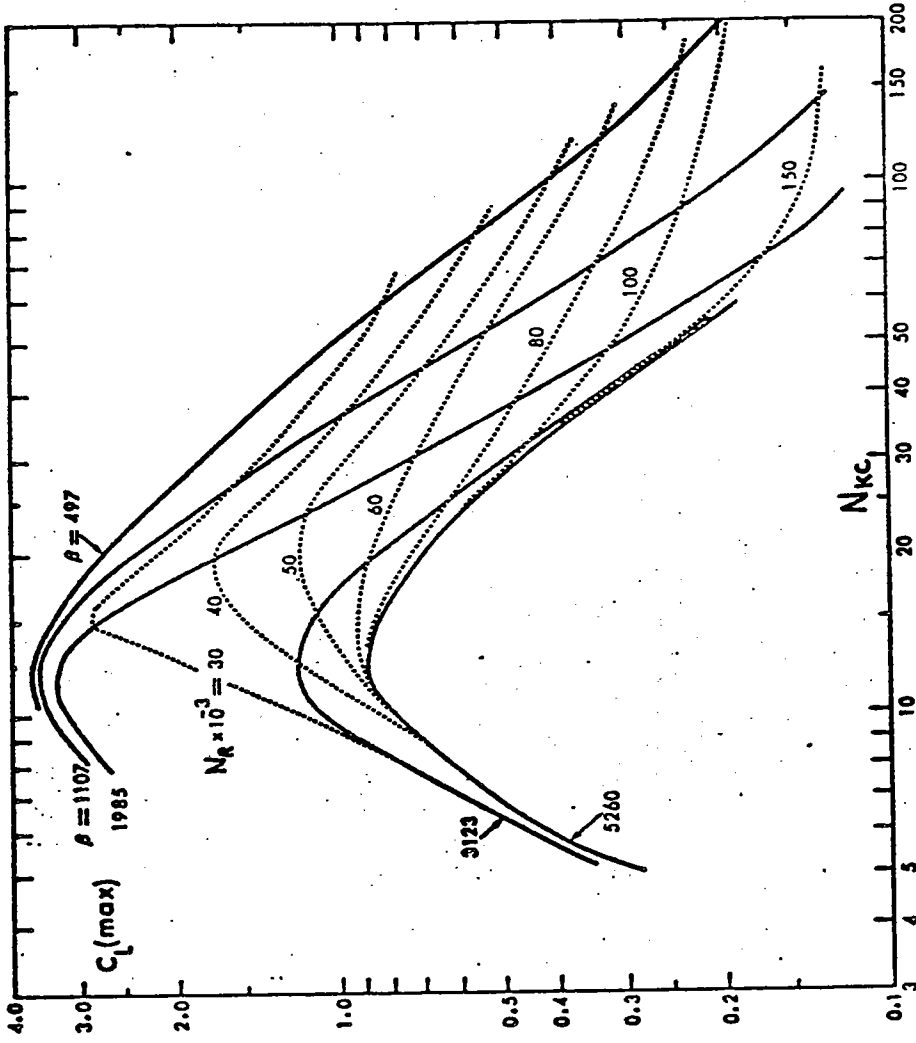
Figure 3.6 $C_{L(max)}$ versus N_{KC} for various values of N_R, Sarpkaya (1976)
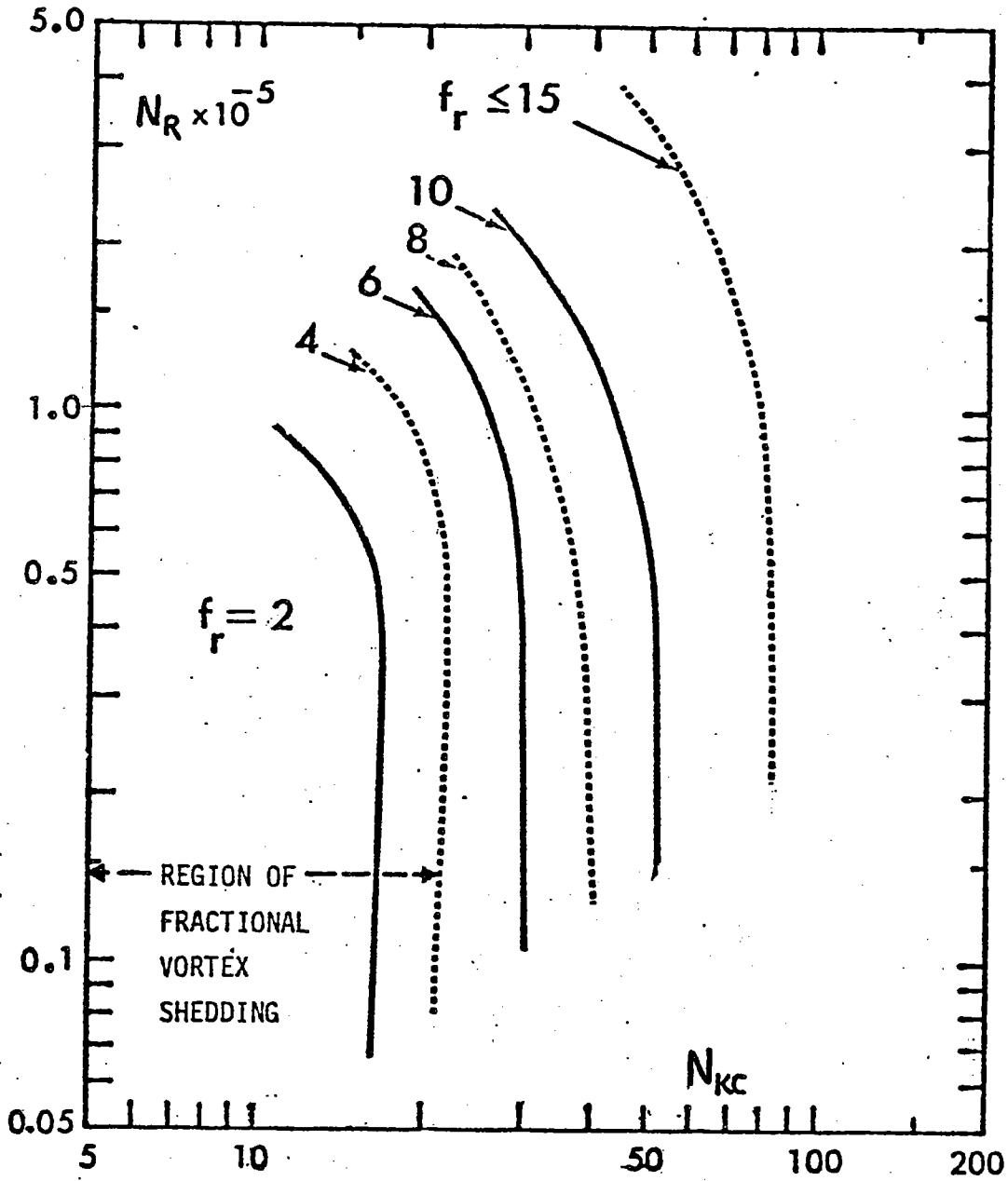
Figure 3.7 Relative frequency of vortex shedding
as a function of the Reynolds and
Keulegan-Carpenter numbers, Sarpkaya (1976)

Figures 3.4 to 3.6 have basically the same shape, with a maxima

around N_{KC} = 15. The magnitudes of C_M and C_D are fairly well be-

haved, but the lift coefficient varies by an order of magnitude,

and is larger than observed in steady flows. These large lift

coefficients seem to be the result of constructive interference

between the wake of the previous half cycle and vortices currently

being generated. Sarpkaya notes that in this region Morison's

equation appears to have its poorest performance, due to large

in-line forces at approximately twice the eddy shedding frequency.

However, such large lift coefficients may not be characteristic

of the natural environment. Experiments by Mercier (1973) indi-

cate that with a small mean velocity introduced into the flow,

the lift coefficient is reduced. This supports the notion that

the large vortex forces may indeed be due to the high coherence

of purely sinusoidal flow. In a random velocity field with some

mean component, a more "natural" environment, the lift coefficient

might be expected to behave more like a constant. In any case,

the model proposed here assumes constant drag, mass and lift co-

efficients. The exact values chosen could be taken from

Sarpkaya's data by characterizing the environment in terms of

the expected frequency and expected amplitude.

3.3 Equations of Motion

Viscous effects may be incorporated into the equations

of motion by employing strip theory. That is, a 2- dimensional

flow normal to the cylinder is assumed, which is not affected by gradients along the cylinder axis or flow along the axis. This assumption is compatible with the slender body potential theory of Section 2 and is partially supported by steady flow drag measurements on cylinders inclined to the flow, see Hoerner (1965), where the drag force is proportional to $(U_o \cos \psi)^2$. In waves this implies that we will be considering only the horizontal component of water velocity, assuming small angles of inclination for the spar.

Thus using the strip theory, we decompose the viscous effects into a "steady" force, i.e., a force which is proportional to the square of the normal velocity, and a "vortex" force. The "vortex" force is modeled as a random process independent of the other forces on the cylinder.

3.3.1 "Steady" Drag

Incorporation of the "steady" drag force into Equation 2.20 is straightforward. In anticipation of forces and motions normal to the wave current direction, we introduce an angular displacement δ in the $x = 0$ plane of Figure 2.1. For small motions, ψ and δ are orthogonal, and there is no coordinate coupling. Therefore, the viscous drag moments are

$$M_{\psi_D}^* = \int_0^h C_D \frac{1}{2} \rho \, U_m^2 \, \frac{(u - z\dot{\psi})}{U_m} \, D z \, dz$$

and

$$M_{\delta_D}^* = -\int_0^h C_D \frac{1}{2} \rho \, U_m^2 \, \frac{z\dot{\delta}}{U_m} \, D z \, dz$$

where u is the fluid velocity in the incident field and the

resultant velocity

$$U_m = [(u - z\dot\psi)^2 + (z\dot\delta)^2]^{1/2}$$

The wave making drag moment is much smaller than this

viscous moment for long cylinders. To illustrate this, the ratio

of the wave drag to viscous drag in still water for $\psi = \psi_M \sin\omega t$

is plotted in Figure 3.8 for the experimental spar described in

Section 5. Note that the ratio is proportional to $\frac{1}{\psi_M}$. In the

neighborhood of the natural frequency the wave damping forces

are small, and we will therefore drop this term from the equations

of motion, as well as ignore any contribution to the mean angle of

inclination from the free surface wake. We postpone writing the

equations of motion until after considering the "vortex" forces.

3.3.2 Vortex Forces

The transverse vortex force is modeled as a frequency

modulation of the dynamic pressure, that is,

$$F_L = \tfrac{1}{2}\rho \hat C_L u^2 DL \sin\left[2\pi \frac{uN_s}{D} t\right] \tag{3.3}$$

where the frequency, $\frac{uN_s}{D}$, comes directly from the definition of the

Strouhal number. Agreement of this form with experiment when u

is a constant is obvious. We shall demonstrate that in a purely

sinusoidal flow, this formulation for the lift force implies

that the frequency content of the lift force is dominated by

the frequency corresponding to the maximum velocity. This

observation lends considerable help in interpreting Sarpkaya's
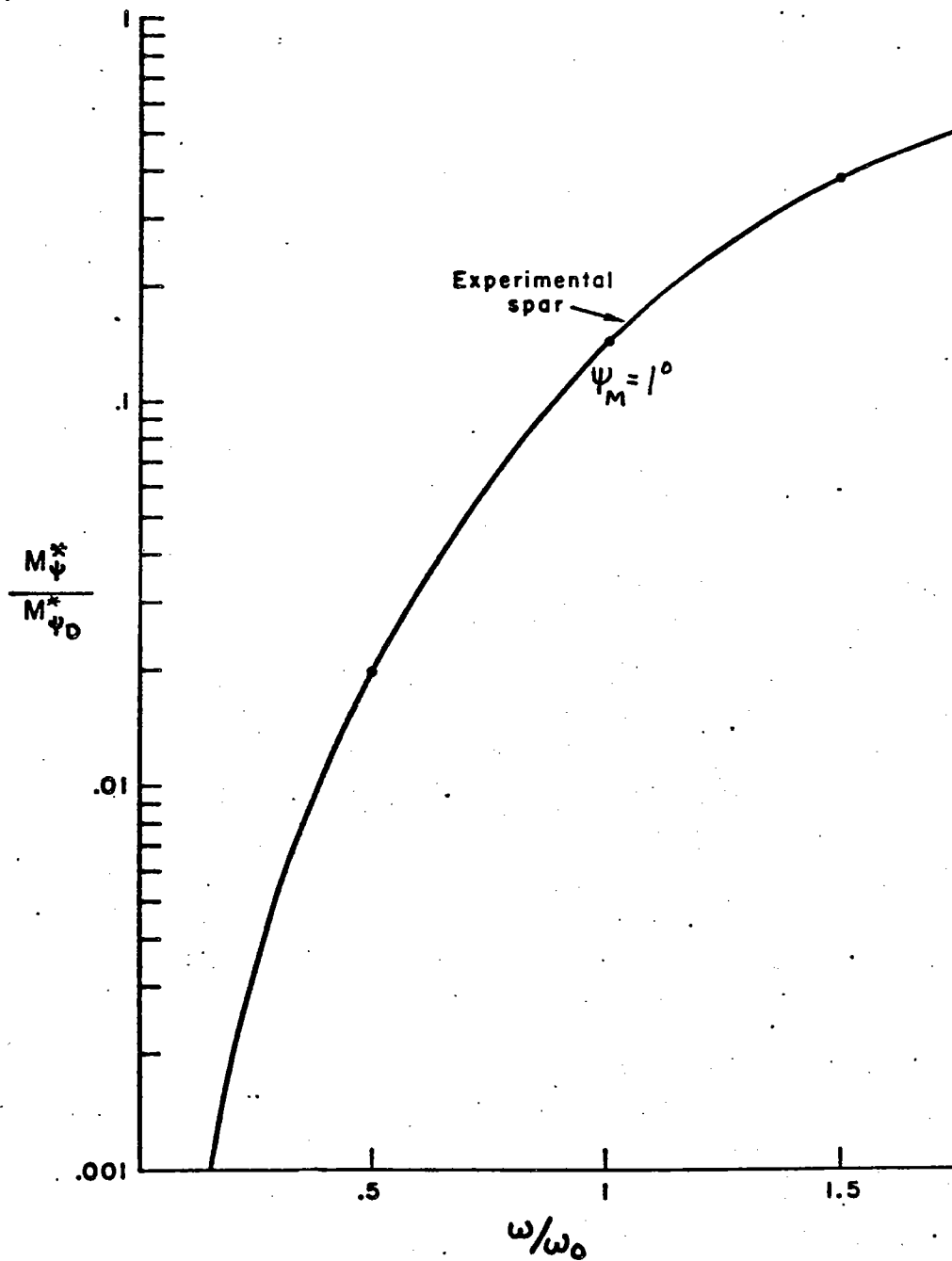
Figure 3.8 Ratio of Wave Damping Moment to Bluff
Body Drag Moment versus Frequency Ratio
for Model Experimental Spar, computed
for a pitch amplitude of 1°.

data, shown in Figure 3.7, which corresponds to an approximately
constant Strouhal number. We will look first at the sinusoidal
case, and then at the random wave case of special interest here.

3.3.2.1 Sinusoidal Flow

A constant Strouhal number, for steady flow, implies
that a pair of vortices is shed every time a fluid particle in
the free stream travels a certain number of diameters. We can
compute this length as

$$\ell_v = \frac{U_o}{f} = \frac{D}{N_s}$$

In fact, one might imagine vortices as made up of a constant
length of boundary layer. In sinusoidal flow, or any flow for
that matter, we can imagine a vortex being shed each time the
fluid travels the distance, $\ell_v/2$. The vortices are in effect
integrating the flow up to some cutoff point where a vortex is
shed. This idea is supported by experimental results of Bruun
and Davies (1975), where the vortex frequency was found to be
almost constant with r.m.s. turbulence levels up to 10% of the
mean. For harmonic flow with a particle excursion amplitude,
A_o, the relative vortex frequency, f_r, can be written as

$$f_r = \frac{2A_o}{\ell_v} = 2\frac{(N_{KC}D/2\pi)}{D/N_s} \qquad (3.4)$$
$$= \frac{N_{KC}N_s}{\pi}$$

where $2A_o$ is the distance a fluid particle travels during half a
cycle and ℓ_v is the distance a particle travels for each shed
vortex. If we assume Sarpkaya's data reflects the vortex shed-

ding frequency, Equation (3.4) predicts a Strouhal number of approximately .5 in the low Reynolds number regime. This Strouhal number is disappointingly large, since we would expect a value near .2 in this regime, corresponding to the steady flow case. However, this apparent discrepency is misleading and comes about because Sarpkaya's data reflects not the vortex shedding frequency, but rather the lift force frequency. We will clarify this state-ment by the following analysis of the expected frequency of the lift force, Equation (3.3), and show that satisfactory agreement between the Strouhal numbers is in fact found.

Using the definition of expected frequency for a random process, see for example Crandall and Mark (1963), the expected frequency for the lift force can be found as

$$\overline{\omega}_\ell = \frac{\int_{-\infty}^{\infty} \omega'^2 S_L(\omega') \, d\omega'}{\int_{-\infty}^{\infty} S_L(\omega') \, d\omega'} \tag{3.5}$$

where $\overline{\omega}_\ell$ is the expected lift force frequency and $S_L(\omega')$ is the power spectrum of the lift force. We note that for a narrow band process, the expected frequency corresponds to the average time between zero crossings. The power spectrum, $S_L(\omega')$, is approxi-mated by employing the principle of stationary phase. A concise presentation of the approximate integration method can be found in Vakman (1968), but here we shall only make use of the conceptual result.

Briefly, the principle of stationary phase demonstrates that the power spectral density of the function

$$f(t) = a(t) \sin \omega_c(t) t$$

where $\omega_c(t)$ is the frequency function of $f(t)$

at some frequency ω is

$$S(\omega') \simeq a^2(t_o) * TDF$$

t_o is defined by $\omega_c(t_o) = \omega'$ and TDF is the "time density function"

of $\omega_c(t)$. In other words, the energy at ω is proportional to the

amplitude squared of the function when the instantaneous frequency

is ω' and the fraction of time the frequency function, $\omega_c(t)$,

spends between ω' and $\omega' + \Delta\omega'$ for the limit of $\Delta\omega' \to 0$. An important

assumption employed above is that the function $f(t)$ oscillates

much faster than the amplitude function $a(t)$. For many cases of

interest in the vortex problem this is not strictly true, as we

shall see below.

Assuming a sinusoidal flow so that $u = A_o \omega \sin \omega t$, we

see from Equation (3.3) that

$$\omega_c(t) = \frac{2\pi N_s A_o \omega}{D} \sin \omega t$$

and

$$a(t) = \tfrac{1}{2} \rho \hat{C}_L (A_o \omega)^2 DL \sin^2 \omega t$$

For the frequency restriction to be satisfied during most of a

cycle, we would like $\dfrac{2\pi A_o}{D} N_s \omega$ to be much larger than ω or

$$\frac{2\pi A_o}{D} N_s = N_{KC} N_s >> 1 \qquad\qquad (3.6)$$

In fact, as stated before, the important parameter in vortex

formation is fluid excursion amplitude, even though the frequency

of shedding is defined by the speed. If the amplitude is not

large enough, even though the shedding frequency may be quite

high, no vortices will be shed. If there is a small mean flow,

even though the mean fluid speed is much lower than the peak

flow values, the vortex shedding process will effectively filter

the time varying fluid motions if the above criterion, Equation

(3.6), is not satisfied, i.e., vortex shedding will be controlled

by the mean flow. In this case, the lift force spectrum will be

an impulse at the shedding frequency predicted from the mean

flow, essentially independent of the oscillating flow. With

this restriction in mind, we shall look at the predictions of

the stationary phase model.

If we let $\omega_c(t) = \omega_m \sin \omega't$ where ω_m is the amplitude

of the frequency function, then the fraction of time which the

function $\omega_c(t)$ is less than ω is

$$CDF(\omega) = \tfrac{1}{2} + \frac{1}{\pi} \sin^{-1}\frac{\omega}{\omega_m} \qquad \text{for } |\omega| \leq \omega_m$$
$$= 0 \qquad \qquad \text{for } \omega < -\omega_m$$
$$= 1 \qquad \qquad \text{for } \omega > \omega_m$$

where CDF is the "cumulative density function". The time density

function, $TDF(\omega)$, is the derivative of $CDF(\omega)$ with respect to ω,

so that

$$TDF(\omega) = \frac{1}{\pi}\left(\omega_m^2 - \omega^2\right)^{-\frac{1}{2}} \qquad |\omega| \leq \omega_m$$

Applying the principle of stationary phase to Equation (3.3), we

find upon assuming $u = U_{(max)}\sin \omega t$, that

$$S_L(\omega') = \left(\tfrac{1}{2}\rho \hat{C}_L DL U_{(max)}^2\right)^2\left(\frac{\omega'}{\omega_m}\right)^q \frac{\left(\omega_m^2 - \omega'^2\right)^{-\frac{1}{2}}}{\pi} \qquad |\omega'| \leq \omega_m$$

where we have used the fact that $\frac{\omega'}{\omega_m} = \sin \omega t$

in which $\omega_m = \frac{2\pi\, U_{(max)}\, N_s}{D}$. $S_L(\omega')$ is plotted in Figure 3.9.

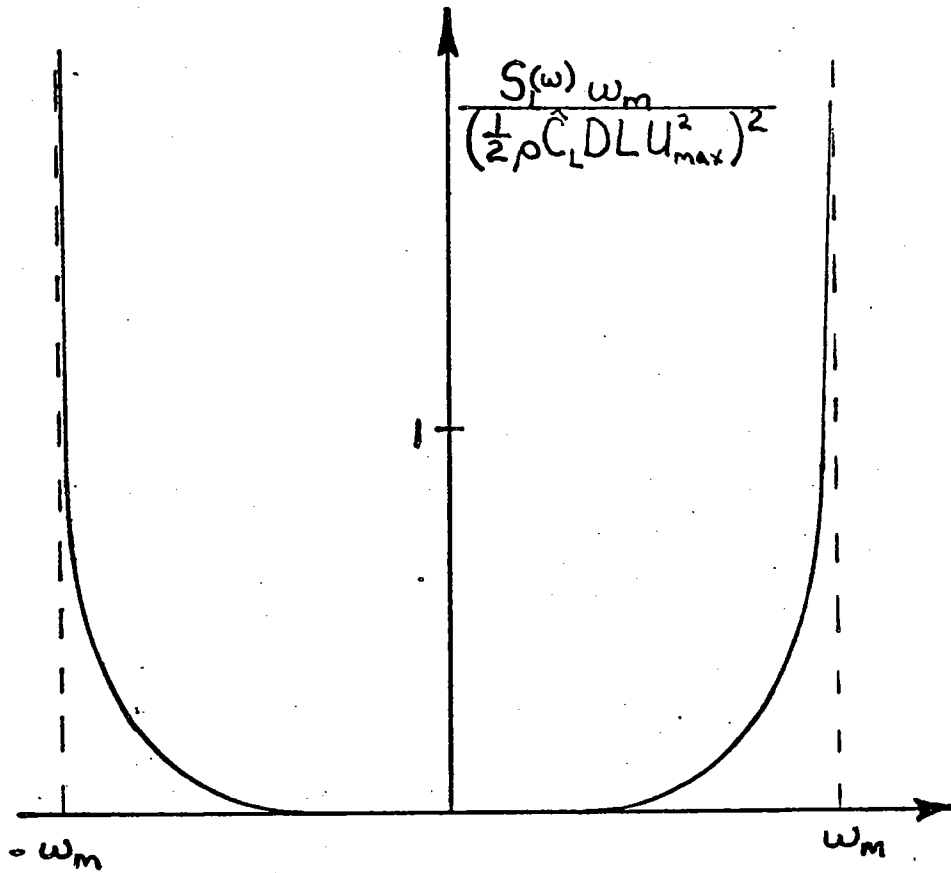Computing the expected frequency of $S_L(\omega')$ using

$$\frac{S(\omega)\,\omega_m}{\left(\frac{1}{2}\rho\hat{C}_L DLU_{max}^2\right)^2}$$

Figure 3.9 Power spectrum of vortex shedding
in harmonic flow

Equation (3.5) we find that $2\pi \bar{f}_{\ell} = \bar{\omega}_{\ell} = .91\omega_m$. Thus, the Strouhal

number based on the maximum oscillatory velocity, $\dfrac{\bar{f}_{\ell} D}{U_{(max)}}$,

should be nearly equal to the constant flow Strouhal number.

Sarpkaya, in fact, finds that $\dfrac{\bar{f}_{\ell} D}{U_{(max)}} = .22$ for all of the low

Reynolds number range, which is gratifyingly close to the fixed

cylinder steady flow Strouhal number, $N_s \simeq .21$. In fact, now

that we see that the frequency content of the lift force is dominated

by the frequency corresponding to the maximum oscillatory velocity,

it is quite reasonable for the Strouhal number to increase as the

Reynolds number based on $U_{(max)}$ enters the critical flow region.

This is a phenomenon similar to what we see in the fixed cylinder

steady flow Strouhal number, see Figure 3.1.

3.3.2.2 Lift Moment Spectrum

We now look at the lift force spectrum for the case of

a cylindrical strip of length L under 2 -dimensional random

waves with a steady co-linear current. The probability density

function for the velocity under a Gaussian random wave system

is also Gaussian, assuming linear wave theory. Assuming ergo-

dicity, the time density function and the probability density

function of the velocity are identical. The power spectrum of

the lift force is therefore

$$S_{\ell}(\omega') = (\tfrac{1}{2}\rho \hat{C}_{\ell} D L \, \sigma_u^2)^2 \left(\tfrac{\omega'}{\omega_{\sigma}}\right)^4 \frac{1}{\sqrt{2\pi}\, \omega_{\sigma}} \times \qquad (3.7)$$

$$\exp\left(-\tfrac{1}{2}\left(\tfrac{\omega'-\omega_{\mu}}{\omega_{\sigma}}\right)^2\right)$$

where $\quad \omega_{\mu} = 2\pi \dfrac{N_s U_0}{D} \quad$ and $\quad \omega_{\sigma} = 2\pi \dfrac{N_s \sigma_u}{D}$

and U_0 and σ_u are the mean and standard deviation of the fluid

velocity, respectively. Notice that the limit as $\sigma_u \to 0$ is an

impulse at the frequency corresponding to the mean velocity, as

it should be. Some examples of possible spectra are plotted in

Figure 3.10.

The effects of lengthwise correlation for the strip

model proposed can be described using the properties of a

spatially correlated narrow band process, as discussed by Blevins

and Burton (1976). However, the amount of data on the correla-

tion coefficient is small, so that this aspect of the problem

will not be pursued. We shall in fact assume that the correla-

tion length is infinite. For the experimental system described

in Section 5, this assumption is adequate, since most of the

moments are due to forces near the top of the spar, only a few

diameters long.

The lift moment spectrum can readily be obtained from

the cross spectrum of the lift forces. Thus, we write the power

spectrum of the lift forces as a spatial cross spectrum

$$S_L(z_1, z_2, \omega') = \frac{1}{2}\rho \hat{C}_L D \sigma_u^2(z_1) \omega_\sigma^{-5/2}(z_1) \times \qquad (3.8)$$

$$\frac{1}{2}\rho \hat{C}_L D \sigma_u^2(z_2) \omega_\sigma^{-5/2}(z_2) \frac{\omega^4}{\sqrt{2\pi}} \times$$

$$\exp\left[-\frac{1}{4}\left(\frac{\omega' - \omega_M(z_1)}{\omega_\sigma(z_1)}\right)^2 - \frac{1}{4}\left(\frac{\omega' - \omega_M(z_2)}{\omega_\sigma(z_2)}\right)^2\right] \times$$

$$r_c(z_1, z_2, \omega)$$

where r_c is the spanwise correlation. Notice that for $z_1 = z_2$

Equation (3.8) is identical to Equation (3.7) except for L^2. As

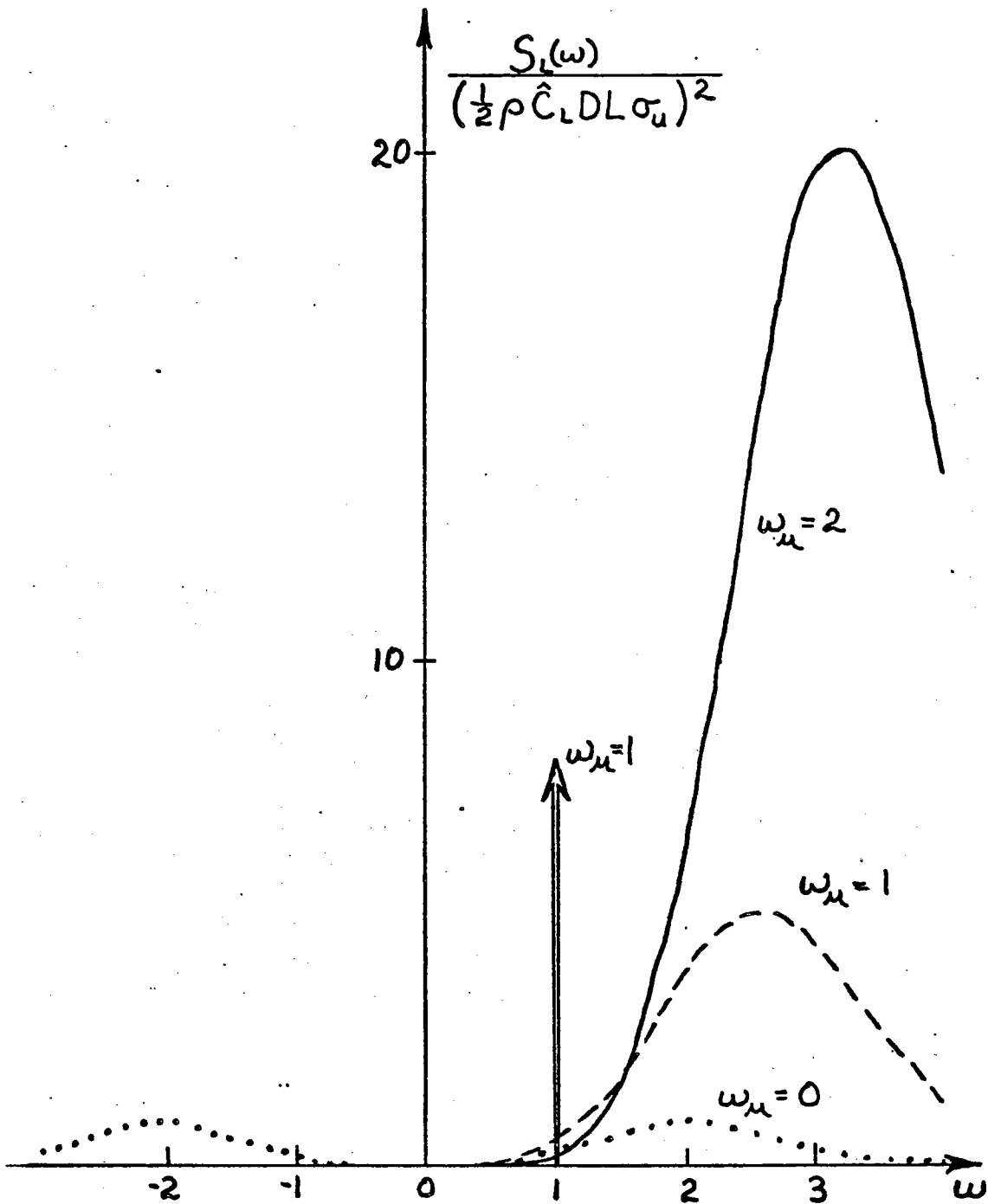mentioned above, we will use an infinite correlation length which

Figure 3.10 Some examples of lift force spectra under Gaussian waves, $\omega_\sigma = 1$. The impulse represents a case where the fluid oscillation frequencies are greater than the shedding frequencies

implies $r = 1$. The lift moment spectrum is then obtained from the cross spectrum, as

$$S_{M_L}(\omega') = \int_o^h \int_o^h S_L(z_1, z_2, \omega) z_1 z_2 \, dz_1 \, dz_2 \qquad (3.9)$$

where z is the "mode shape" of the spar.

We approximate the vortex drag force in the same manner as the lift force. For the alternate shedding mode, the lift force spectrum is transformed to twice the shedding frequency and scaled by the drag coefficient to yield a drag spectrum

$$S_{M_{\hat{D}}}(\omega') = \left(\frac{\hat{C}_D}{\hat{C}_L}\right)^2 \int_o^h \int_o^h S_L(z_1, z_2, \omega/2) z_1 z_2 \, dz_1 \, dz_2 \qquad (3.10\ a)$$

The paired shedding mode drag force spectrum is generated by transforming the lift spectrum to four times the vortex shedding frequency, that is

$$S_{M_{\hat{D}}}(\omega') = \left(\frac{\hat{C}_D}{\hat{C}_L}\right)^2 \int_o^h \int_o^h S_L(z_1, z_2, \omega/4) z_1 z_2 \, dz_1 \, dz_2 \qquad (3.10\ b)$$

In employing these spectra, we must decide whether the paired or alternate shedding will dominate. This can be done by assuming that the process which causes the largest motions will dominate. Notice that the paired shedding will dominate only when its peak is near the system natural frequency and that there will be no lift forces with paired shedding.

3.3.3 Equations of Motion

We shall now write the equations of motion of the spar, incorporating viscous effects into Equation (2.11)

$$\ddot{\psi} I_T + \dot{\psi} C_T + \psi \mathcal{H} = M_W + M_D + M_{\hat{D}} \qquad (3.11)$$

$$\ddot{\delta} I_T + \dot{\delta} C_T + \delta \mathcal{H} = M_{\hat{L}}$$

where

$$I_T = I + C_a \rho \pi R^2 \frac{h^3}{3}$$

$$C_T = \int_0^h C_D \tfrac{1}{2} \rho D U_m z^2 dz$$

$$\mathcal{H} = \rho g \pi R^2 h - M z_{cg}$$

in which C_a is the added mass coefficient. M_L and M_D are defined

by their spectra, Equations (3.9) and (3.10) respectively

$$M_w = (1 + C_a) \rho g A \frac{\pi R^2}{k \cosh kh} (kh \sinh kh - \quad (3.12)$$
$$\cosh kh + 1) e^{-i(kU_0 + \omega)t}$$

$$M_D = \int_0^h \tfrac{1}{2} C_D \rho u(z) U_m D z dz$$

with $\quad U_m = [(u(z) - \dot{\psi} z)^2 + (\dot{\delta} z)^2]^{1/2}$

and $\quad u(z) = U_0 + i A \omega \frac{\cosh kz}{\sinh kh} e^{-i(kU_0 + \omega)t}$

In the next section we shall assume a spectral form for

the incident wave system and propose an approximate linear tech-

nique for obtaining the response of the spar pendulum in 2-

dimensional random waves and a uniform current.

4. Equivalent Linearization of the Equations of Motion

The analytical methods for investigating linear systems under random excitation are well-developed, compact and efficient, see for example Papoulis (1965). On the other hand, investigation of non-linear systems has been restricted mostly to harmonic excitation or to brute force numerical techniques, although an elegant method for treating randomly excited non-linear systems does exist and involves the expansion of a system response as a functional (Volterra) series, see Bedrosian and Rice (1971). In fact, the entire theory of linear system response involves the investigation of the first term of this functional series, that is, if a system is linear, the series representation degenerates to only one term. The expansion of the system response in a functional series is in fact capable of handling input non-linearities, non-linear waves in the present problem, as well as non-linear system properties.

The method is most useful when the non-linear terms take the form of polynomials, so that only a few terms in the series are needed. However, it is not at all clear that a system involving a magnitude or absolute value function, as in the case considered here, even has a functional series expansion. We shall, therefore, attack Equation (3.10) by linearizing the drag term so that we can employ the techniques for predicting linear system response.

A linearized treatment of this problem is probably

more than adequate considering the linearizing assumptions we
have already made concerning wave kinematics and spar response
and the limited knowledge of the forces exerted by flow around
a bluff body. Linearization of hydrodynamic drag in oscillating
flows has been considered for in-line forces on a fixed cylinder,
see Borgman (1965), and response of a point oscillator, see
Seymour (1974). However, these treatments did not include the
effects of a mean flow or of vortex shedding.

The linearization employed here equates the expected
value of the power exerted on the system by the linearized force
to the expected value of the power exerted on the system by the
non-linear force. That is, we would like to find a linear system
which has the same average energy flow as the non-linear system
in the particular environment of interest. If we look at a
strip of a cylinder which has a displacement x, then, ignoring
transverse motions, we can write the drag force as

$$F_D = \tfrac{1}{2}\rho\, C_D\, DL\, u_r\, |u_r|$$

where u_r = x - u, the relative velocity. This would be linearized

as
$$F_D = \tfrac{1}{2}\rho\, C_D\, DL\, u_r\, U_E$$

where the equivalent velocity, U_E, is chosen so that it satisfies
the following equation:

$$E[\dot{x}\, \tfrac{1}{2}\rho\, C_D\, DL\, u_r\, U_E] = E[\dot{x}\, \tfrac{1}{2}\rho\, C_D\, DL\, u_r\, |u_r|]$$

or

$$U_E = E[\dot{x}\, u_r\, |u_r|] / E[\dot{x}\, u_r]$$

where E[ ] means expected value. This linearization is equivalent

to using the first term of the series solution for wave force
statistics discussed by Borgman (1965). Another possible linear-
ization, used by Seymour (1974), is to minimize the mean square
error in the total drag dissipation. Both expected value and
mean square linearizations lead to almost identical solutions.
The mean square method is biased toward predicting the instanta-
neous power and therefore would probably provide better extremal
statistics. The energy balance implied by the equivalence in
expected power in the first method is physically attractive, and
is the reason for employing it here.

In order to make computations of the expected values,
one must assume a probability density function for the system
response, x in the example above. The velocity of the fluid,
u, will be assumed Gaussian, a generally accepted distribution
for the velocity under random waves. For the linearized system
this would imply a Gaussian output, and calculation of the
expected value is straightforward. In fact, we will also assume
that the non-linear response is approximately Gaussian as well.
In the case of a strong non-linearity, such as the absolute value
in the drag law, there seems to be, at first glance, no reason
to believe that the Gaussian assumption is reasonable. However,
for a narrow band process, one can see that the function $x|x|$
leaves most of the output energy at the same frequencies as the
input, see Figure 4.1. This fact is probably the principle reason
that linearization of hydrodynamic drag appears to perform so
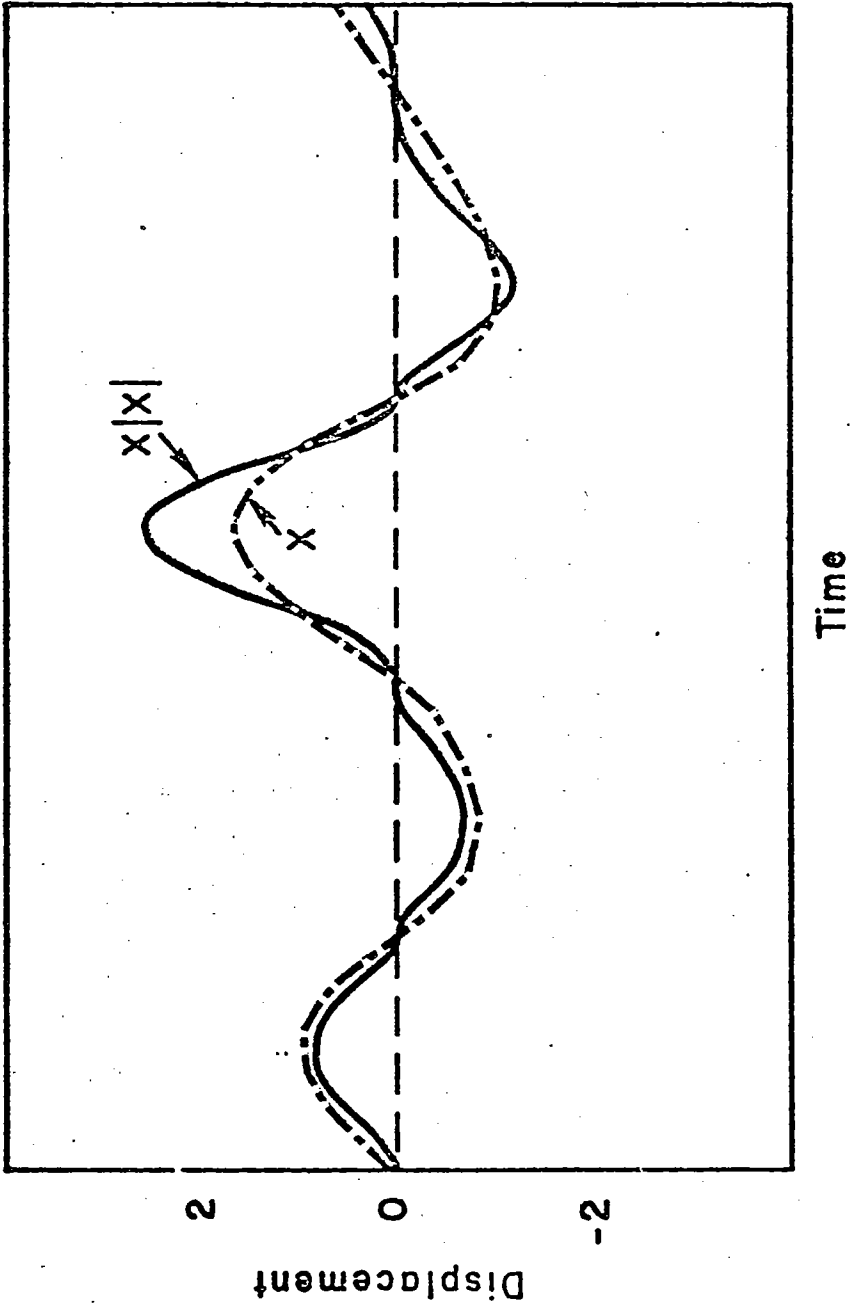
Figure 4.1 Displacement vs. Time for a Narrow Band Process and the output of a "drag law" process

well. That is, a narrow band input, a realistic assumption for ocean surface waves, to the non-linear drag process yields a narrow band output at the same frequencies as the input, much like a linear process. We can, therefore, expect little correlation between frequency bands where there is significant energy, implying a nearly Gaussian response.

In Section 4.1 we shall apply the linearization to a simple analog system which can be thought of as a strip of the spar. We will find that the linearization requires the solution of a set of simultaneous integral equations which we propose to solve iteratively. Convergence of the iterative scheme proposed is discussed in Appendix B. Studying the transfer function of the simple system for various parameter ranges will provide some insight into the solutions of the spar equations. In Section 4.2 we attack the spar governing equations and consideration is given to the linearization of this spatially distributed process. In Section 4.3 we discuss a numerical experiment in which we isolate ourselves from some of the complexities of the real world, and test the performance of the linearization against a numerical simulation. A simplified form of the spar equation is used for this purpose.

4.1 Simple Analog

We shall consider here the linearization of the following equation:

$$\ddot{x} + C(\dot{x}-u)|\dot{x}-u| + x = F'\dot{u} \qquad (4.1)$$

As we stated in the introduction to this section, this may be considered the dimensionless equation for a strip of the spar with no vortex effects, where time is multiplied by the natural frequency and length is divided by the diameter. We would find that in this case

$$F' = (1+C_a)/(\frac{\rho_c}{\rho} + C_a) \qquad (4.2\ a)$$

and

$$C = \frac{2}{\pi} C_D/(\frac{\rho_c}{\rho} + C_a) \qquad (4.2\ b)$$

where ρ_c is the density of the strip of cylinder and the added mass coefficient $C_M = 1 + C_a$. The forcing function, u, is characterized as a Gaussian random process with a power spectral density, $\omega^2 S_{A_o}(\omega)$, and a mean m_u. We begin by substituting into Equation (4.1) the equivalent velocity U_E for the absolute value of the relative velocity.

$$\ddot{x} + CU_E\dot{x} + x = F'\dot{u} + CU_E u \qquad (4.3)$$

Employing harmonic analysis, we let $u = iwA_o e^{-i\omega t}$ and $x = e^{-i\omega t}$ where X is complex, and solve for the transfer function

$$\frac{X}{A_o} = \frac{-\omega^2 F' - i\omega CU_E}{(1-\omega^2) - i\omega CU_E} \qquad (4.4)$$

We can also compute the transfer function for the relative velocity $x - u = U_r e^{-i\omega t}$ which will be of use in finding the equivalent velocity.

$$\frac{U_r}{A_o} = -i\omega \left(\frac{X}{A_o} - 1\right) \qquad (4.5)$$

Using the theory of linear random processes, it is easy to find the spectrum of the output

$$S_x(\omega) = \left|\frac{X}{A_o}\right|^2 S_{A_o}(\omega)$$

and the relative velocity spectrum

$$S_{u_r}(\omega) = \left|\frac{U_r}{A_o}\right|^2 S_{A_o}(\omega) \qquad (4.6)$$

where $S_{A_o}(w)$ is the spectrum of the input amplitude.

We now consider the value of the equivalent velocity to be used

in the previous analysis. The linearizing constraint of equiva-

lent expected power can be written as

$$E[U_E \dot{x} u_r] = E[\dot{x} u_r |u_r|] \qquad (4.7)$$

As mentioned earlier, we will compute the expectations in Equation

(4.7) by assuming that u_r is a Gaussian process. The PDF, proba-

bility density function, of u_r is therefore defined by its mean,

m_{u_r}, and its standard deviation, σ_{u_r}. Since we assume that

there is no mean velocity of the system, $x = o$, the mean of the

relative velocity is simply the mean of the incident velocity,

m_u. From the theory of random processes we know that

$$\sigma_{u_r}^2 = \int_{-\infty}^{\infty} S_{u_r}(\omega) \, d\omega \qquad (4.8)$$

where $S_{u_r}(w)$ is defined by Equation (4.6). We can now write

Equation (4.7) in terms of probability integrals, where we

assume that x and u_r are jointly Gaussian with correlation ρ',

that is

$$U_E \iint_{-\infty}^{\infty} \dot{x} u_r \, PDF_{\dot{x} u_r} \, d\dot{x} \, du_r = \iint_{-\infty}^{\infty} \dot{x} u_r |u_r| \, PDF_{\dot{x} u_r} \, d\dot{x} \, du_r$$

where

$$PDF_{\dot{x} u_r} = \left(2\pi \sigma_{\dot{x}} \sigma_{u_r} \sqrt{1-\rho'^2}\right)^{-1} \times$$
$$\exp\left\{-\frac{1}{2}\frac{1}{1-\rho'^2}\left[\left(\frac{\dot{x}}{\sigma_{\dot{x}}}\right)^2 - 2\rho\left(\frac{\dot{x}}{\sigma_{\dot{x}}}\right)\left(\frac{u_r - m_u}{\sigma_{u_r}}\right) + \left(\frac{u_r - m_u}{\sigma_{u_r}}\right)^2\right]\right\}$$

We have assumed that x has a zero mean. Solving for the equiva-

lent velocity, we find that

$$U_E = \left(\sqrt{2\pi}\ \sigma_{u_r}^3\right)^{-1} \int_{-\infty}^{\infty} |u_r| u_r (u_r - m_u) e^{-\frac{1}{2}\left(\frac{u_r - m_u}{\sigma_{u_r}}\right)^2} du_r \qquad (4.9)$$

Equation (4.9) can be easily integrated when there is no mean

incident velocity so that

$$U_E = \sqrt{\frac{8}{\pi}}\ \sigma_{u_r} \qquad \text{for}\ \ m_u = 0 \qquad (4.10)$$

We can also find the limit for $m_u \gg \sigma_{u_r}$ is $U_E = 2m_u$.

Equations (4.8) and (4.9) are a pair of simultaneous

equations with unknowns U_E and σ_{u_r} . We propose to obtain the

solution of these equations by successive approximation. That

is, we guess a value for U_E , compute a response and find a new

value of U_E , iterating until some error criterion for U_E is

satisfied. We shall consider the convergence of such a routine

for this simple model in Appendix B.

Before moving on, it is instructive to consider the

transfer function of the simple analog, Equation (4.4). This

function is plotted in Figures 4.2 a, b, c for various values

of equivalent velocity and three values of relative density,

$\frac{\rho_c}{\rho}$. For the purpose of this discussion we have chosen to let

$C_a = C_D = 1$. A more general parameterization might have used

CU_E and F' as parameters but the physical significance of relative

density and linearized velocity seemed more apparent. In fact,

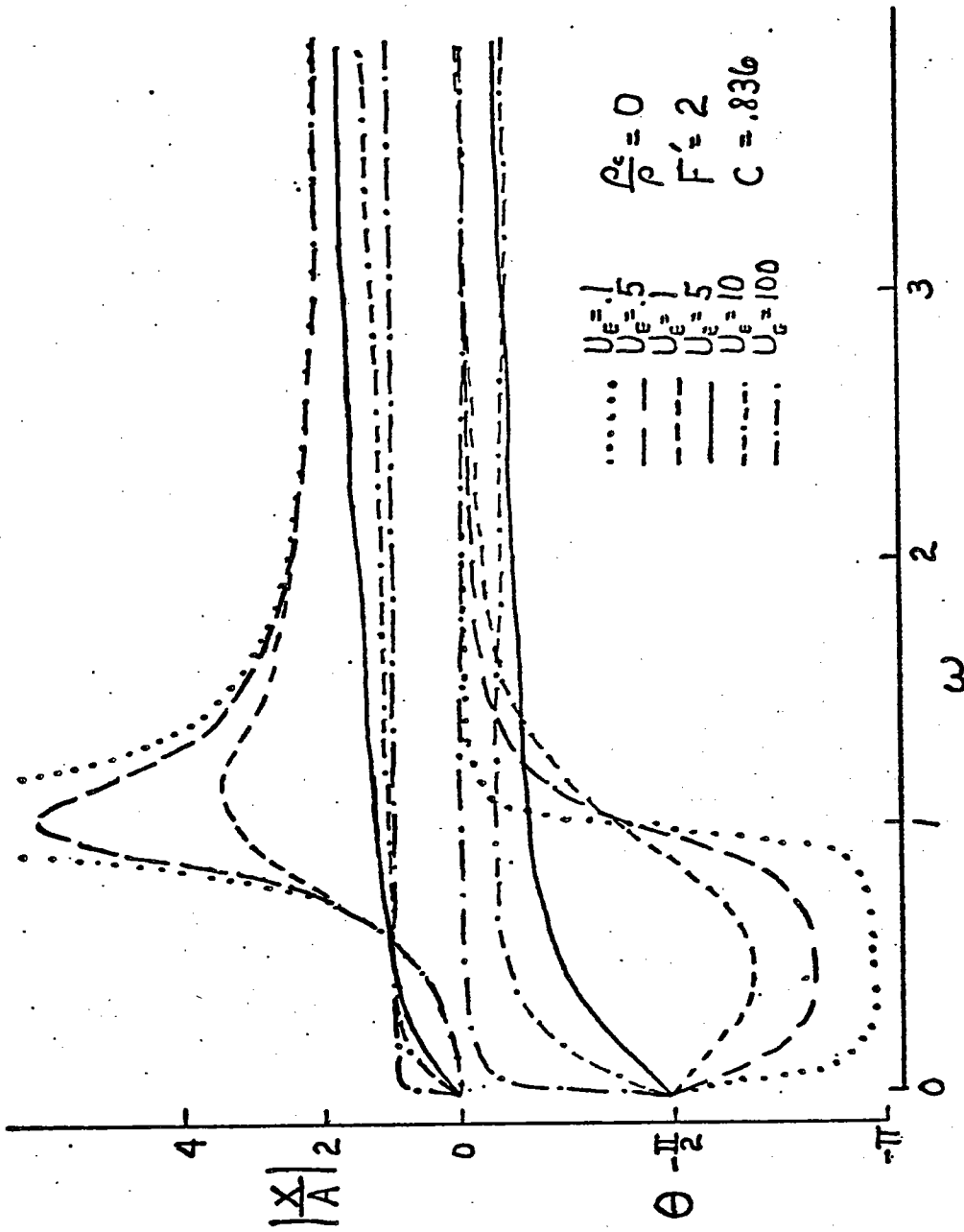the two parameterizations are equivalent and merely require a

Figure 4.2 a   Transfer function of linearized analog for various values of equivalent velocity, $\frac{\rho_e}{\rho} = 0$.

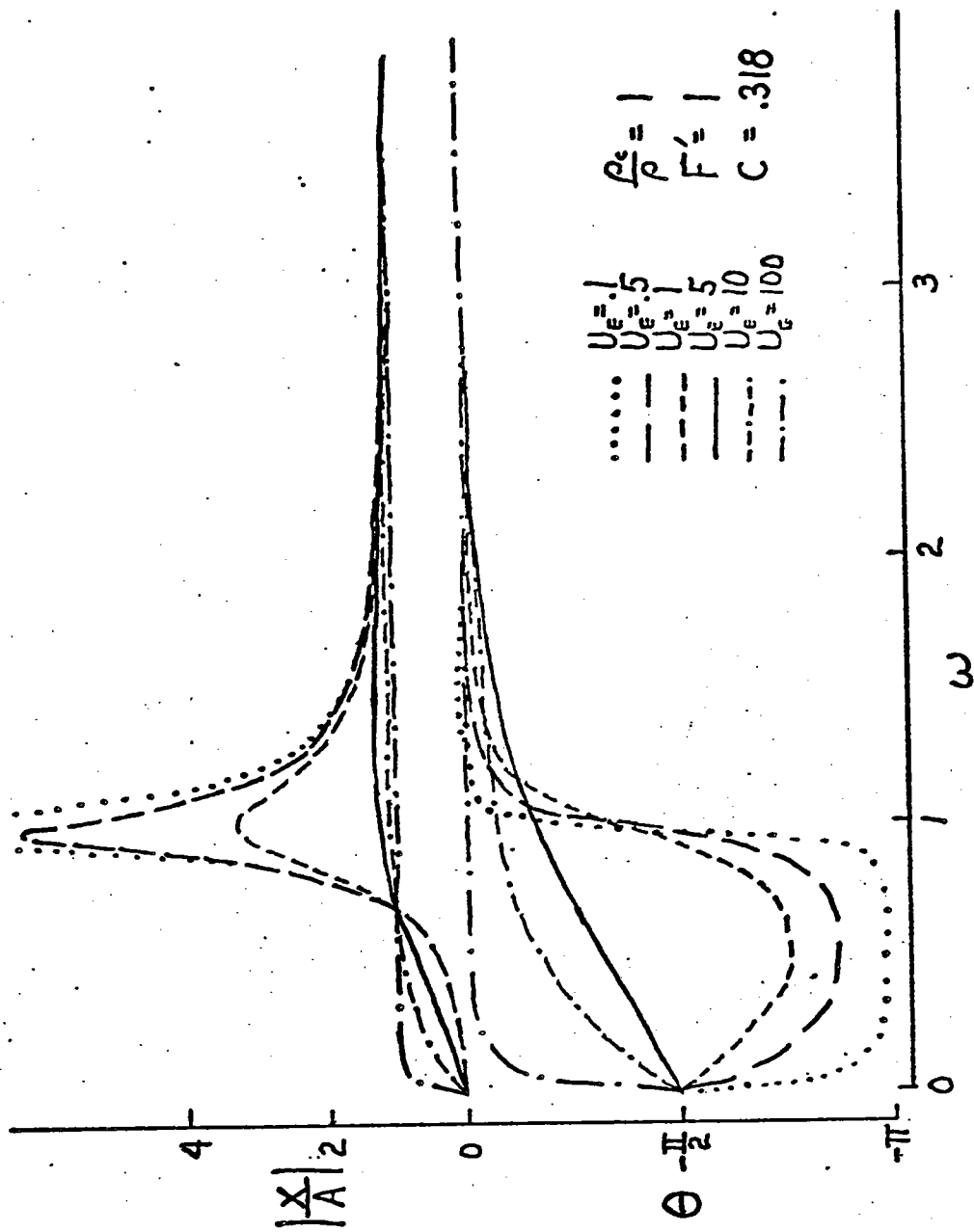**Figure 4.2 b** Transfer function of the linearized analog for various values of equivalent velocity, $\frac{\rho_c}{\rho} = 1$.
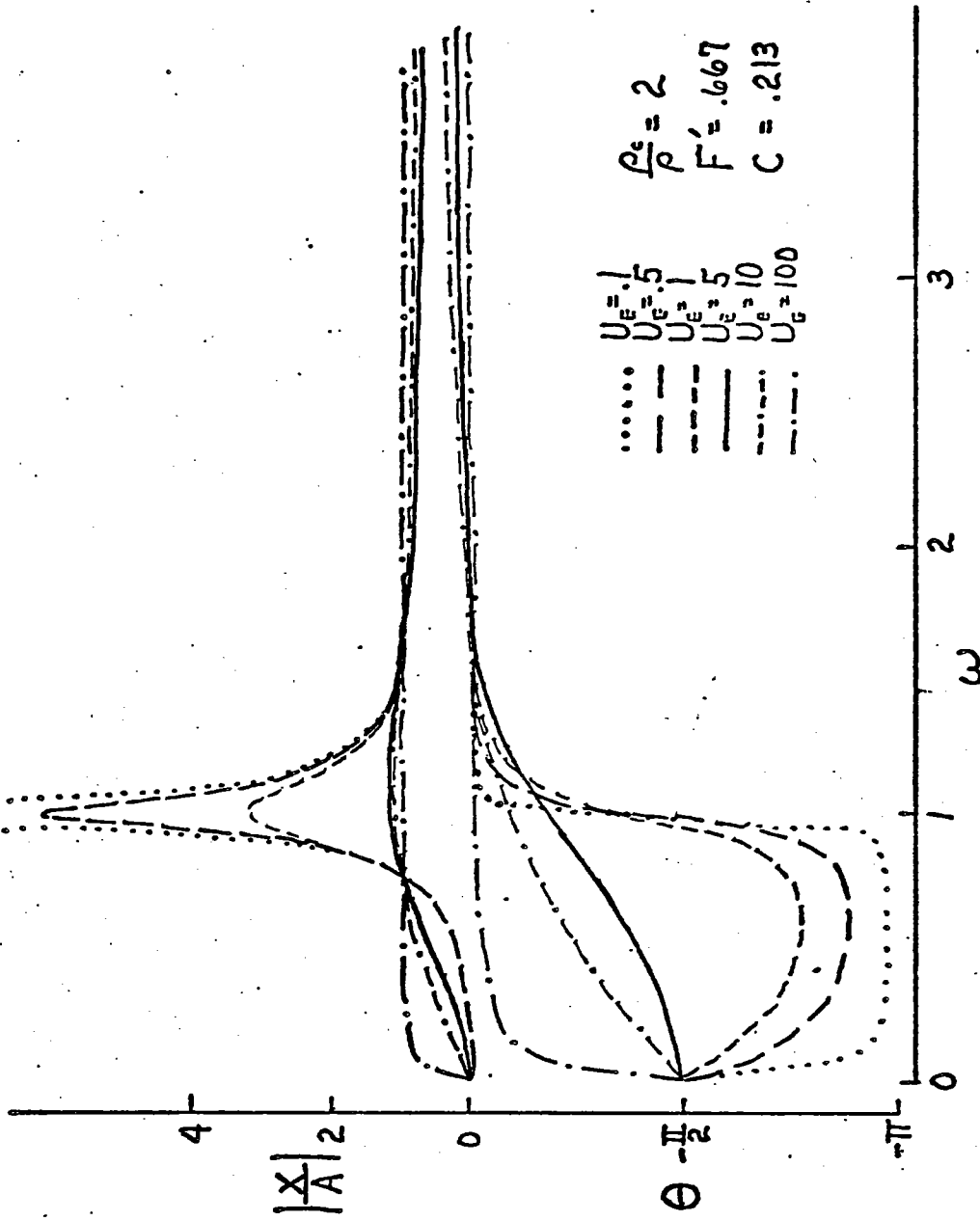
Figure 4.2 c   Transfer function of the linearized analog for
various values of equivalent velocity, $\frac{\rho_e}{\rho} = 2$.

relabelling of the figures. The most striking feature of this transfer function is its division into three distinct regions by the real roots of $\omega^4 = (1 - F'^2)^{-1}$. These regions can be best seen in Figure 4.2 c, where both positive roots are real. The second important feature is the limit of the response as the equivalent velocity, U_E , goes to infinity. That is, as the viscous forces predominate, the motions of the body are in phase and of equal amplitude with the motions of the fluid. The body is advected by the fluid, exactly as we would expect.

The first region, $0 < \omega < (1 + F')^{-\frac{1}{2}}$, always exists and is characterized by a balance between the viscous exciting force and the stiffness of the system. The curve representing the lower limit of response in this region is the balance of inertial driving force and system stiffness, typical of the usual single input single degree of freedom system studied in elementary vibration theory. By comparing this region in Figures 4.2 a, b, c we can see that, as the relative density decreases, the viscous forces predominate at lower frequencies. This is due to an increase in the dimensionless drag coefficient, C. The second region is an inertial forcing region, and may extend to infinity if $F' \geq 1$. In this region, the upper bound of the response is controlled by the inertial driving force, and viscous forces act to retard the response and bring it down to unity. The limit of the response for high frequencies and low damping is always F' . We see now that the third region, $\omega > (1 - F')^{-\frac{1}{2}}$, which exists

when F' is less than 1, has a lower limit specified by inertial
forces where increasing vicsous forces act to raise the response
to unity. We see, therefore, that the action of large viscous
forces is to try and bring the response of the system to unity,
and that around resonance, response always decreases. In this
light, it is not too surprising that the linearization is well-
behaved, rapidly yielding a solution under successive approxima-
tions.

4.2 Linearized Analysis of the Pendulum Spar

There is only one important difference between the
pendulum spar and the dimensionless analog of the previous sec-
tion. The spar involves a spatial process with significant
gradients. That is, for the 2 -dimensional wave climate which
we will consider, the velocity profile is in no way uniform, and
it is necessary to consider an equivalent velocity "profile". In
fact, we can consider each strip of the spar as an oscillator
similar to the dimensionless analog, where all of the strips are
coupled, in this case by being constrained to move as a rigid
body. We begin by considering the implications of this on the
analog equation, and then we will write down the linearized
solution of the spar.

4.2.1 Linearized Spatial Process

The spatially varying analog equation looks like

$$\ddot{\xi} + \int_0^h C \,|\Gamma\dot{\xi} - u(z)|\,(\Gamma\dot{\xi} - u(z))\,dz + \xi$$
$$= \int_0^h F\,\dot{u}(z)\,dz$$

where ξ is the "modal displacement", angle of inclination for

the spar, and Γ is the "mode shape", z for the spar. This

equation is linearized to

$$\ddot{\xi} + C_\xi \dot{\xi} + \xi = \int_0^h \left[F\,\dot{u}(z) + C\,U_E(z)\,u(z) \right] dz$$

where

$$C_\xi = \int_0^h C\,\Gamma\,U_E(z)\,dz$$

We see now that there is an equivalent velocity "profile" which

we must compute in a similar manner to the equivalent velocity

of the point problem. The response of this linearized system

to some random input involves a straightforward computation which

will yield a relative velocity spectrum which is a function of

depth. From this spectrum we can obtain the standard deviation

of the relative velocity as a function of depth and making the

Gaussian assumption as before, we use Equation (4.9) to compute

an equivalent velocity profile, $U_E(z)$. An iterative procedure

similar to that discussed in Section 4.1 could be used to find

the correct profile.

4.2.2 Linearization Algorithm

The spar equations of motion, Equations (2.11) are

already in a linearized form. All that we need do is replace

the velocity magnitude, U_m , by the equivalent velocity, U_E .
We shall discuss the linearized solution of these equations in
random waves and a uniform current, by describing the algorithm
used to find the solution.

We begin by assuming some form for the input wave
spectrum, say $S_A(\omega')$. The input velocity spectrum is obtained
from the amplitude spectrum by assuming linear wave theory, so
that

$$S_u(z,\omega) = | H_u(\omega')|^2 S_A(\omega')$$

where

$$H_u(\omega') = i\,\omega'\,\frac{\cosh kz}{\sinh kh}$$

with

$$\omega' = \omega - kU_0$$

in which we note that ω is the Doppler shifted frequency of the
wave

and

$$\omega'^2 = g k \tanh kh$$

An initial estimate of the equivalent velocity is made by
assuming that the spar is fixed, that is, we just use the mean
square of the input velocity spectrum. A summation integration
of the power spectrum $S_u(z,\omega)$ over all frequencies where there is
significant energy is used to find the mean square of the velocity
at various depths. The depth spacings used for the computations
presented later are given in Table 4.1. The depth is divided
into regions of length $2^{-n}h$ to simplify spatial integrations,
with the densest sampling near the surface where the largest

TABLE 4.1

Fraction of where calculations are made on the spar.

POINT	z/h
1	1.0
2	.9375
3	.875
4	.75
5	.625
6	.5
7	.25

changes in the velocity spectra will occur. The mean square

profile obtained from integrating $S_u(z,\omega)$ is then used to obtain

an equivalent velocity profile by applying Equation (4.9). The

integration of the probability integral is accomplished with a

seven point Simpsons rule applied at 1/3 standard deviation

intervals to ± 4 standard deviations. Now that there is a trial

equivalent velocity profile, we can calculate the response of

the spar, and obtain a new approximation of $U_E(z)$.

Using the relative velocity standard deviations, it

is now possible to calculate the cross spectrum of the vortex

lift force, Equation (3.8), at each sample depth and then to

calculate the vortex lift moment and drag moment spectra,

Equations (3.9) and (3.10) respectively. We can also calculate

the inertial moment and "steady" drag moment spectra by applying

the transfer functions of Equation (3.12) to the input spectrum,

that is

$$S_M(\omega) = |H_M(\omega')|^2 \, S_A(\omega')$$

where

$$H_M(\omega') = (1+C_a)\rho g \, \frac{\pi R^2}{k \cosh kh} \left(kh \sinh kh - \cosh kh + 1\right) +$$
$$\tfrac{1}{2} i \rho D \int_0^h C_D \, \omega' \frac{\cosh kh}{\sinh kh} \, U_E(z) \, z \, dz$$

From Equation (3.11) we can see that the transfer functions for

ψ and δ are identical so that

$$H_\delta(\omega) = H_\psi(\omega)$$

and

$$H_\psi(\omega) = ( )\{ - \omega^2 I_T - i\omega C_T)^{-1}$$

where $\{$, I_T and C_T are defined in Equation (3.11). We now use
this transfer function to compute the response spectrum of the
spar.

$$S_\psi(\omega) = |H_\psi(\omega)|^2 [S_M(\omega) + S_{M_b}(\omega)]$$
$$S_\delta(\omega) = |H_\delta(\omega)|^2 [S_{M_\tau}(\omega)]$$

In order to compute the in-line relative velocity
spectrum, we must be a bit careful since the spar response is
not independent of the input velocity spectrum. Note that if
it were independent we could simply compute the spar velocity
spectrum at any depth, multiply by $(\omega z)^2$, and add it to the
input velocity spectrum. We have already presented the correct
relative velocity transfer function in the discussion of the
simple analog, Equation (4.5). Applying this to the spar, we
find

$$S_{(z\psi-u)}(z,\omega) = |z\omega H_M(\omega') H_\psi(\omega) - H_u(\omega')|^2 S_A(\omega') +$$
$$(z\omega)^2 |H_\psi(\omega)|^2 S_{M_b}(\omega)$$
$$S_{z\delta}(z,\omega) = (z\omega)^2 |H_\delta(\omega)|^2 S_{M_\tau}(\omega)$$

The standard deviation of the relative velocity is then just the
sum of the two integrated spectra, since ψ and δ are orthogonal,
so that

$$\sigma_{u_r}^2(z) = \int_{-\infty}^{\infty} [S_{(z\psi-u)}(z,\omega) + S_{z\delta}(z,\omega)] \, d\omega$$

It is now clear that we can compute a new equivalent velocity
profile, check for convergence and repeat the response calculation

if necessary.

We have, as yet, ignored the question of mean inclination of the spar. However, the idea of equating power flows through the oscillator does not make sense at D.C., since there is no energy flow, only a force balance. For calculating the mean angle of inclination, we shall therefore turn to an energy balance in the flow field. We shall assume that the expected value of the flow dissipation from a linearized viscous force is equal to the expected value of the flow dissipation from the non-linear force, therefore

$$E[u_r^2 \, U_{0E}(z)] = E[|u_r^3|]$$

or, evaluating the expected values

$$U_{0E}(z) = [\sqrt{2\pi} \, \sigma_{u_r}(\sigma_{u_r}^2 + m_u^2)]^{-1} \times$$
$$\int_{-\infty}^{\infty} |u_r^3| \exp[-\tfrac{1}{2}(\frac{u_r - M_u}{\sigma_{u_r}})^2] \, du_r$$

Note that $U_{OE}(z)$ is computed after we determine the spar response, so that we use the final computation of $\sigma_{u_r}(z)$ and that in general $U_{OE}(z) \neq U_E(z)$. The mean angle of inclination is then computed as a force balance using the linearized drag law.

4.3 Numerical Experiment

In order to get some idea of how well the linearization performs under ideal conditions, a numerical simulation of the spar equations for various environments is performed. The effects of vortex shedding are ignored, that is $C_D = C_L = 0$, and a relatively simple 2-dimensional problem results. The actual spar

properties used in the numerical experiment are those of the circular cylinder experimental system described in the next section, and the important properties are

f_o = natural frequency = .75 Hz

D = 10 cm

h = 1.1 m

It is also assumed that $C_D = C_A = 1$ and that $\rho = 1000$ kg/m^3. The input environments used are scaled Pierson-Moskowitz (P-M) Spectra which were used in the experimental work plus some improperly scaled P-M spectra which provided large amplitude waves necessary for large viscous forces. The full-scale P-M spectrum is

$$S_{P-M}(\omega) = 8.1 \times 10^{-3} \frac{g^2}{|\omega^5|} \exp\left[-.74 \left(g/V\omega\right)^4\right]$$

where V is the spectral wind speed. The scaled spectrum is scaled in time by a factor of 10 and in length by a factor of 100, so that

$$S'_{P-M}(\omega) = .81 \frac{g^2}{|\omega^5|} \exp\left[-.74 \left(g/.1V\omega\right)^4\right]$$

Various uniform currents are also used, and the above spectrum is corrected for the doppler shift in wave frequency, due to the uniform current.

The numerical simulation utilizes a Fast Fourier Transform to produce a coherent velocity profile time-series and acceleration moment time-series. The spar governing equation, Equation (3.11), is then integrated numerically using these forcing functions.

The scaled P-M spectrum is divided into 1024 bands with the maximum frequency at 20 Hz, see Figure 4.3, so that each band has a width of $\Delta\omega \simeq .12 \frac{rad}{sec}$. If we assign a random phase, ϕ, to each band, we can obtain a pseudo-Gaussian simulated amplitude transform as follows

$$A_n = [S_{P-M}(\omega') \Delta\omega']^{1/2}$$
$$\omega' = \omega - kU_0$$
$$\omega = n\Delta\omega$$

and

$$\Delta\omega' = \Delta\omega / \frac{\partial\omega}{\partial\omega'}$$
$$\omega'^2 = gk \tanh kh$$

Note that much of the high-frequency range of the spectrum in Figure 4.3 is nearly zero. This has the effect of generating a "densely sampled" time series when the amplitude transform is inverted, making the numerical integration simpler. The velocity transform at z is obtained by applying linear wave theory to the amplitude transform, so that

$$u_n(z) = i\omega' \frac{\cosh kz}{\sinh kh} A_n$$

The depths used for calculations are the same as those used in the linearization, and are given in Table 4.1. The velocity transform is then inverted to obtain a velocity profile time series. A typical time series is shown in Figure 4.4. The acceleration moment time series is obtained in a similar manner so that

$$M_n = (1+C_a)\rho g \frac{\pi R^2}{k \cosh kh} (kh \sinh kh - \cosh kh + 1)A_n$$
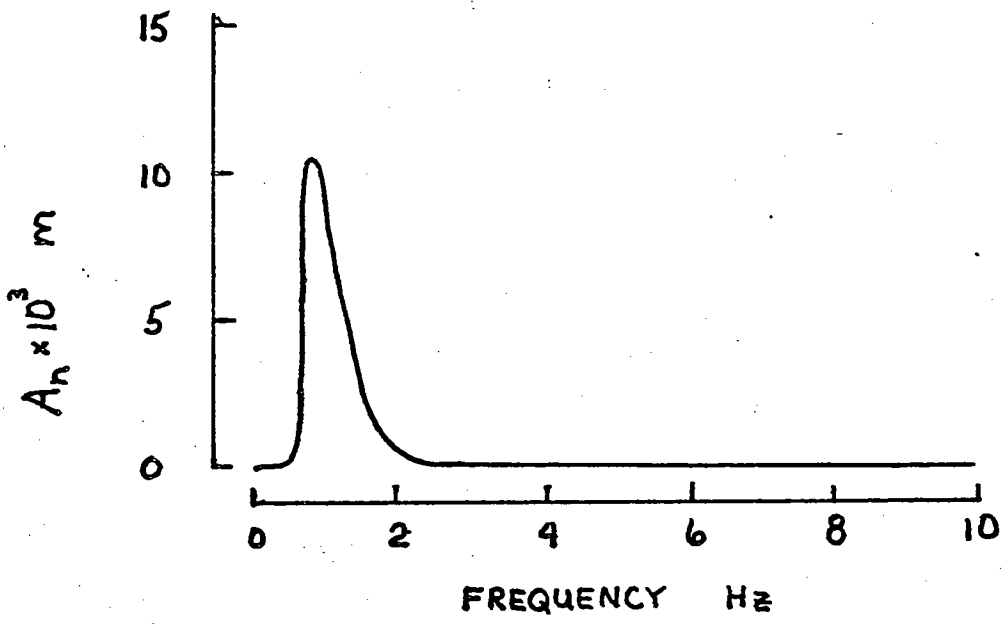
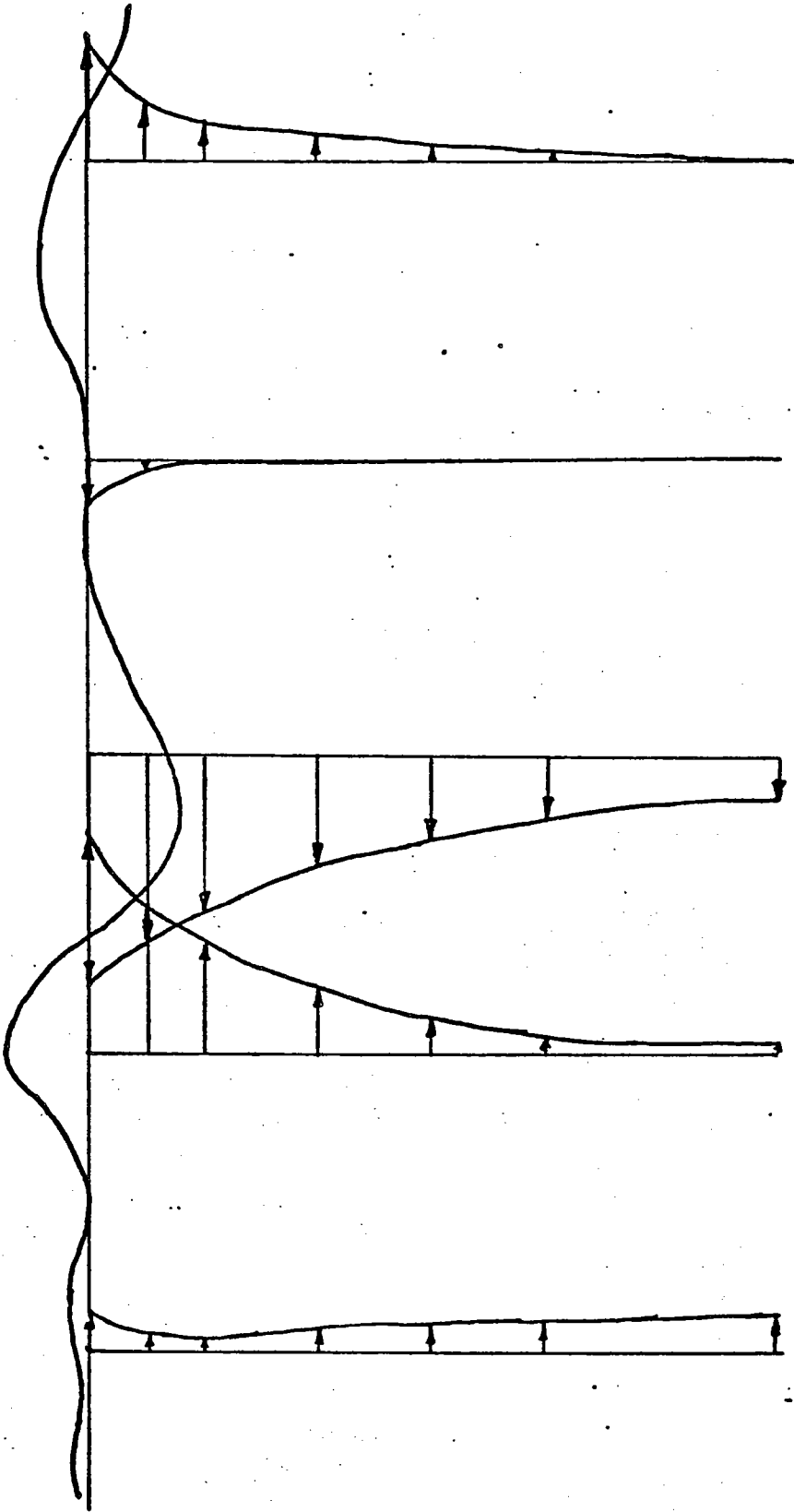Figure 4.3 Typical input spectrum for simulation

Figure 4.4   Simulated time series of velocity profiles under random waves

See Equation (3.10). The spar equation is integrated in time

using a fourth order Hamming predictor-corrector integration

algorithm. Because of the random simulation, it is not possible

to compute subsamples of the time series so that convergence of

this method is forced, rather than the usual single estimate of

a predictor corrector, in order to avoid numerical instability.

Note that at each time step the relative velocity is found at the

spatial sample points and a spatial integral is evaluated to find

the drag moment. The integration in time is begun by assuming

that the spar is at rest. This introduces starting transients

into the response, which are eliminated by restarting the inte-

gration using conditions from a later time, after transients

have decayed, as the initial conditions.

In Figure 4.5, the ratio of the standard deviations of

the angular velocity predicted by the linearization and the

simulation is plotted in order to provide some measure of the

performance of the linearization. The parameter $\frac{\sigma_A}{R}$, where

σ_A is the standard deviation of the wave amplitude, is much

like the Keulegan Carpenter number discussed in Section 3, so

for small $\frac{\sigma_A}{R}$ and small mean flow, we would expect inertial

forces to dominate, and for large values we would expect viscous

forces to dominate.

Each value of $\frac{\sigma_A}{R}$ represents a particular spectral

wind speed, that is to say that the spectral wind speed deter-

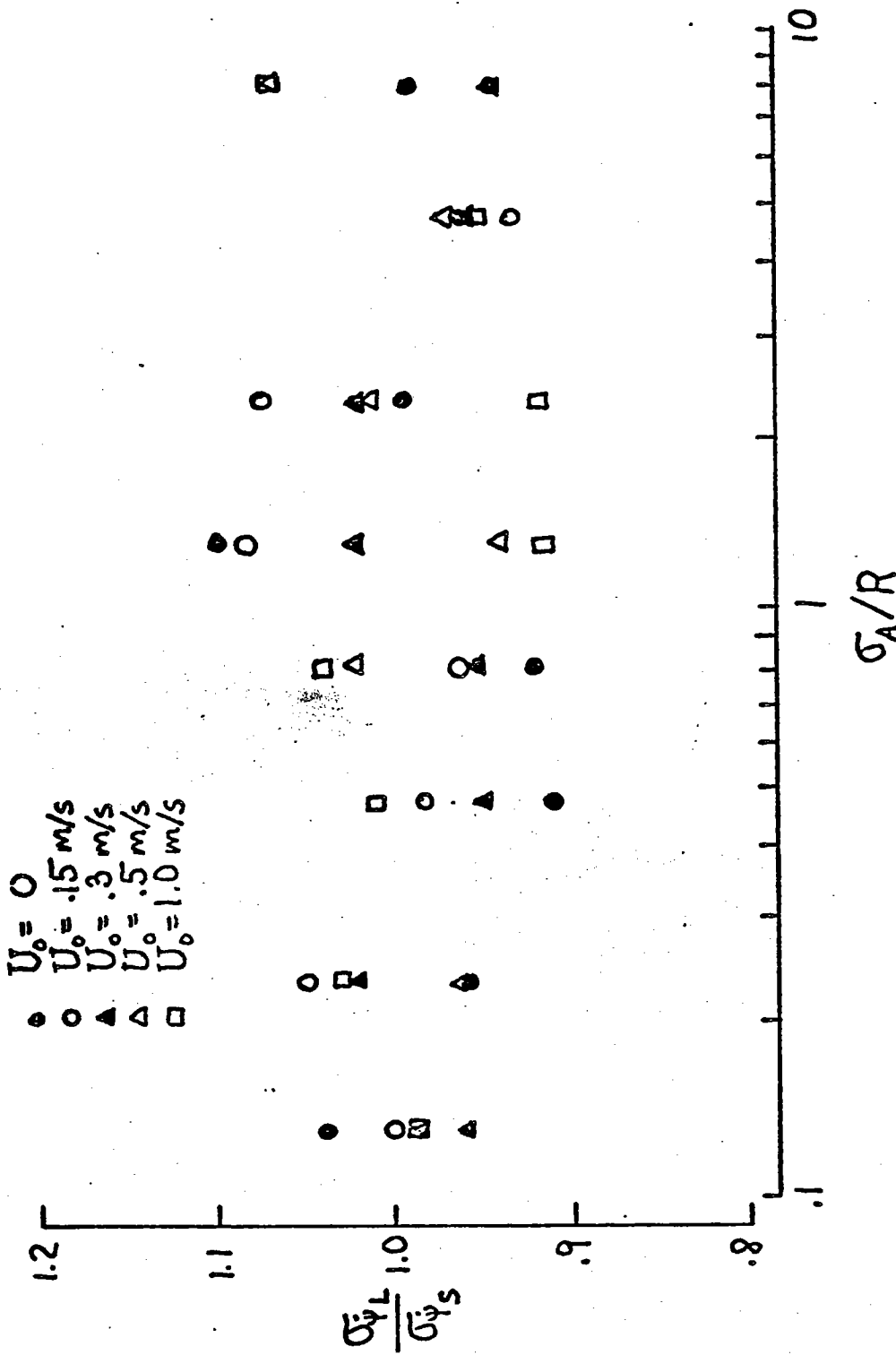mines the variance of the wave amplitude and that the variance

Figure 4.5   Ratios of the root mean square response of the spar from the linearization and simulation.

is independent of the mean current. Thus, each spectrum used

generates a column of data points on the graph.

For comparison with Figure 4.5, the values of the

standard deviations of the angular velocity predicted by the

linearization are plotted in Figure 4.6. The numbers in paren-

theses are the ratios of the wave spectral peak frequencies to

the natural frequency of the spar. Notice that for any particular

input wave spectrum characterized by a column of data points,

this frequency ratio varies, due to the Doppler shift introduced

by the mean flow. We point this out to emphasize that the change

in response, $\sigma_{\dot{\psi}}$, for any given input level, σ_A , is due not.

only to the increased viscous forces caused by a mean flow, but

also to spectral smearing caused by the frequency shift.

The most important thing to notice about Figures 4.5

and 4.6 is that the error in the linearized estimate is within

10% over a substantial range of inputs and responses. The r.m.s.

error, ϵ , of the simulation variances, assuming a bandwidth

B = 1 Hz and a sampling interval T = 100 sec, is about 10%, where

$$\epsilon^2 = \frac{1}{BT}$$

see Bendat and Piersol (1971). Some of the scatter in Figure 4.5

may therefore be random error.

The linearized estimates of the mean inclination,

plotted in Figure 4.7, are not as good as the estimates of r.m.s.,

and differences as large as 30% are observed. Note that the mean

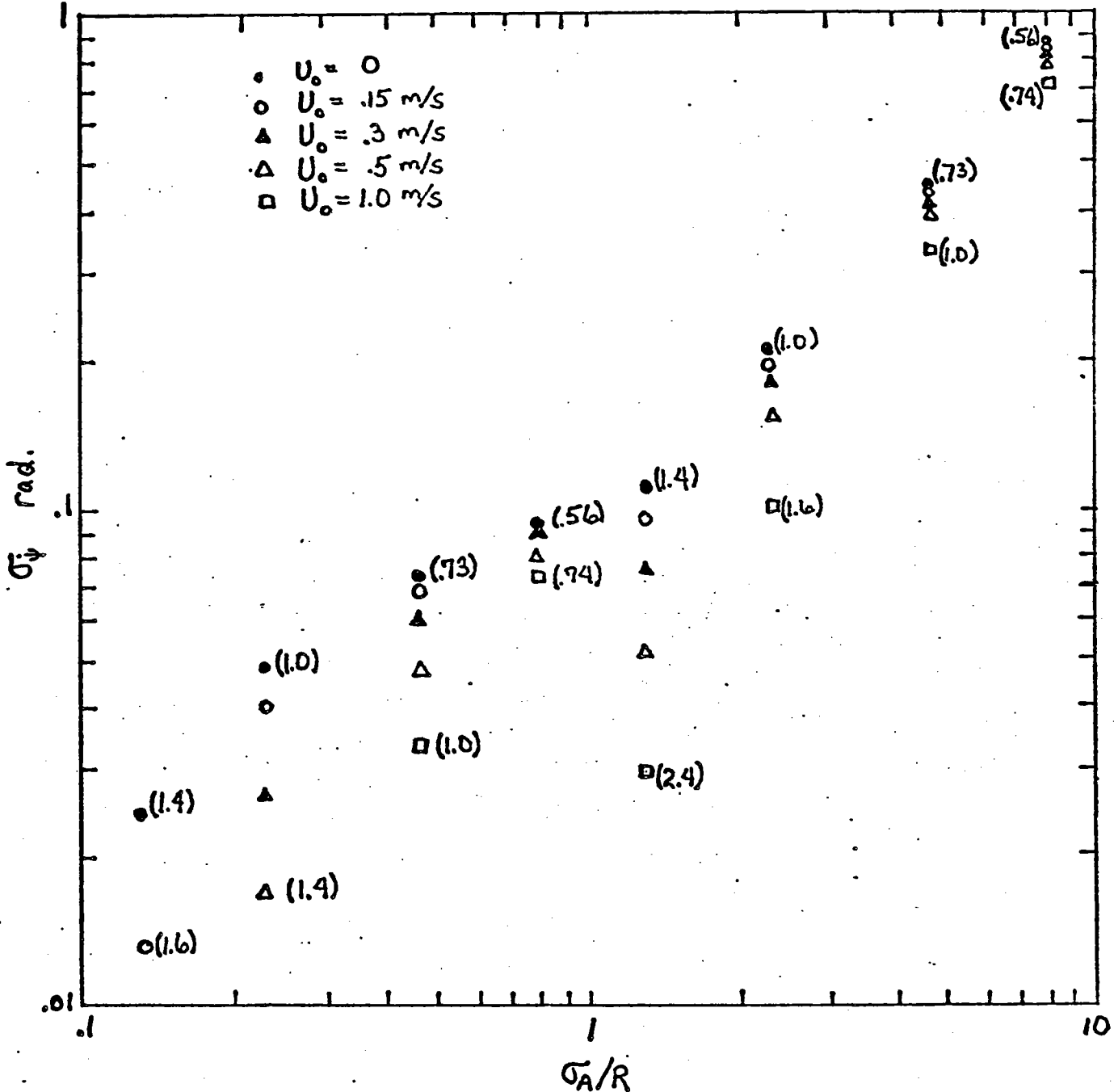angle of inclination is substantially influenced by wave energy,

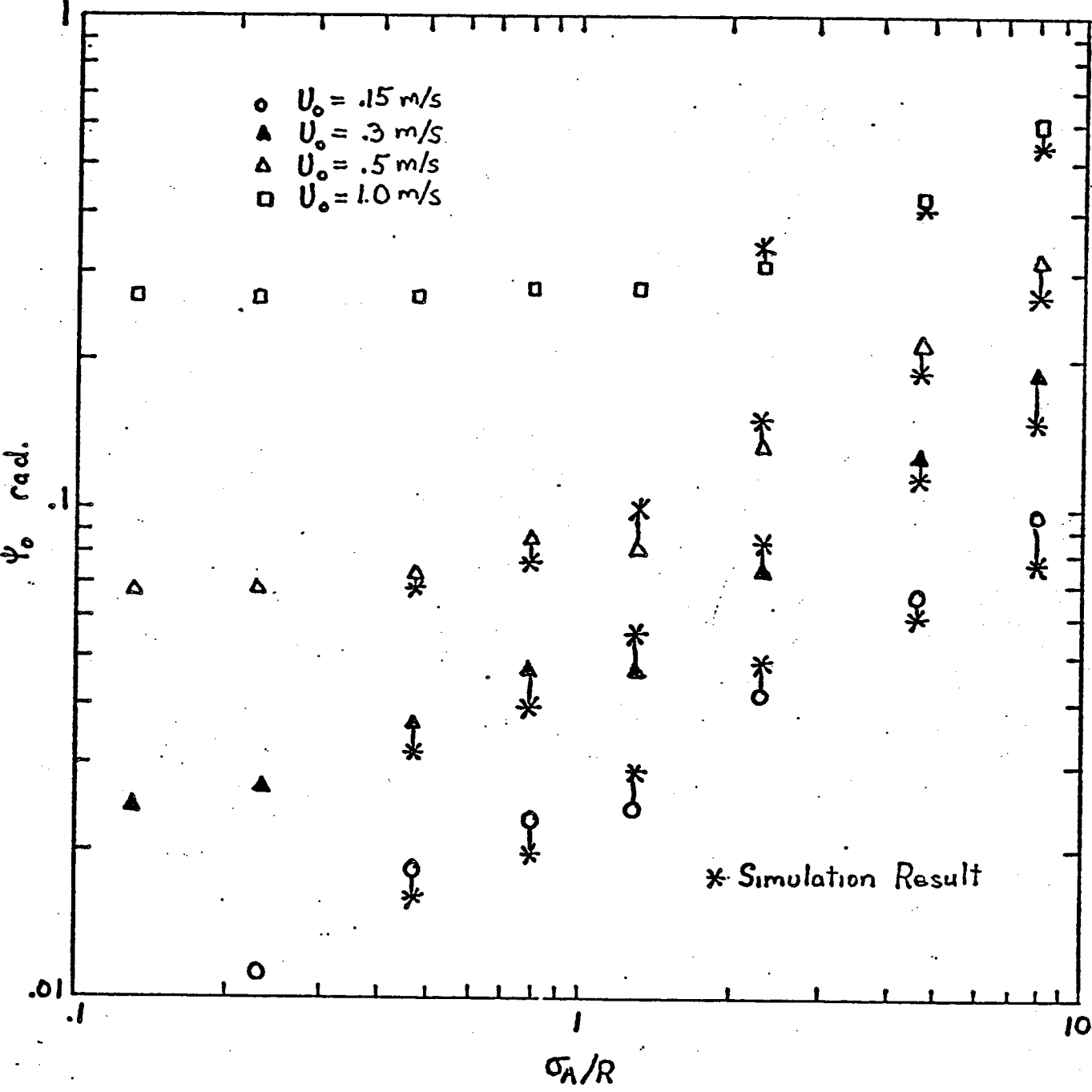Figure 4.6　Root mean square response of the spar from the linearization.

Figure 4.7   Mean inclination predicted by linearization for the numerical experiments.

and that the linearization does reflect this behavior.

It appears that the linearization performs well, so that any large discrepancies with experimental data cannot be attributed to this technique, but rather to the physics of the model.

5. Experiment

The experimental system described here is designed to test the performance of the drag linearization and the vortex shedding model. It is not, in fact, capable of exploring all of the parameter ranges which are of interest. The most significant deficiency is the small maximum amplitude to radius ratio, Keulegen-Carpenter number, which can be achieved. We are, therefore, not able to explore the region of drag dominance which exists in large amplitude oscillations. The small Keulegan-Carpenter number also implies negligible vortex shedding due to wave motion so that the validity of the stationary phase vortex model is not tested. The linearized approximation should perform best in the region of small amplitude waves, $N_{KC} < 10$, where the added mass and drag coefficients are well-behaved (see Figures 3.4 and 3.5). This region, then, seems like a good place to begin exploring the model's performance.

5.1 Spar and Instrumentation

5.1.1 Spar

The experimental spar consists of a right circular cylinder 10 cm in diameter mounted on a large compression spring and anchored with 60 lb of lead, see Figure 5.1. The spar is mounted on a compression spring to elevate the natural frequency of the system into the region of significant wave energy
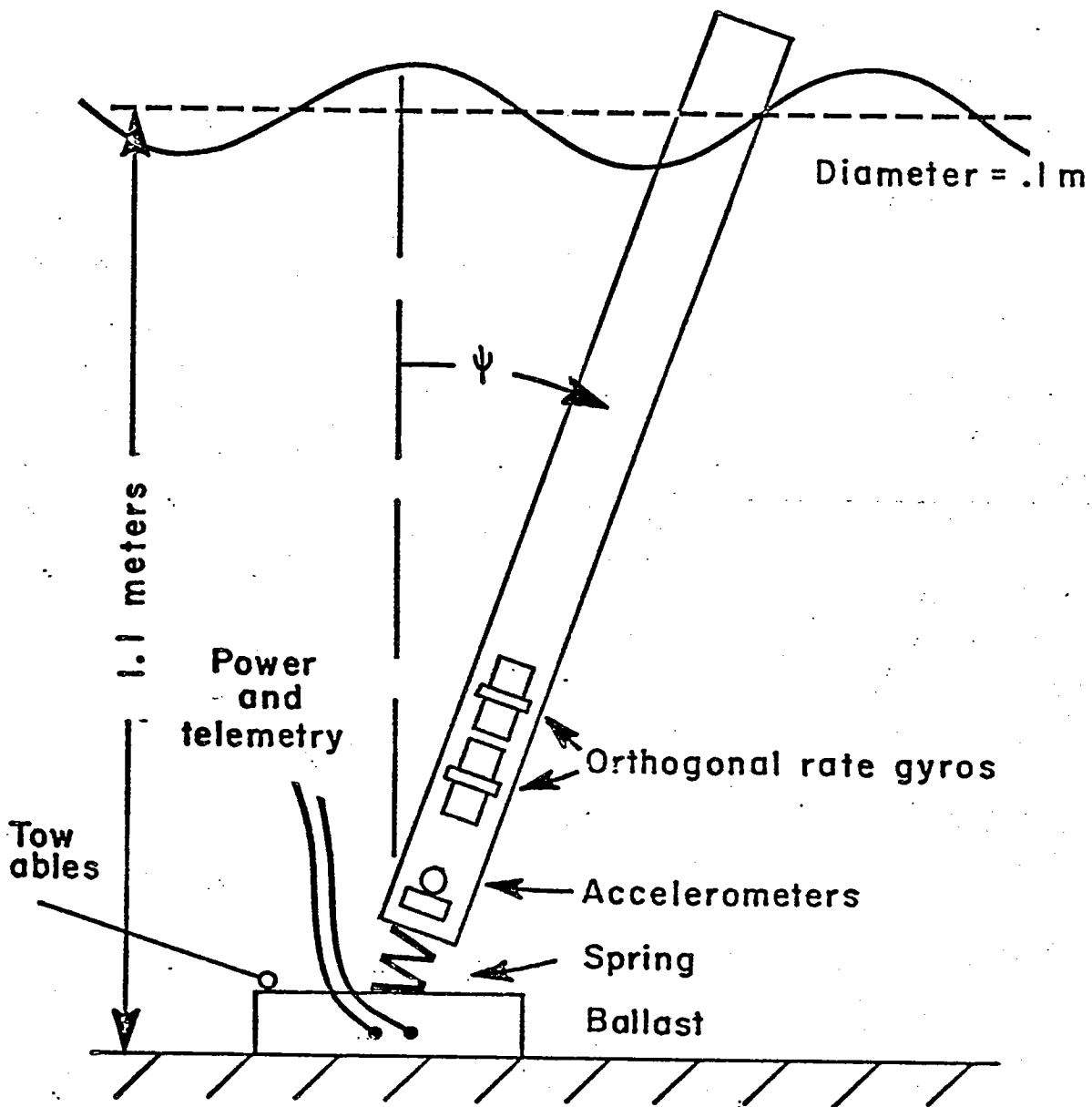
Figure 5.1   Experimental System

of the random wave spectra available at the MIT ship model

towing tank. A compression coil spring which is relatively weak

as a beam and offers roughly the same stiffness in all directions

is ideal for simulating an increased buoyancy. Due to the

asymmetry in the number of effective turns in the spring for

different directions of inclination, there is about a 5% varia-

tion in the bending stiffness which results in a slight coupling

of the in-line and transverse oscillation modes. For the purpose

of estimating the response using the linearization, this coupling

is ignored.

The spring used has a nominal 10 cm outside diameter,

is 15 cm long and is wound from 1 cm diameter wire. The ends are

ground flat and the spring has a nominal compression stiffness of

1.5×10^5 N/m (130 lb/in). The bending stiffness of the assembled

system in air was measured using a spring balance and found to be

$\chi_A \simeq 110$ Nm/rad. This value is used in place of $-Mz_{cg}$ in Equa-

tion (3.9) so that

$$\chi = \int_o^h \rho g \, \pi R^2 z \, dz + \chi_A$$

for this system. The moment of inertia in air is found by measur-

ing the natural frequency of the system in air, that is,

$I = \chi_A/\omega_o^2$. The natural frequency is $f_o = .8$ Hz, which implies

that $I = 4.4$ kg m^2. If we make a calculation of the natural

frequency of the spar in water, we find that the added moment of

inertia is $I_a = 3.5$ kg m^2 assuming $C_a = 1$ and that the buoyant

restoring force adds 45 N-M to the stiffness so that $f_{o_w} = .74$ Hz.

A measurement of this natural frequency in the MIT towing tank

showed f_{o_w} = .75 Hz. The cylinder itself is nominal 4 in. out-

side diameter with 1/8 in. wall extruded aluminum tubing. No

special effort was made to ensure roundness, but some sample

measurements showed it to be within 1% of the nominal outside

diameter. The end caps were machined from aluminum plate and

o-ring seals were used to maintain a water tight seal, see

Figure 5.2 for some detail. The end caps are held in place by

internal tie rods, which are 1/2 in. x 1/2 in. x 1/8 in. aluminum

angles at the bottom of the cylinder and stud stock near the top.

Two rate gyros, two accelerometers and amplifiers are mounted in

the frame formed by the angles. Foam inserts are wedged between

the cylinder and the instruments to damp lateral vibrations of

the internal structure. The first mode natural frequency of the

frame and instruments was near 20 Hz and any motions at resonance

could be filtered from the signal, since frequencies of interest

are in the neighborhood of 1 Hz. Electrical penetrations were

made through the bottom end cap using Amphenol type 165 hermeti-

cally sealed connectors filled with silicon dielectric to ensure

a water tight seal. The male halves of the connectors have an

o-ring seal at the end cap and the female halves are potted to

Belden shielded power supply cable using a urethane casting

compound. The cables run inside the mounting spring and through

the lead anchor. The cylinder, spring, and anchor are held

together with a short chain made of s-hooks and two eye bolts,

Figure 5.2   Detail of the spar.

see Figure 5.2. The center of rotation is assumed to be at the lower eye, even though the spar is no longer "rigid". The spring is precompressed, by tightening the eye bolt in the anchor, so that the end cap does not lift away from the spring at large angles of inclination.

5.1.2 Rate Gyros

The instrumentation in the spar includes two orthogonal rate gyros. The rate gyros are surplus Minneapolis Honeywell JRH 20 Rate Measuring Gyros. A three-phase, 400 Hz power supply was built to drive the gyro motors. The same 400 Hz signal is used to excite the variable reluctance pickoff, which measures the gyro gimbal deflection. The output from the pickoff is an amplitude modulated 400 Hz signal which is demodulated by analog multiplication with the input signal. A low pass filter at 40 Hz removes the unwanted high-frequency signal, so that the output is a voltage proportional to the angular velocity of the spar. Linearity of the system should be within 1%, limited mainly by the performance of the analog multiplier. The claimed resolution of the rate gyros is .01 degree/sec, but various sources of noise degraded this to about .1 degree/sec. Note that this corresponds to an oscillation at the natural frequency of the spar of .02 degree amplitude. The natural frequency of the gyros is between 30 Hz and 100 Hz with about 40% of critical damping, and posed no problems for this experiment.

The calibration of the rate gyros was performed by exciting the spar at a frequency near 1.5 Hz at a known amplitude. This was done by attaching an aluminum channel to a bracket on the top of the spar and to an eccentric on a rotating circular plate. The signal from the gyros is fed into a Hewlett Packard Fourier Analyzer and the frequency and amplitude of the signal are determined.

Assuming a 2% error in each of the length measurements and a 2% error in the determination of the oscillation frequency, the gyro calibration should be correct to within 6%.

5.1.3 Accelerometers

Two Sundstrand Kistler Model 303 force balance accelerometers were mounted with their sense axes parallel to the rate gyro sense axes. In this orientation they act as inclinometers, measuring gravity times the sine of the angle of inclination, with an error due to horizontal accelerations. They were included for measuring the mean angle of inclination as well as an alternate source of response data. Unfortunately, a small amount of vibration of the internal mounting structure excited by the rate gyros created noise with an amplitude equivalent to about 6 degrees of inclination at a frequency near 20 Hz. This was easily filtered for purposes of data analysis but introduced extra recorder noise because a lower gain was used.

The accelerometers are calibrated by placing them

vertically on a level surface and measuring the output corre-
sponding to 1 g. They are then inverted and the output corre-
sponds to -1 g. Half the sum of these two measurements is then
used as the zero measurement. Linearity of the accelerometers
is claimed to be better than .1% of full scale, which corre-
sponds to an accuracy of the zero within .1 degree.

5.2 Experimental Configuration and Data Handling

5.2.1 Towing Tank

The experiments on the spar were carried out in the
MIT Ocean Engineering Ship Model Towing Tank. The towing tank
is equipped with a steel belt driven overhead carriage, which
runs at a number of fixed speeds. The tank is approximately
2.5 meters wide, 33 meters long and 1.1 meters deep. There is a
flat plate hydraulically driven wave maker at one end which can
be driven by a sine wave generator or a simulated Pierson-
Moskowitz wave form recorded on 7 track FM tape. A beach made
of stainless steel lathe turnings acts as a wave absorber at the
opposite end. Large windows near the middle of the tank make it
possible to view a section of the tank below the water line.

5.2.2 Wave Gauges

Two bridge balanced, parallel wire, resistance wave
gauges measured the wave height during the experiments. One was

fixed to the side of the tow tank and the other was mounted on the towing carriage. They are calibrated by recording the output for various depths of immersion. There appeared to be about a 5% nonlinearity in their response over 10 cm, and a slight zero drift. The zero drift was eliminated in the data analysis and the nonlinearity was ignored. The accuracy of the calibration is on the order of 2% since the wave gauge mounts were equipped with dowels which mated with pairs of machined holes in a fixed mounting plate.

5.2.3 The Experiment

A current was simulated by towing the spar over the bottom of the wave tank using the towing carriage. Two views of the towing configuration are shown in Figure 5.3. An outrigger made of steel angle was bolted to the lead anchor and plexiglas skids were attached to the ends to carry transverse moments. Four cables made of stainless aircraft control cable were attached, as shown in Figure 5.3, to an aluminum channel which was bolted to the towing carriage. A limitation on the towing speed is introduced by the stability of the anchor. For speeds higher than about .3 m/s, the drag force and lift from the tow cables became large enough to raise the leading edge of the lead weight from the bottom. This also occurred during some of the large waves in the simulated random seas.

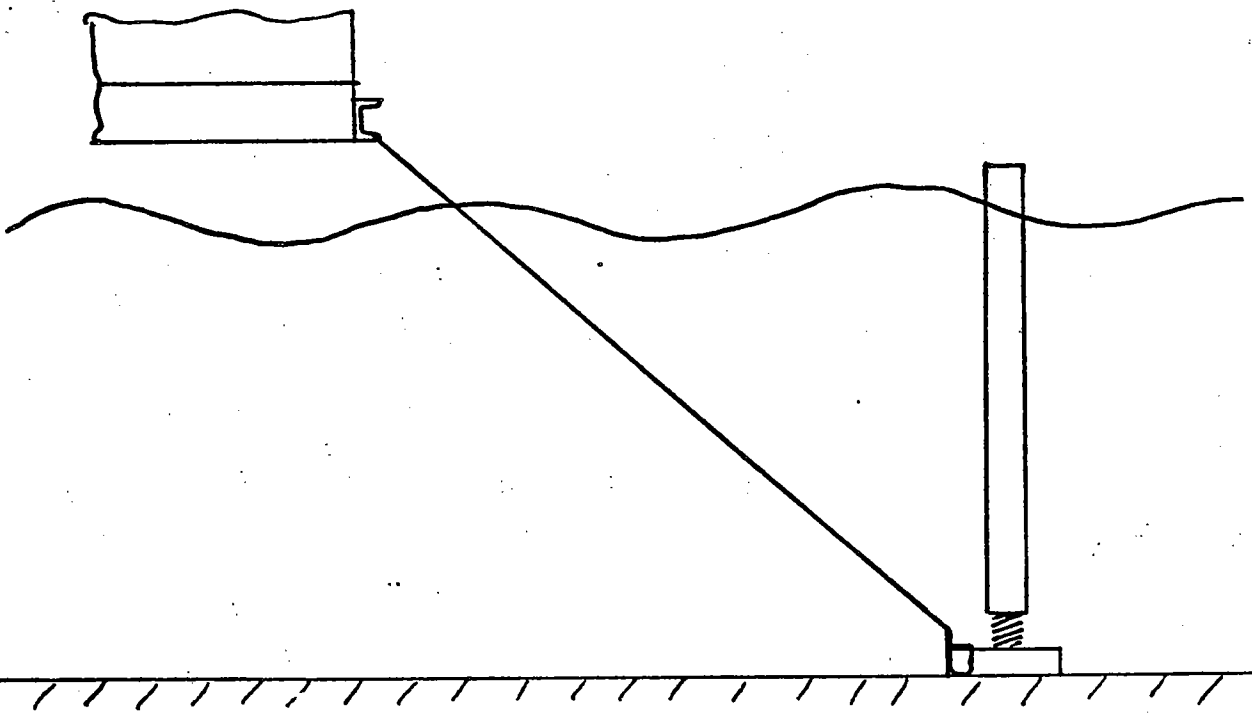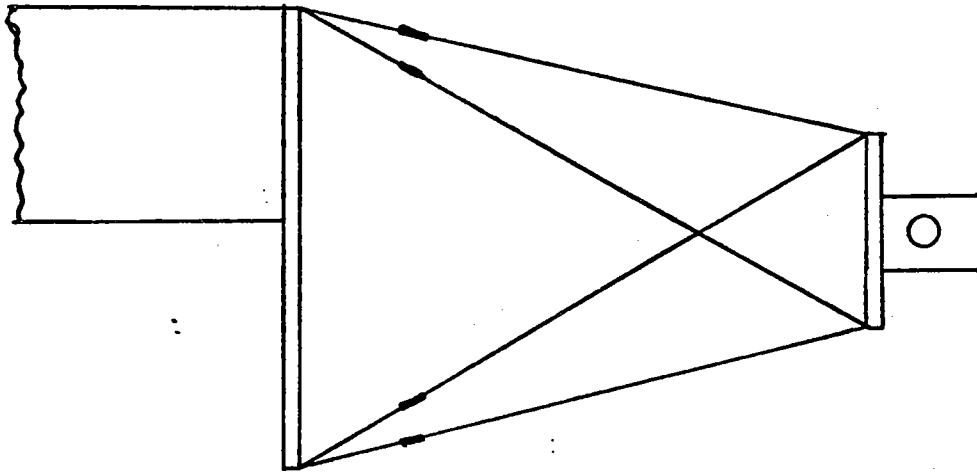The orientation of the instruments with respect to the

Figure 5.3   Towing configuration of the spar.

tank was determined by inclining the spar in the direction of tow and recording the components of the angle of inclination measured by the accelerometers. A coordinate rotation of .19 radians is necessary to separate the in-line from the transverse motions. An error of 2 or 3 degrees in this measurement would cause less than .2% crosstalk in the computed spectra, which was far less than the coupling introduced by the spring.

The data from the four on-board instruments and the two wave staffs is recorded in analog form on 6 FM tracks of Sangamo 14 track tape recorder. The same machine is then used to play back the data into a Hewlett Packard 2100 mini-computer equipped with a 16 channel 12 bit digitizer. The signals pass through active low pass filters with second order poles at 20 Hz and are then digitized in parallel at a frequency of 80 Hz. The digitization actually occurs serially with a 20 sec lag between channels at each sample point. The small phase shift introduced is ignored during processing. Each digitized run is then recorded on 9-track digital magnetic tape, so that it can be accessed for later processing. Processing was done on the same machine which is equipped with an HP 5451 Fourier Analyzer System. This system has a CRT display of blocks of machine core, permitting visual interaction during processing. It is programmable in a similar fashion to hand-held calculators, allowing quick development of processing schemes.

5.3 Experimental Results

The experiment consisted of towing the spar through simulated Pierson-Moskowitz fully developed seas. The wave spectra are generated by filtering the signal of a white noise generator. The P-M seas used in the experiment corresponded to wind speeds of 10, 17.5, and 25 m/s. In addition, towing speeds of .15 and .3 m/s were used to simulate the combined wave and current field. For the experiment, some values of the surface wave Reynolds Number, N_{Re_W}, the surface wave Keulegan Carpenter Number, N_{KC}, the fixed cylinder shedding frequency, f_v, and the steady flow Reynolds Number, N_{Re}, where

$$N_{Re_W} = \sqrt{2}\, \sigma_{A\omega} D/\nu$$
$$N_{KC} = \sqrt{2}\, \sigma_A \pi/r$$
$$f_v = N_s U_o/D$$
$$N_{Re} = U_o D/\nu$$

respectively, are given in Tables 5.1 and 5.2. Note that the maximum N_{KC} is 4.4 so that we would not expect much vortex shedding due to waves. In fact, in the 25 m/s P-M waves, one could occasionally see a vortex shed as a large wave passed.

Approximately 10 minutes of data for each of the combinations of wave spectra and towing speeds was recorded, including tows in calm water. This provided enough data for averaging ten spectra with a resolution of .018 Hz. The experimental spectra in the following figures were generated in this

TABLE 5.1

WIND SPEED	σ_{AW}	σ_A	N_{Re_W}	N_{KC}
10	9.3 cm/s	.8 cm	13,000	.7
17.5	16.4 cm/s	2.4 cm	23,000	2.1
25	23.4 cm/s	5.0 cm	33,000	4.4

TABLE 5.2

TOW SPEED	N_{Re}	f_v (N_S = .16)
.15	16,000	.24 Hz
.3	32,000	.48 Hz

fashion using a rectangular window. Since the character of the vortex shedding is a dominant feature governed by the towing speed for these cases, the results are grouped according to towing speed.
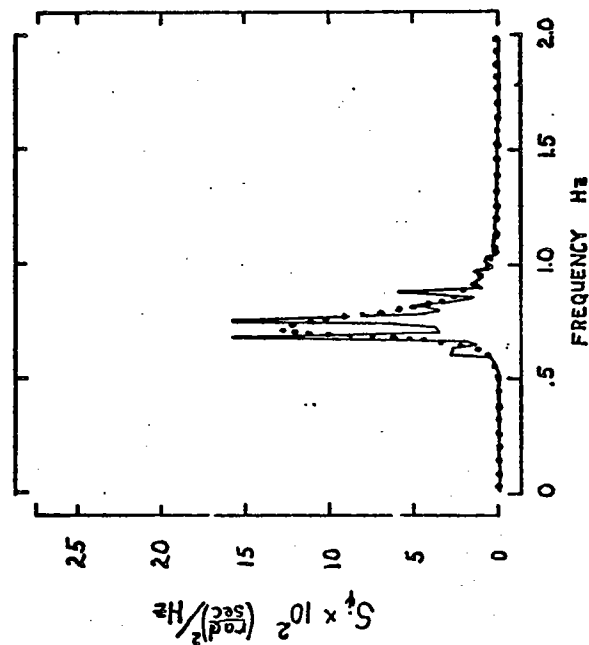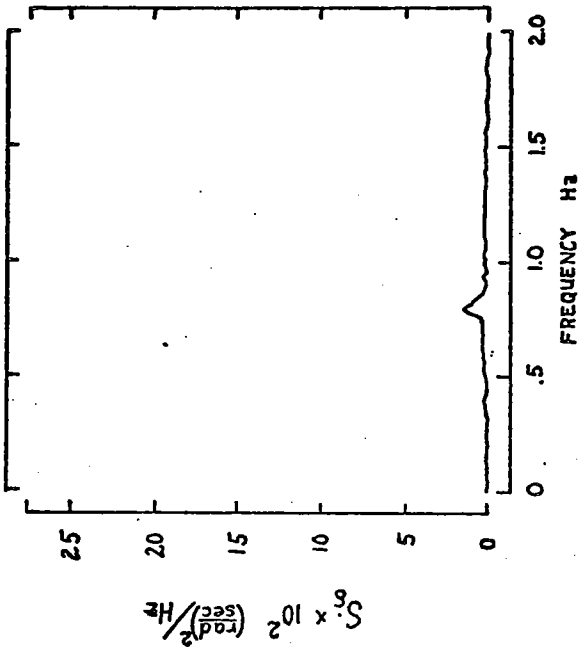
5.3.1 Zero Current

Figures 5.4 a, b, c present the angular velocity spectra, $S_{\dot{\phi}}$ and $S_{\dot{\delta}}$, as well as the wave spectra, S_A, from the zero current experiments and the linearized approximations to the response spectra. It is clear from Figure 5.4 a that there is good agreement between experiment and linearized response for the 10 m/s wave spectrum. This is expected since the wave energy is above the spar natural frequency, so that drag damping is unimportant. As shown in Figure 5.4 b and c, the estimates for 17.5 m/s and 25 m/s are somewhat high. This is due primarily to the nature of the simulated spectrum, which appears to have discreet bands at approximately .05 Hz frequency spacing. By looking at the input wave spectra and the response spectra for these two cases, one can see a "hole" in the response close to the natural frequency which is due to low energy in the input spectrum. This would cause an overestimate of response found using the smooth input spectrum with the same mean square as shown, because of the amplification which occurs near the natural frequency. We note that the energy in the $\dot{\delta}$ spectrum is due to the coupling
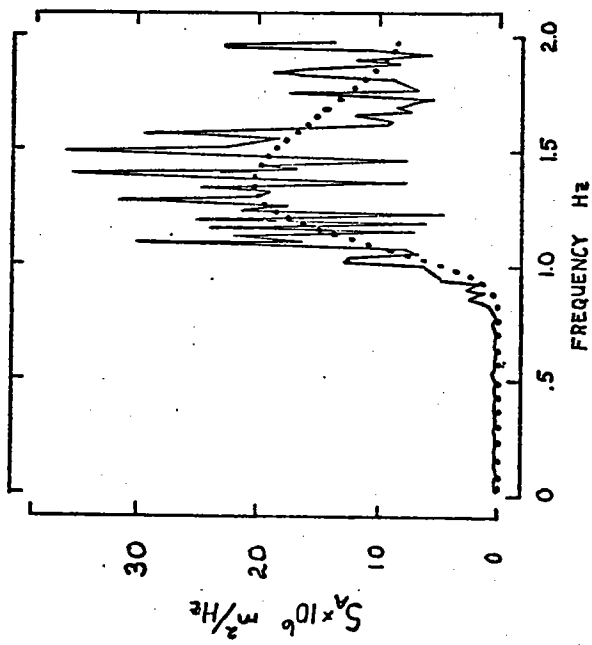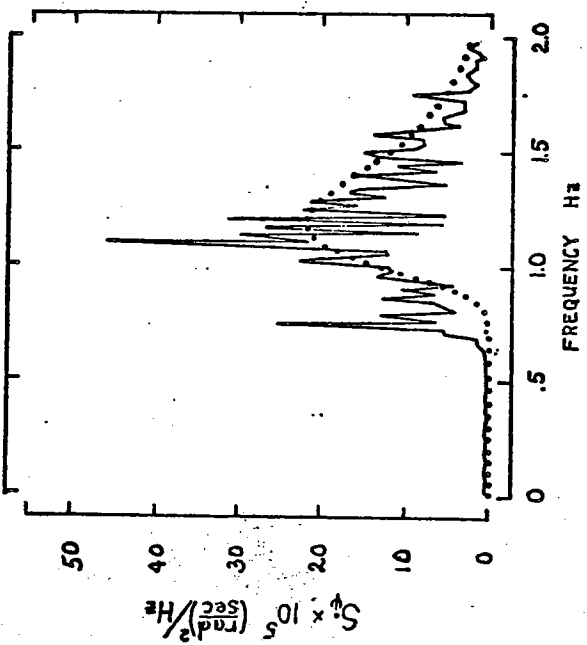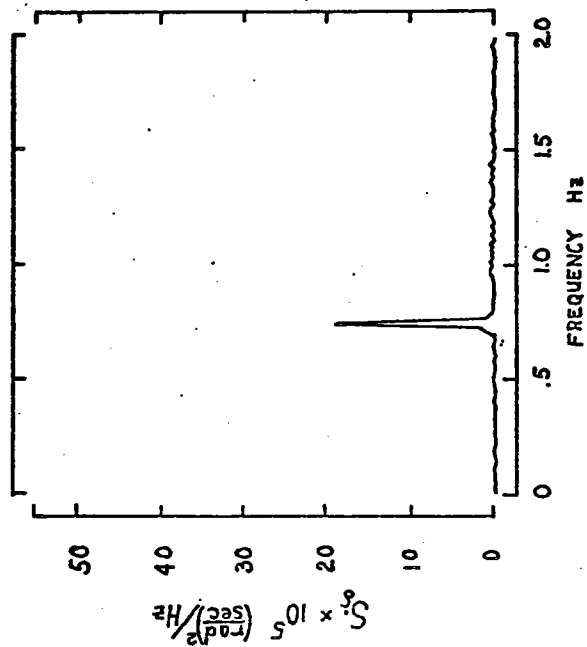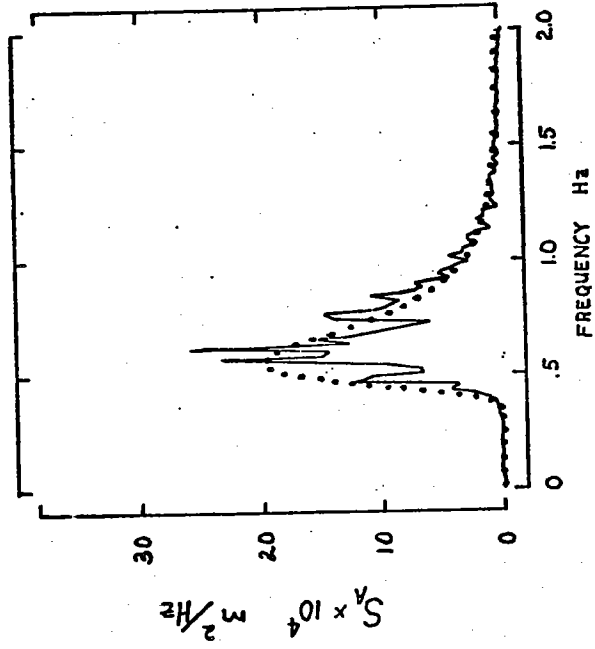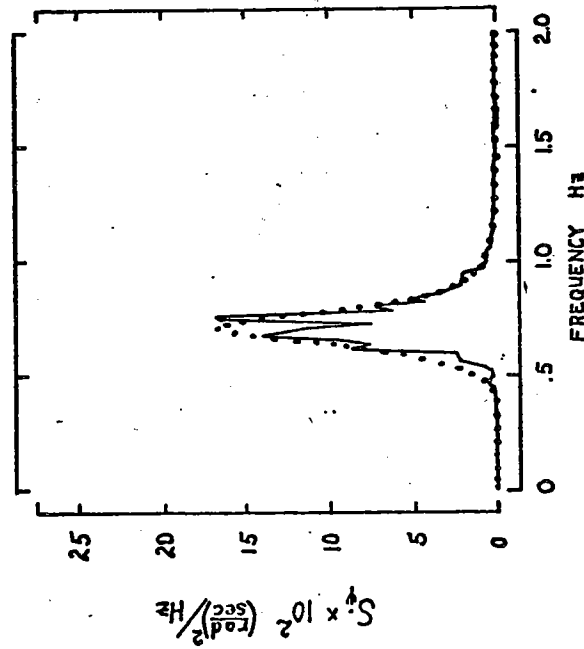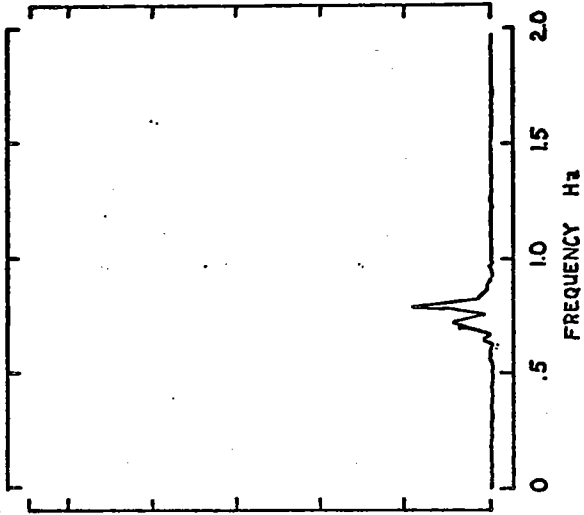
	Lin···	Exp—
σ_A^2	3.4×10^{-5}	3.4×10^{-5}
σ_ψ^2	2.6×10^{-6}	2.6×10^{-6}
σ_δ^2	0	1.6×10^{-7}

Figure 5.4 a   Spar response $U_0 = 0$, $V = 10 \, m/s$
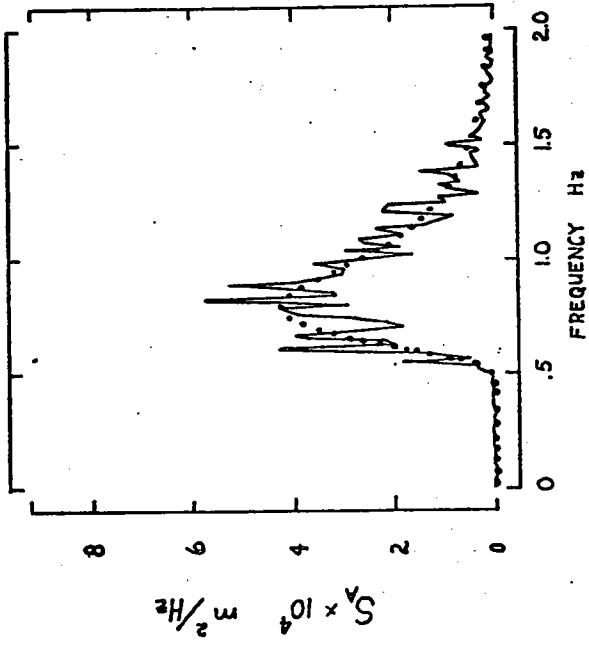
	LIN···	Exp—
σ_A^2	4.4×10^{-4}	4.2×10^{-4}
σ_ψ^2	.033	.036
σ_δ^2	0	7.6×10^{-3}

Figure 5.4 b   Spar response $U_b = 0$, $V = 17.5$ m/s

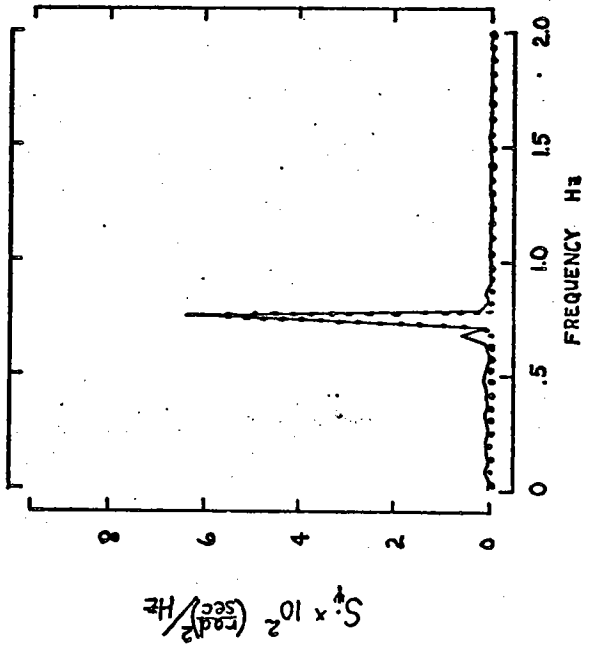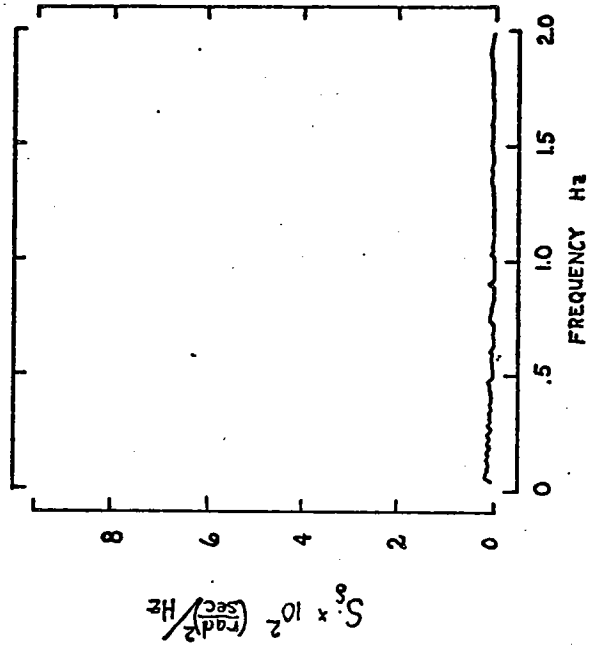|	Lin...	Exp—
σ_A^2	1.2×10^{-3}	1.2×10^{-3}
$\sigma_{\dot{\psi}}^2$	.069	.058
$\sigma_{\delta_0}^2$	0	7.6×10^{-3}

Figure 5.4 c   Spar response $U_b = 0$, $V = 25$ m/s

introduced by the spring, mentioned earlier.

5.3.2 .15 m/s Towing Speed

The vortex shedding frequency for a fixed cylinder in .15 m/s flow assuming N_S = .2 is .32 Hz, and the in-line force frequency would be .64 Hz so that we might expect alternate shedding in-line lock-in for a cylinder with a natural frequency near .75 Hz. This does not occur. However, it appears that the actual Strouhal number for the cylinder is about .16, since the cylinder experiences three dimensional effects at the free sur-face. Gouda (1975) has shown that cylinders with $\frac{L}{D}$ = 15 may have a shedding frequency reduced by as much as 35%, implying a correspondingly lower Strouhal number. Thus, in this case, where $\frac{L}{D}$ = 10, using N_S = .16, twice the shedding frequency is at .5 Hz and 4 times the shedding frequency is at 1 Hz. From Figure 3.2 we see that this places the system in the center of the paired shedding in-line, lock-in region.

The cylinder does in fact experience paired shedding at this towing speed, and the response can be seen clearly in Figures 5.5 a, b. The formation of the vortex pairs could be plainly viewed during the tows, since vortex dimples appeared on the surface. Each time the cylinder moved forward through the flow, a pair of vortices was shed. It appears that the acceleration of the spar "cleans" the wake, and therefore permits

	Lin···	Exp—
σ_A^2	0	0
σ_ψ^2	2.1×10^{-3}	2.7×10^{-3}
σ_δ^2	0	1.6×10^{-4}

Figure 5.5 a   Spar response $U_o = .15 \, m/s, \, V = 0$
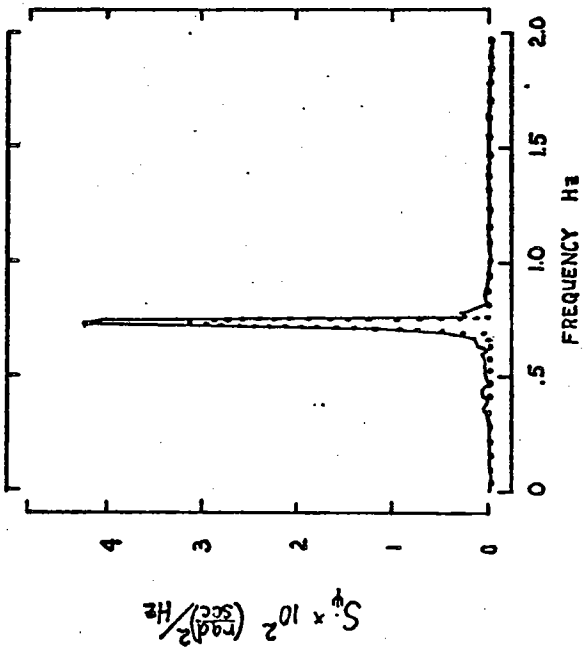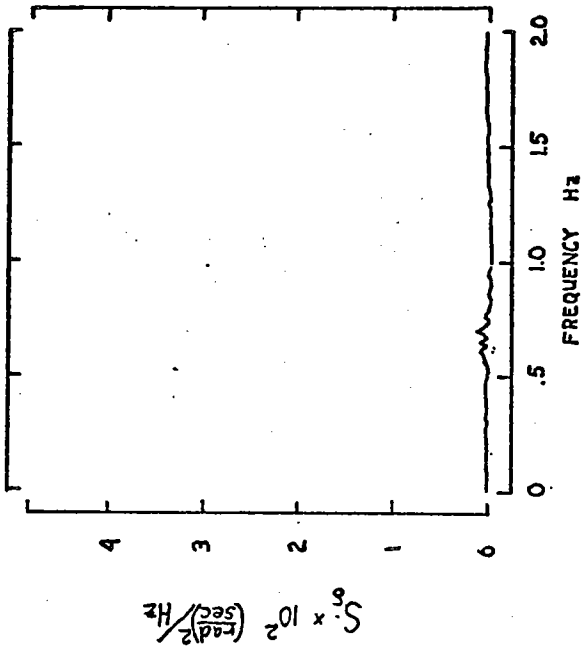
	LIN···	EXP—
σ^2_A	3.4×10^{-5}	3.3×10^{-5}
$\sigma^2_{\dot\psi}$	2.2×10^{-3}	2.8×10^{-3}
σ^2_δ	0	1.7×10^{-4}
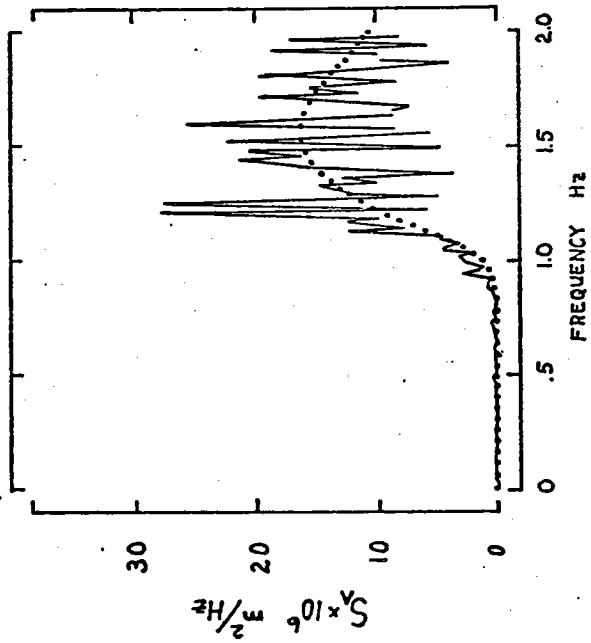
Figure 5.5 b   Spar response $U_0 = .15\,m/s$, $V = 10\,m/s$
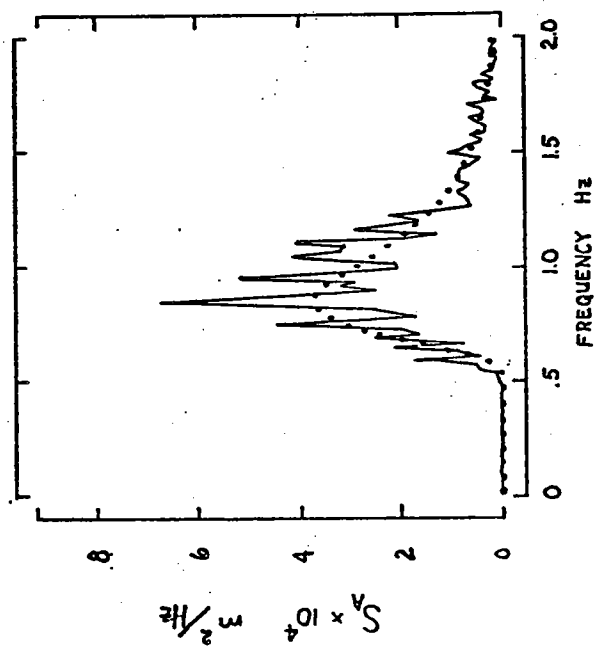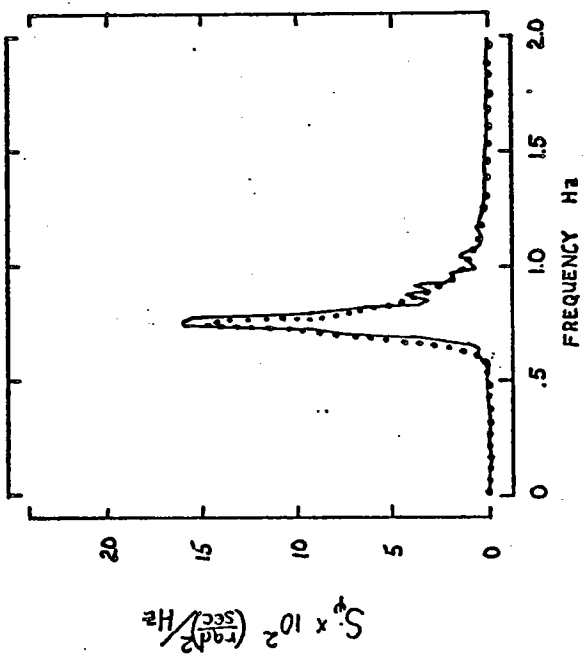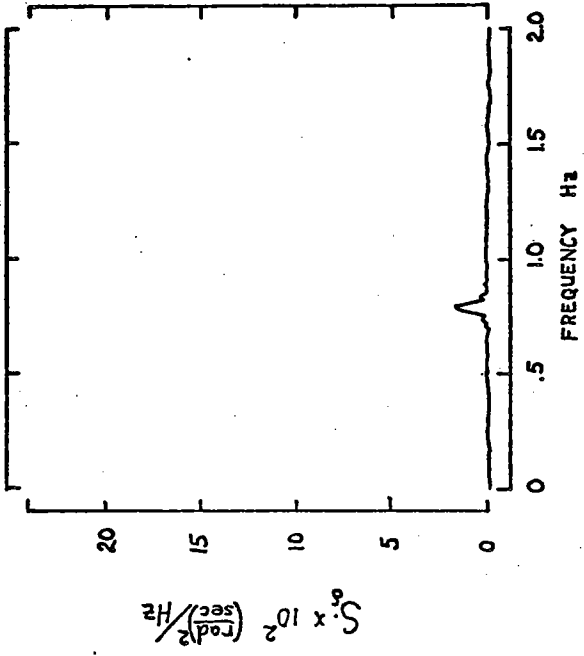
	LIR···	Exp—
σ_A^2	4.3×10^{-4}	4.3×10^{-4}
σ_ψ^2	.025	.026
σ_δ^2	0	1.6×10^{-3}

Figure 5.5 c   Spar response $U_o = .15 \, m/s, \ V = 17.5 \, m/s$

-111-
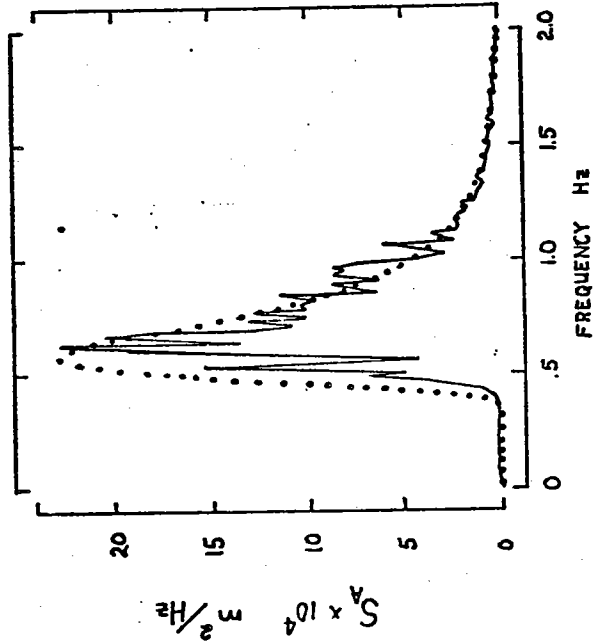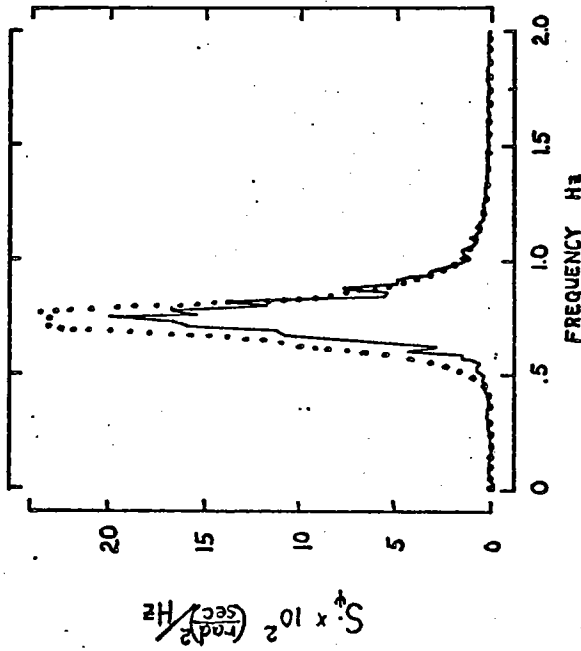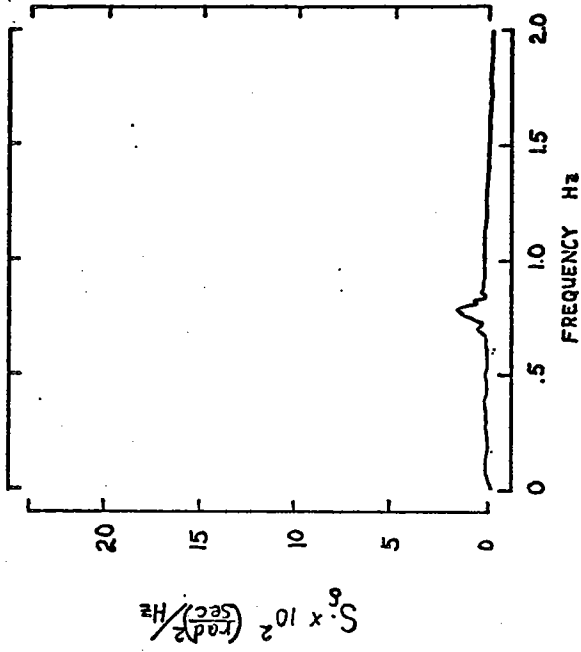
	LIN···	EXP—
σ_A^2	1.2×10^{-3}	1.1×10^{-3}
σ_ψ^2	.061	.045
σ_δ^2	0	5.5×10^{-3}

Figure 5.5 d   Spar response $U_0 = .15\ m/s,\ V = 25\ m/s$

nearly symmetric formation of another pair of vortices. This process reminds one of the formation of a pair of vortices behind a cylinder started from rest, which then shed and are followed by alternate vortex formation. It seems that the in-line accelerations of the cylinder are causing the vortices to be shed cleanly, so that wake formation begins anew, maintaining symmetry in the wake.

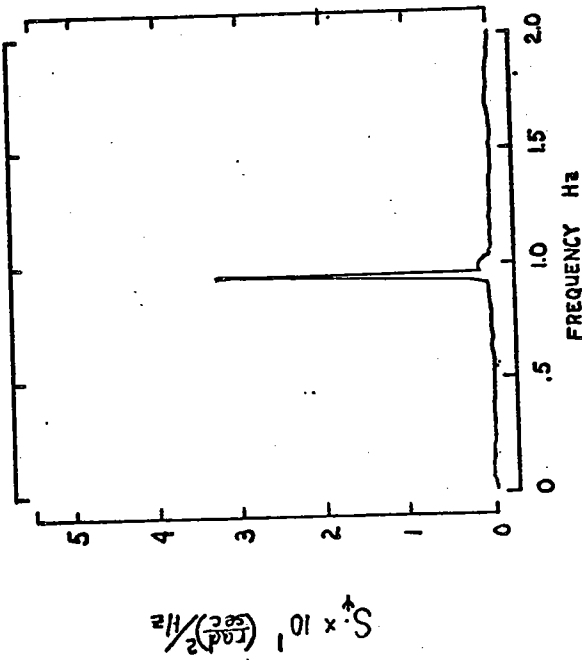There are two important differences between the model proposed in Section 3 for vortex shedding and the one used to generate the linearized responses of Figures 5.5 a, b, c, d. The first is the obvious discrepancy in shedding frequency, the vortices are shed exactly at the spar natural frequency, which would correspond to four times the alternate shedding frequency only if the Strouhal number was .13. We see, therefore, that the wake has been "captured" by the spar motions, similar to a forced cylinder. This is a well-documented phenomenon for alternate shedding, and is not completely unexpected. The linearized predictions of Figure 5.5 use N_S = .13, that is to say that we must predict wake capture, since the model is not sensitive to this phenomenon. It is also necessary to change the in-line drag coefficient. The value of C_D = .06 proposed earlier led to responses an order of magnitude too low. The linearized responses in Figures 5.5 employ C_D = .5, and produce reasonably good results. This result is not exceptional either, considering

the wide scatter in the available data. In fact, King (1977)
recommends a value of C_D = .2 as a safe design value. It appears,
however, that some extensive and consistent experiments would be
of much use.

Notice that the vortex models used in Figures 5.5 and
5.6 assume impulsive power spectra, i.e., sinusoidal forcing, at
the shedding frequency produced by steady flow since the wave
frequencies are higher than the shedding frequency and the sta-
tionary phase estimation is not valid, as mentioned in Section 3.

5.3.3   .3 m/s Towing Speed

The response of the spar when towed at .3 m/s was
dominated by alternate vortex shedding, see Figure 5.6 a, b,
c, d. The main effect of the waves was to slightly decrease the
response in the lateral direction. The linearized model predicts
this due to increased drag, but decreased longitudinal correlation
of the vortices may also be important. The actual transverse
motions of the spar were observed to be somewhat squared. The
effects of this can be seen in Figure 5.6 a in the δ spectrum
where there is a small peak around 1.5 Hz corresponding to the
second Fourier series component of a square wave. The in-line
motions are at exactly twice the frequency of the horizontal
motions, so that the motion of the spar at the surface follows
a "U"-shaped path in the coordinate system moving with the spar.
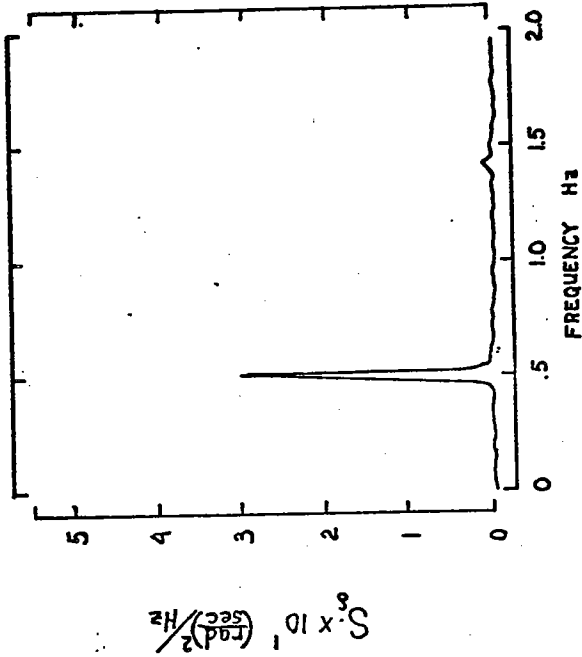
	LIN···	Exp—	LIN*** $C_a=0$
σ_A^2	0	0	0
σ_ψ^2	3.0×10^{-3}	9.6×10^{-3}	9.9×10^{-3}
σ_δ^2	.003	.014	.012

Figure 5.6 a   Spar response $U_o = .3$ m/s, $\bar{V} = 0$

$U_o = .3 m/s$, $V = 10 m/s$

	LIN···	Exp—	LIN $C_a=0$ ***
σ_A^2	3.1×10^{-5}	3.1×10^{-5}	3.1×10^{-5}
σ_ψ^2	.0034	.0092	.010
σ_δ^2	.007	.013	.012

$S_\delta \times 10^1$ $\frac{(rad/sec)^2}{Hz}$

$S_\psi \times 10^1$ $\frac{(rad/sec)^2}{Hz}$

$S_A \times 10^6$ m^2/Hz
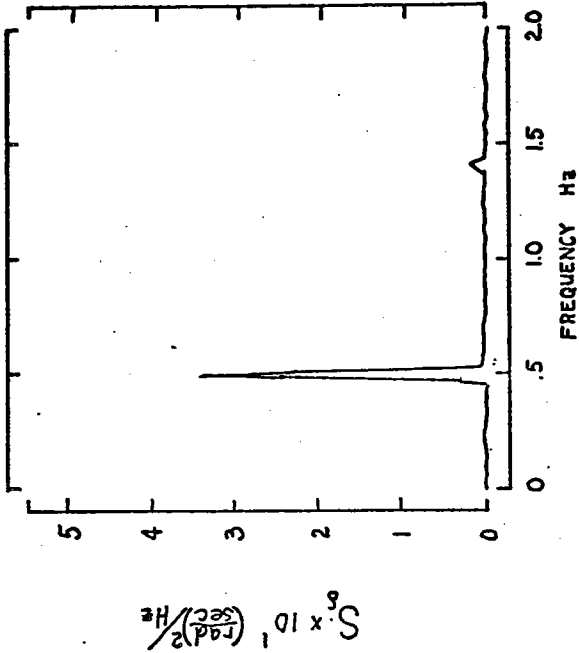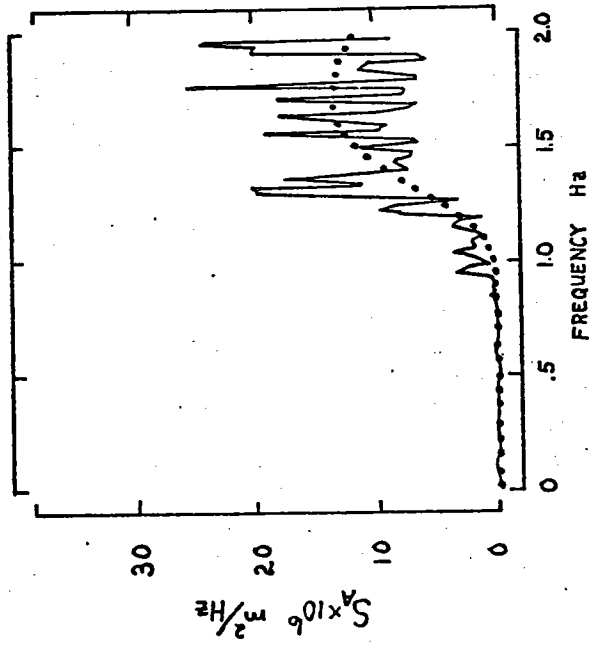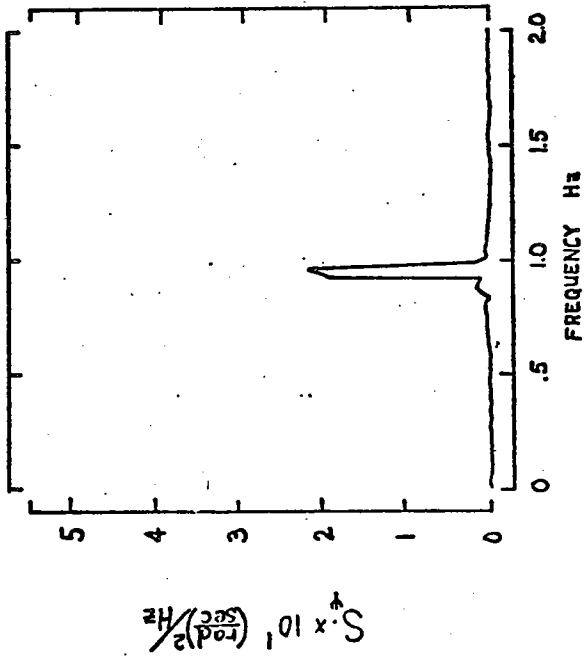
Figure 5.6 b   Spar response
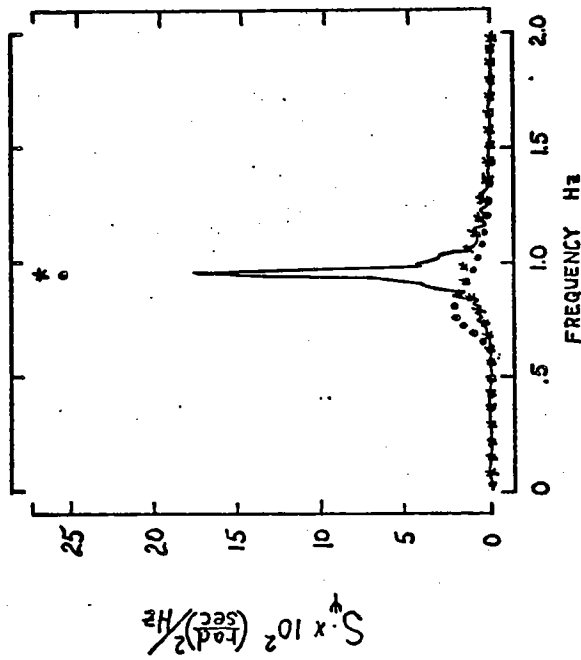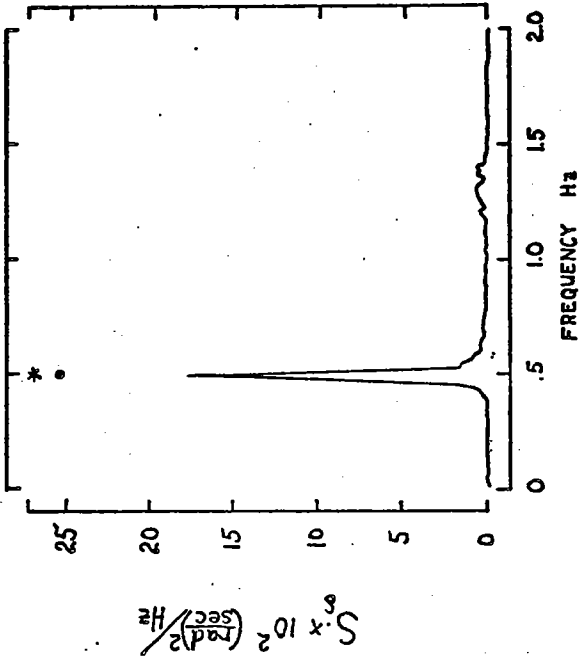
	LIN···	EXP—	LIN***, $C_a=0$
σ_A^2	4.3×10^{-4}	4.3×10^{-4}	4.3×10^{-4}
σ_ψ^2	.0134	.0154	.0169
σ_δ^2	.007	.011	.012
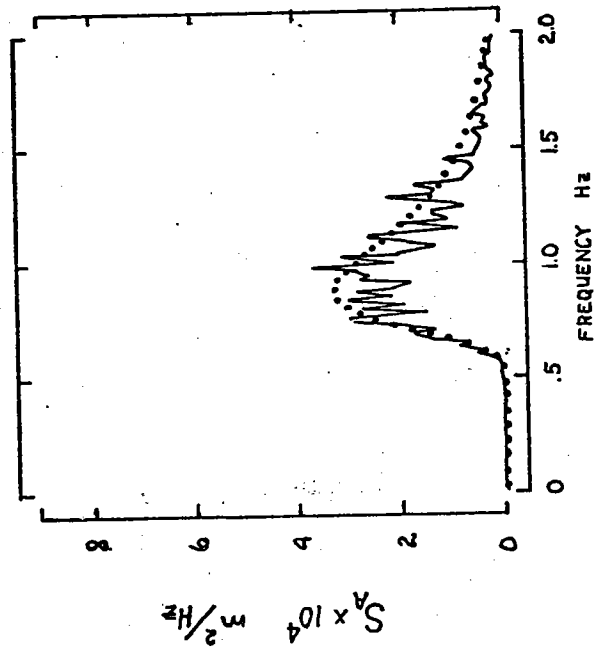
Figure 5.6 c   Spar response $\bar{U}_0 = .3\,m/s$, $V = 17.5\,m/s$
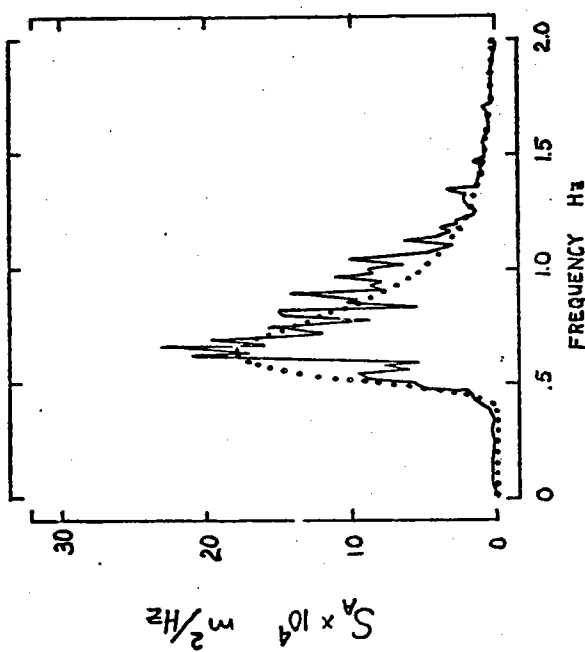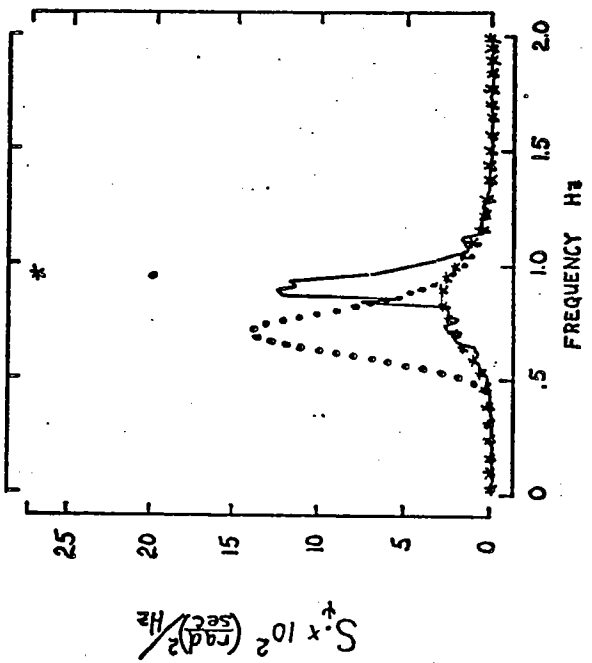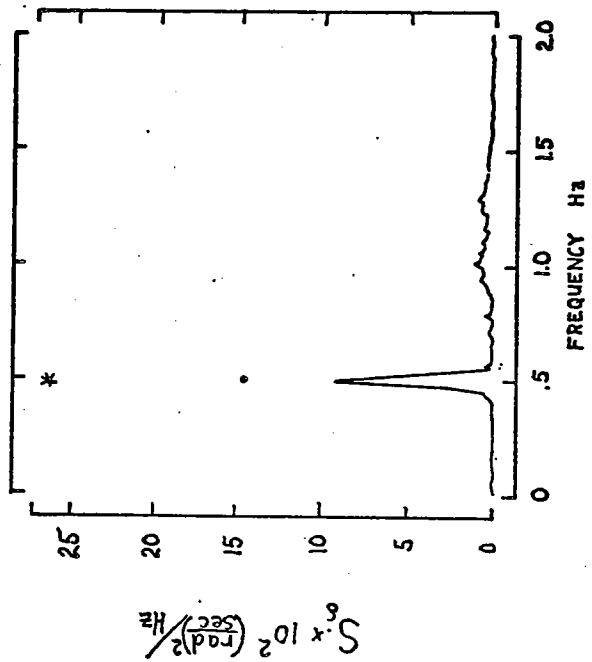
	LIN***	Exp—	LIN $C_a=D$ ***
σ_A^2	1.2×10^{-3}	1.2×10^{-3}	1.2×10^{-3}
σ_ψ^2	.043	.026	.024
σ_δ^2	.0069	.012	.012

Figure 5.6 d   Spar response $U_o = .3\,m/s$, $V = 25\,m/s$

A vortex was shed at each tail of the "U" trajectory, as the motion reversed direction. As for the previous paired shedding case, an oscillating drag coefficient of .5 rather than .06 was necessary to achieve reasonable linearized predictions. Strouhal number of .16, as mentioned earlier, gives good agreement with the experimental oscillation frequency.

All of the linearized estimates using $C_a = 1$ are a bit low, and Figures 5.6 c, d show that the wave response is over-predicted and that the peak wave response is at a lower frequency than in the experiment. By assuming that the added mass co-efficient is 0, much better agreement is achieved. This assumption is not altogether unreasonable if we consider Sarpkaya's data, Figure 3.4, and note that there is a decrease in the added mass coefficient when vortex shedding becomes important, around $N_{KC} = 10$. Thus, it appears that an important effect of vortex shedding in a flow with a mean component may be the reduction of the added mass coefficient. Vortex shedding due to a mean flow could thereby have significant effects on structural response, even if the actual vortex forces were not important.

6. Summary and Conclusion

A linearized theory for the response of a circular pendulum spar in two-dimensional random waves and a uniform current has been developed. The linearized inviscid equations of motion were developed using an approximate potential flow theory for slender bodies. The reasons for pursuing the slender body solution were (1) to lend some "legitimacy" to the well-known and widely-accepted strip theory approach to writing the equations, while formally stating the simplifying assumptions, and (2) to allow an estimate to be made of the linear, wave-making, damping force for comparison with estimates of viscous damping. The dynamic equations were amended to account for the "quasi-steady" wake effects of viscous bluff body flow by including a quadratic drag law. This idea is inherent in the Morrison equation, widely used to interpret wave force measurements, and stems principally from the concepts of superposition and steady flow drag. The principal flaw in this concept is a consequence of the fundamental "non-steadiness" of the bluff-body drag in steady flow, that is to say that there are always significant fluctuations from the mean in the forces on a cylinder in steady flow. This is due to periodic fluctuations in the wake, generally characterized as vortex shedding. It seems a bit hopeless therefore to attempt to describe the forces with any fidelity without incorporating this effect. The

quasi-steady drag force was therefore supplemented, again

resorting to superposition, by a spectral model for the forces

on a cylinder due to an oscillating wake.

The forces due to "vortex" effects were modeled as a

frequency modulation process. Note that this includes an in-line,

drag, component and a transverse, lift, component. The major

assumption was that the vortex shedding frequency was proportional

to the instantaneous speed of the fluid in the incident field. A

spectrum of vortex forces was then estimated using the method of

stationary phase. There are two important faults with this model.

The first is a consequence of the fact that the stationary phase

approximation only works when the modulating signal, the dynamic

pressure in this case, is lower in frequency than the carrier,

vortex frequency. This means that if the spectra of vortex

shedding forces predicted by the model contain frequencies less

than or only slightly larger than the spectrum of the fluid

velocities, then this model is not valid. It was suggested that

in this case, sinusoidal forces predicted by the mean flow only

would be an appropriate substitution. The second shortcoming is

due to the neglect of feedback between the wake and the motions

of a cylinder. Although it is possible to "adjust" the shedding

frequency of the model to produce an adequate result, this manip-

ulation is a little unsettling. However, since there is no

reasonably simple way to include the feedback, the user must be

aware of lock-in phenomena, so that this solution can be "artificially" produced and studied. The model proposed for forces on the cylinder can be considered as composed of three components: first, the inertial force predicted by inviscid theory; second, a quasi-steady quadratic drag; and third, a "vortex" induced lift and drag force. When there is no current, the forces are dominated by the inertial term for small Keulegan Carpenter numbers, that is, small fluid amplitude-to-cylinder diameter ratios, and by the viscous effects for large N_{KC}, this includes important vortex shedding effects. This should seem reasonable, since for small motions compared to the cylinder, one would expect that potential theory would describe the flow well, and for large motions compared to the cylinder one would expect things to look quasi-steady in terms of the flow field. The effect of a mean flow is to push the dominance of viscous forces toward the low N_{KC} range. The behavior of the vortex shedding forces is probably best described in terms of a spectral impulse, corresponding to the mean flow, which is smeared by the variations in the flow when they are large or comparable to the vortex length, ℓ_v , discussed in Section 3. The most important thing to note here is that, even though the forces are parameterized in terms of velocities and accelerations, the relative importance of any effect is determined by the length scales, that is excursion amplitude, cylinder radius and the mean flow vortex shedding length, ℓ_v.

The non-linear equations of motion which resulted from
the analysis of the forces were solved using a linearization
technique assuming a Gaussian random sea and constant force
coefficients. The linearization equates the expected value of
the power transmitted to the spar by the non-linear viscous
forces to the expected value of the power transmitted by the
equivalent linear forces. The method discussed includes the
extension of the linearization needed to describe mean flow
effects and a spatially distributed process. Since this linear-
ized model was a further simplification of an at best questionable
equation, some numerical experiments were performed to test the
performance of the technique under "ideal" circumstances. For a
variety of simulated environments, the linearization predicts the
standard deviation of the simulation response within 10% and the
mean angle of inclination to within 30%. Since the various
simulations resulted in responses differing by orders of magni-
tude, the linearization performed extremely well.

A laboratory experiment was carried out to test the
linearized spar model in a realistic fluid environment. Only
the low Keulegan Carpenter number regime was investigated with
various mean flows. Some manipulations of the model coefficients
was required to obtain agreement between the experiment and the
linearized estimates. The drag coefficient for vortex induced
in-line motions has not had much previous investigation, and a

value of .5 fits the experimental results presented here much

better than the value of .06, which is more representative of

results given in the literature. It also appeared that

the Strouhal number was significantly reduced by the finite

length of the cylinder from .21 to .16. This effect is often

attributed to the motion of a cylinder, but little variation

in the response frquency could be found although the cylinder

response varied by an order of magnitude. As mentioned above,

it was necessary to further manipulate the Strouhal number to

model the case of lock-in. Perhaps the most interesting result,

however, is the apparent reduction in the added mass coefficient

when there is strong vortex shedding induced by the mean flow.

This is not too surprising though, if we note that the same

effect is observed in oscillating flows with no mean when there

is significant vortex shedding. Although this set of experiments

is by no means conclusive, some important interactions of mean

flow and oscillating flow are apparent.

It is obvious from the few experiments performed here,

if not intuitively, that there is significant interaction between

waves and current in producing structural loading. Since ocean

environments of interest, particularly storms, will contain

simultaneous waves and current near the water surface, it seems

clear that any reasonable structural loading theory should consider

the complete problem. The linearization of bluff body drag

forces on a cylinder appears to be an accurate method of pre-
dicting the response of an elastically supported cylinder so
that further investigation of its performance in this and more
general applications is warrented. Extension of the present
theory should include the effects of horizontal correlation of
random waves, directional spreading of the wave spectrum, as
well as an arbitrary angle between waves and current.

REFERENCES

Bedrosian, E. and S.D. Rice, 1971, "The Output Properties of
    Volterra Systems (Nonlinear Systems with Memory) Driven
    by Harmonic and Gaussian Inputs", Proceedings of the
    IEEE, Vol. 59, No. 12.

Bendat, J.S. and A.G. Piersol, 1971, Random Data: Analysis and
    Measurement Procedures, Wiley-Interscience, New York.

Bidde, D.D., "Laboratory Study of Lift Forces on Circular Piles",
    Journal of the Waterways, Harbors and Coastal Engineering
    Division, ASCE, Vol. 97, No. WW4, pp. 595-614.

Blerins, R.D. and T.E. Burton, 1976, "Fluid Forces Induced by
    Vortex Shedding", Journal of Fluids Engineering, Transactions
    of the ASME, March, pp. 19-26.

Borgman, L.E., 1967, "A Statistical Theory for Hydrodynamic Forces
    on Objects", Annals of Mathematics, February.

Bruun, H.H. and P.O.A.L. Davies, 1975, "An Experimental Investi-
    gation of the Unsteady Pressure Forces on a Circular Cylinder
    in a Turbulent Cross Flow", Journal of Sound and Vibration,
    Vol. 40, No. 4.

Caughey, T.K., 1963, "Equivalent Linearization Techniques", JASA,
    Vol. 35, No. 4.

Crandall, S.H. and W.D. Mark, 1963, Random Vibration in Mechanical
    Systems, Academic Press, New York.

Gerrard, J.H., 1966, "The Mechanics of the Formation Region of
    Vortices Behind Bluff Bodies", JFM, Vol. 25, pp. 401-413.

Gouda, B.H.L., 1975, "Some Measurements of the Phenomena of Vortex
    Shedding and Induced Vibrations of Circular Cylinders",
    Technische Universitat Berlin Report DLR-FB 75-01.

Griffin, O.M., 1972, "Flow Near Self-Excited and Forced Vibrating
    Circular Cylinders", Journal of Engineering for Industry,
    Vol. 94, No. 2, pp. 539-547.

Griffin, O.M., R.A. Skop, and S.E. Ramberg, 1975, "The Resonant,
     Vortex-Excited Vibrations of Structures and Cable Systems",
     OTC Paper 2319.

Griffin, O.M., R.A. Skop, and S.E. Ramberg, 1976, "Modeling of
     the Vortex-Induced Oscillations of Cables and Bluff Struc-
     tures", 1976 Society for Experimental Stress Analysis Spring
     Meeting, Silver Spring, MD.

Havelock, T.H., 1958, "The Effect of Speed of Advance Upon the
     Damping of Heave and Pitch", Quarterly Transactions of the
     Institution of Naval Architects.

Hoerner, S.F., 1965, Fluid-Dynamic Drag, Published by the Author,
     2 King Lane, Brick Town, NJ   08723.

Isaacson, M. de St. Q. and D.J. Maull, 1976, "Transverse Forces on
     Vertical Cylinders in Waves", Journal of the Waterways,
     Harbors and Coastal Engineering Division, ASCE, Vol. 102,
     No. WW1, pp. 49-59.

King, Roger, 1977, "A Review of Vortex Shedding Research and Its
     Applications", Ocean Engineering, Vol. 4, pp. 141-171.

Mavor, J.W., Jr., P.F. Poranski, and R.G. Walden, 1976, "A Current
     Monitoring System for Ship Navigation", OTC Paper 2459.

Mercier, J., 1973, "Large Amplitude Oscillations of a Circular
     Cylinder in a Low-Speed Stream", Ph.D. Thesis, Stevens
     Institute of Technology.

Newman, J.N., 1963, "The Motions of a Spar Buoy in Regular Waves",
     David Taylor Model Basin Report 1499.

Newman, J.N., 1977, Marine Hydrodynamics, The MIT Press,
     Cambridge, MA.

Papoulis, A., 1965, Probability, Random Variables, and Stochastic
     Processes, McGraw-Hill, New York.

Sarpkaya, T., 1976, "Vortex Shedding and Resistance in Harmonic
     Flow about Smooth and Rough Circular Cylinders at High
     Reynolds Numbers", Naval Postgraduate School Report NPS-
     59SL76021.

Seymour, R., 1974, "Resistance of Spheres in Oscillatory Flows",
     Ph.D. Thesis, University of California, San Diego.

Skop, R.A. and O.M. Griffin, 1973, "A Model for the Vortex-
     Excited Resonant Response of Bluff Cylinders", Journal
     of Sound and Vibration, Vol. 27, No. 2, pp. 225-233.

Tanida, Y., A. Okajima, and Y. Watanabe, 1973, "Stability of a
     Circular Cylinder Oscillating in Uniform Flow or in a Wake",
     JFM, Vol. 61, pp. 769-784.

Vakman, D.E., 1968, Sophisticated Signals and the Uncertainty
     Principle in Radar, Springer-Verlag New York, Inc., NY.

Wehausen, J.V., 1961, "Surface Waves", Handbuch der Physik,
     Springer Verlag, Section 13.

APPENDIX A

Solution of Velocity Potentials

We shall use the coordinate systems defined in Section 2.1.1 and begin the analysis by restating the decomposed velocity potential defined by Equations (2.3) and (2.4).

$$\Phi(x,y,z,t) = A \frac{g}{\omega} \frac{\cosh kz}{\cosh kh} e^{i(kx-\omega t)} + \phi_A + \phi_\psi \qquad (A.1)$$

On the spar, the kinematic boundary condition may be written, see for example Wehausen and Laitone (1960), as

$$\frac{D}{Dt}[r' - R(z')] \equiv \left(\frac{\partial}{\partial t} + \nabla \Phi \cdot \nabla\right)[r' - R(z')] = 0 \qquad (A.2)$$

$$\text{on} \quad r' = R(z')$$

That is, the substantial derivative of the equation for the surface of the body is zero. Equation (A.2) may be rewritten as follows:

$$\frac{\partial}{\partial t} r' - \frac{\partial R}{\partial z'} \frac{\partial z'}{\partial t} + \frac{\partial \Phi}{\partial r'} \frac{\partial r'}{\partial r'} - \frac{\partial \Phi}{\partial z'} \frac{\partial R}{\partial z'} = 0$$

Making use of the following properties

$$\frac{\partial}{\partial z'} = \frac{\partial}{\partial z} + \psi \frac{\partial}{\partial x}$$

$$r' = (x^2 - 2xz\psi + y^2)^{1/2}$$

$$\frac{\partial r'}{\partial t} = -z\dot{\psi}\cos\theta$$

$$\frac{\partial}{\partial r'} = \frac{\partial}{\partial r}$$

keeping only the lowest order terms in ψ the kinematic boundary condition becomes

$$-z\dot{\psi}\cos\theta - x\dot{\psi}\frac{dR}{dz} + \frac{\partial \Phi}{\partial r} - \frac{\partial \Phi}{\partial z}\frac{dR}{dz} = 0 \qquad (A.3)$$

$$\text{on } r = R(z)$$

We shall now assume that $\frac{dR}{dz}$ is the same order as Ak and ignore second order terms in which it appears. Substituting

Equation (A.1) into Equation (A.3) and equating terms according to their dependence on different displacements, the following boundary conditions are obtained:

$$\frac{\partial \phi_\psi}{\partial r} = \dot{\psi} z \cos\theta \tag{A.4}$$

$$\frac{\partial \phi_A}{\partial r} = -i \frac{gk}{\omega} \cos\theta \frac{\cosh kz}{\cosh kh} e^{-i\omega t} \tag{A.5}$$

on r = R(z)

We now employ slender body theory, which matches an approximate 2-dimensional solution near the body with a three-dimensional solution, see for example Newman (1977). To satisfy the above boundary conditions, we find that an axial line of dipoles pointed in the x direction is necessary. The moment density necessary to satisfy Equation (A.4) is $\frac{1}{2}\dot{\psi} z [R(z)]^2$ per unit length, so that in an infinite fluid

$$\phi_\psi = \frac{1}{2} \dot{\psi} \int_0^h \varsigma R^2(\varsigma) \frac{\partial}{\partial x} \left[\frac{1}{r*}\right] d\varsigma$$

where $$r*^2 = x^2 + y^2 + (z-\varsigma)^2 = r^2 + (z-\varsigma)^2$$

To satisfy the free surface, bottom and radiation boundary conditions of Equations (A.4) and (A.5), we substitute for the source potential, $\frac{1}{r*}$, the potential, $\bar{\phi}_s$, of a source pulsating at frequency ω under a free surface in a fluid of depth h, see Wehausen and Laitone (1960).

$$\bar{\phi}_s(x,y,z,t;\varsigma) = e^{-i\omega t} \left[\frac{1}{r*} + \frac{1}{r_2*} + \right. \tag{A.6}$$

$$\int_0^\infty \frac{2(\nu+k_\infty)e^{-\nu h}\cosh\nu z \cosh\nu\varsigma}{\nu\sinh\nu h - k_\infty\cosh\nu h} J_0(\nu r) d\nu$$

$$2\pi i \frac{(k_\infty+k)e^{-kh}\sinh kh \cosh k\varsigma \cosh kz}{k_\infty h + \sinh^2 kh} J_0(kr)$$

where $\int$ denoted Cauchy principle value, $r_2*^2 = x^2 + y^2 + (z+\varsigma)^2$ and $k = \frac{\omega^2}{g}$.

Knowing the solution of Equation (A.4) in an infinite

fluid, we anticipate the form of the dipole strength in the

present case and write

$$\phi_\psi = \tfrac{1}{2}\,\dot\psi \int_0^h R^2(\varsigma)(\varsigma + i\,F(\varsigma))\frac{\partial}{\partial x}\left(\Phi_s(x, y, z, t; \varsigma)\right)d\varsigma \qquad (A.7)$$

We will be interested in the potential near the body, so that to

leading order in r for the real and imaginary terms, we find that

$$\phi_\psi = \tfrac{1}{2}\,\dot\psi\Big[\int_0^h \varsigma R^2(\varsigma)\frac{\partial}{\partial x}(r^2+(z-\varsigma)^2)^{-\tfrac{1}{2}}d\varsigma + \qquad (A.8)$$

$$2\pi i \int_0^h \varsigma R^2(\varsigma) K \cosh k\varsigma \cosh kz \frac{\partial}{\partial x} J_0(kr)\,d\varsigma +$$

$$i\int_0^h R^2(\varsigma) F(\varsigma)\frac{\partial}{\partial x}(r^2+(z-\varsigma)^2)^{-\tfrac{1}{2}}d\varsigma$$

where $\quad K = \dfrac{k_\infty + k e^{-kh}\sinh kh}{k_\infty h + \sinh^2 kh}$

Noting that for small values of kr, $J_0(kr) \approx 1 - \tfrac{1}{4}(kr)^2$ and that

for any continuous bounded function $f(\varsigma)$

$$\int_0^h f(\varsigma)\frac{\partial}{\partial x}(r^2+(z-\varsigma)^2)^{-\tfrac{1}{2}}d\varsigma \approx -2\,\frac{f(z)}{r}\cos\theta$$

for $0 < z < h$ and $r \ll h$, see Newman (1960), Equation (A.8)

becomes

$$\phi_\psi = \tfrac{1}{2}\Big[-2z\,\frac{R^2(z)}{r}\cos\theta - \qquad (A.9)$$

$$i\pi K k^2 x \cosh kz\, F^* -$$

$$i z\,\frac{\cos\theta}{r}R^2(z)\,F(z)\Big]$$

where $\quad F^* = \int_0^h \varsigma R^2(\varsigma)\cosh k\varsigma\,d\varsigma$

If we substitute Equation (A.9) into the boundary condition,

Equation (A.4), and solve for $F(z_o)$, we find that

$$F(z) = \tfrac{1}{2}\pi K k^2 \cosh kz\, F^* \qquad (A.10)$$

Therefore, Equations (A.9) and (A.10) define the complex potential,

ϕ_ψ , to lowest order in r for the real and imaginary parts. In

a similar manner, we find that, to lowest order in r, the solution

to Equation (A.5) is

$$\phi_A = i \frac{gk}{\omega} \frac{\cosh kz}{\cosh kh} \frac{R^2_{(z)}}{r} \cos\theta \; e^{-i\omega t} \qquad (A.11)$$

APPENDIX B

Convergence of Iterative Solution

In order to show that a function $= f(\alpha)$ has a convergent successive approximation solution, it is sufficient to demonstrate that there is a region around α, $|x - \alpha| < h$, such that

$$\left| \frac{d\, f(x)}{d\, x} \right| < 1$$

We will look at the zero mean velocity case, since the equivalent velocity is most sensitive to the oscillator response when there is no mean flow. Using Equations (4.8) and (4.10) we can write

$$U_E = \sqrt{\frac{8}{\pi}} \left[\int_{-\infty}^{\infty} \left| \frac{U_r}{A_0} \right|^2 S_{A_0}(\omega)\, d\omega \right]^{1/2}$$

where $\frac{U_r}{A_0}$ is defined by Equation (4.5). We shall simplify this further by assuming that the input spectrum $S_{A_0}(\omega)$ has a uniform density of S_{A_0} between ω_1 and ω_2 and is zero elsewhere, so that

$$U_E = \sqrt{\frac{8}{\pi}} \left[S_{A_0} \int_{\omega_1}^{\omega_2} \left| \frac{U_r}{A_0} \right|^2 d\omega \right]^{1/2}$$

A sufficient condition for convergence is then to show that

$$\int_{\omega_1}^{\omega_2} \frac{\partial}{\partial U_E} \left| \frac{U_r}{A} \right|^2 d\omega < \frac{1}{S_{A_0} \frac{8}{\pi}} \tag{B.1}$$

where

$$\frac{\partial}{\partial U_E} \left| \frac{U_r}{A_0} \right|^2 = - \frac{2 U_E \omega^4 C^2 (1 - \omega^2 + \omega^2 F)^2}{[(1 - \omega^2)^2 + (\omega C U_E)^2]^2} \tag{B.2}$$

Unfortunately, Equation (B.2) blows up near resonance and we cannot satisfy the sufficiency condition for convergence. It appears that the convergence condition, Equation (B.1), can

always be forced to fail by choosing an input density large

enough. Despite this apparent failure, it should be noted that

a number of numerical experiments discussed in Section 4.3 con-

verged rapidly, and only 7 or 8 iterations were necessary to

obtain 1% accuracy for U_E . It appears, however, that the

successive approximation scheme may on occasion be divergent.

Even if this should occur, a solution can always be obtained

by a bisection routine. This can be demonstrated by noting

that the derivative of Equation (B.2) is always negative. The

significance of this can be easily noted by looking at Figures

B.1 a, b, c in which we have plotted $\left| \dfrac{U_r}{A_o} \right|$. That is, as U_E

decreases, the relative velocity transfer function grows uniformly.

The bisection routine begins by guessing a value of U_E and com-

puting a new value as in the successive approximation routine.

We can see from Figure B.1 that, regardless of the shape or

magnitude of the input spectrum, if the guessed value of U_E is

larger than the true value, the new value will be less than the

true value, and vice-versa. We now have an upper bound and a

lower bound for the true value. If we now bisect this region

and compute a new value of U_E , we can find which half of the

bisected region includes the true value, even if the new value

lies outside both regions. We can therefore maintain bounds on

the true value and at least cut the region in half with each

iteration. One could easily write a routine which begins

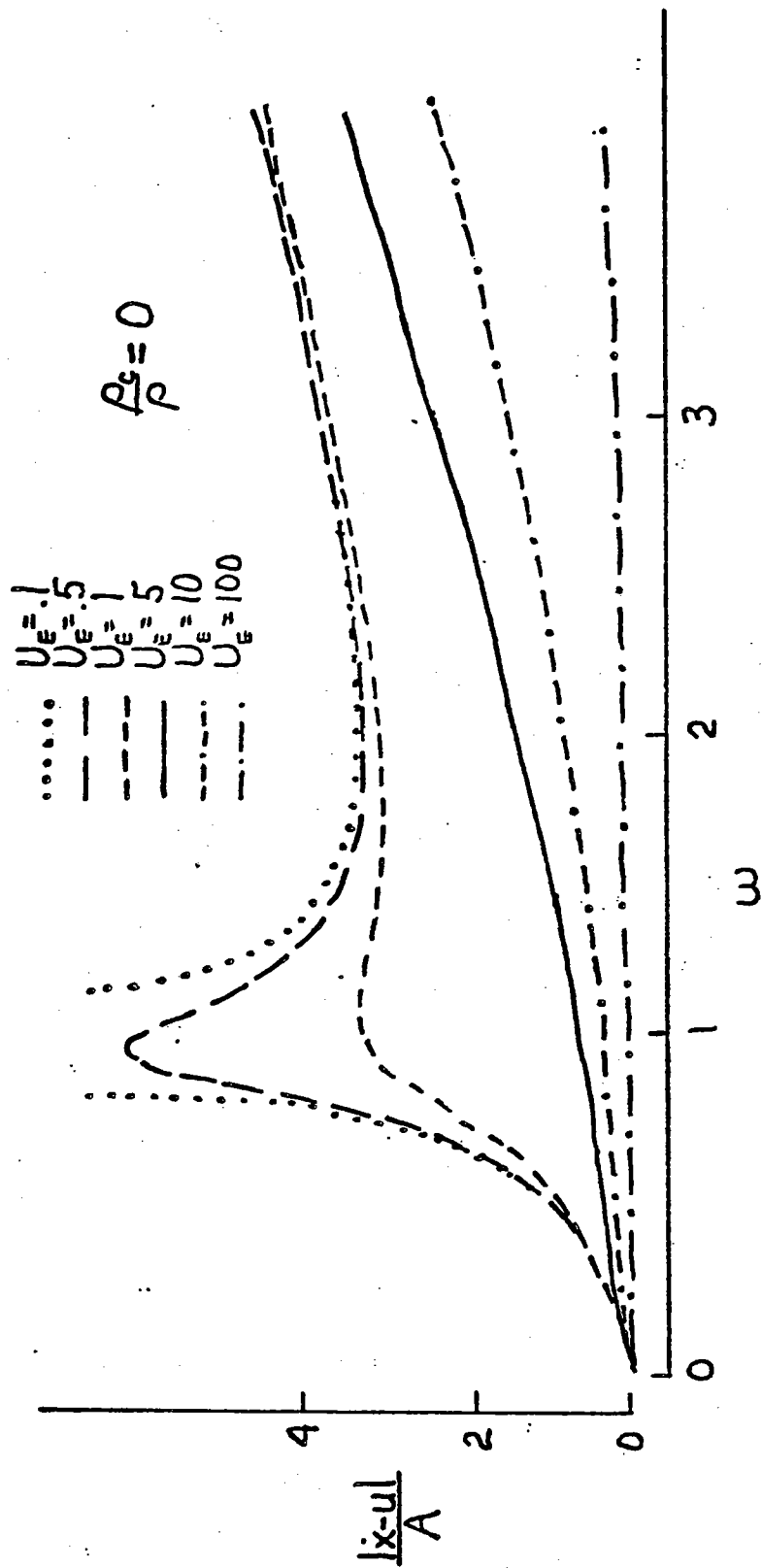solution by successive approximation, checks for divergence and

Figure B.1 a   Relative velocity transfer function for various
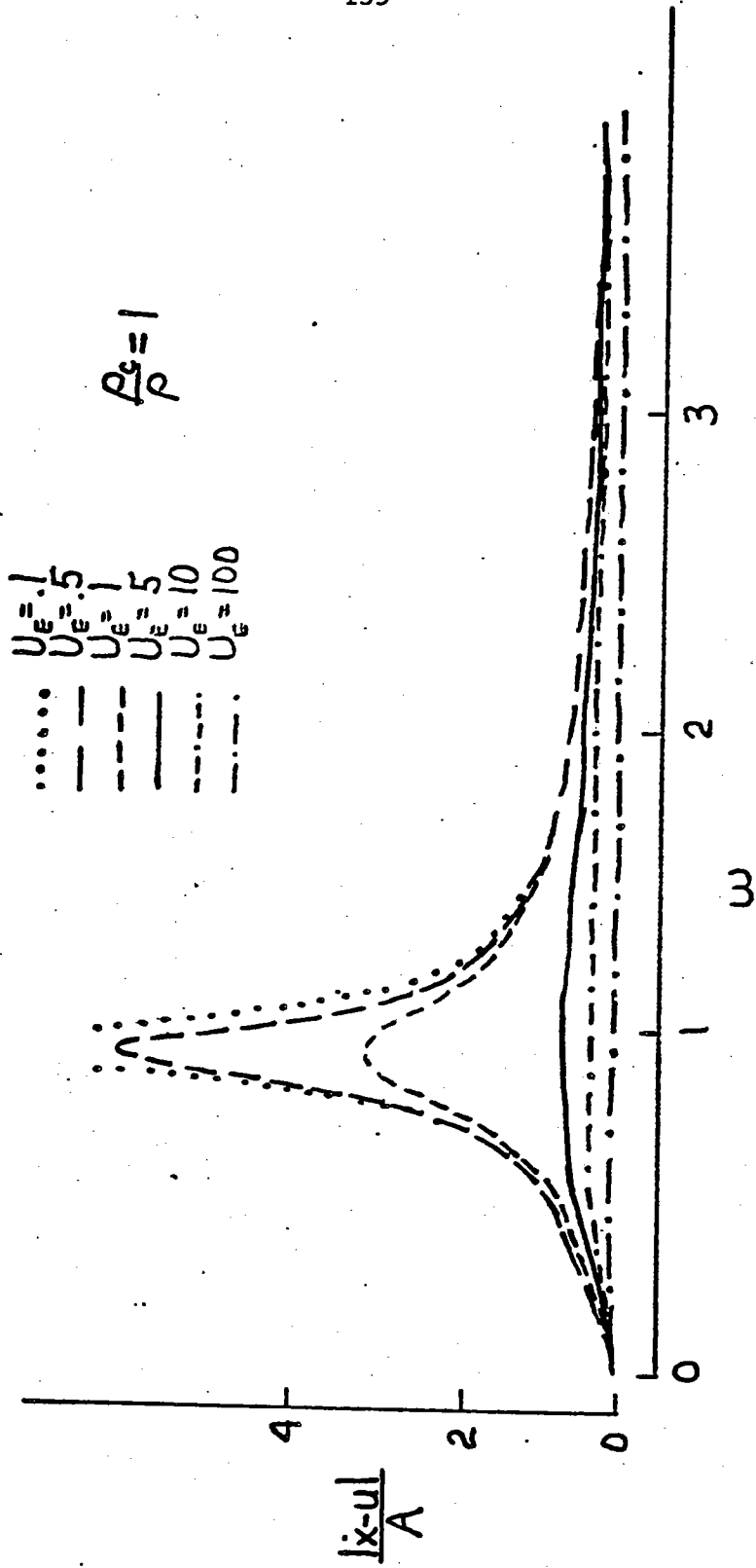values of equivalent velocity, $\frac{\rho_c}{\rho} = 0$.

Figure B.1 b Relative velocity transfer function for various
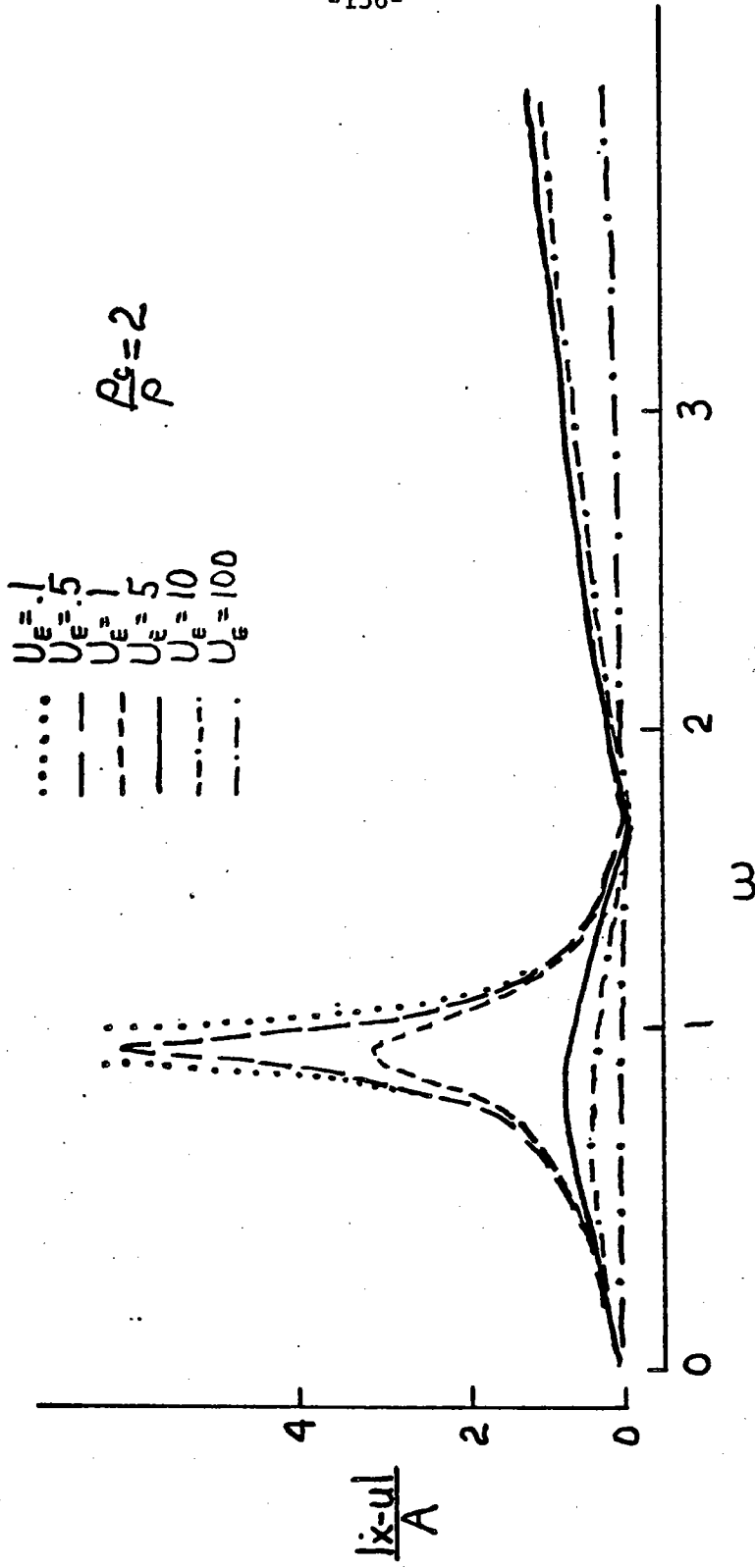values of equivalent velocity, $\frac{\rho_s}{\rho} = 1$.

Figure B.1 c   Relative velocity transfer function for various
values of equivalent velocity, $\frac{\rho_e}{\rho} = 2$.

implements bisection if necessary. We shall limit the discussion
of convergence to this simple model, and state that similar
arguments and conclusions can be made about the more complicated
case of the spar governing equations.

BIOGRAPHICAL NOTE

George Rodenbusch was born December 31, 1951 in San Turse, Puerto Rico. He was reared in Irving, Texas since 1959, and entered Rice University in 1969. He married Nancy Esther Trigg in March 1972, and they have a daughter, Brenda Margaret, born in December 1976.

While at Rice, he was a George R. Brown Scholar and was elected to the Tau Beta Pi honor society. During his fifth year at Rice he worked as a research assistant in the Biomedical Engineering Department assisting in investigations of hemolysis in artificial circulatory assist devices. In May of 1974 he received the degrees of B.S. and M.M.E. cum laude in Mechanical Engineering. He entered the MIT-WHOI Joint Program in Ocean Engineering in June 1974 with a three-year NSF graduate fellowship. Plans are presently being made to work for Shell Development Company after graduation.